Regolith Adaptive Modification Systems (RAMS)

FINAL REPORT: 80NSSC21K0698

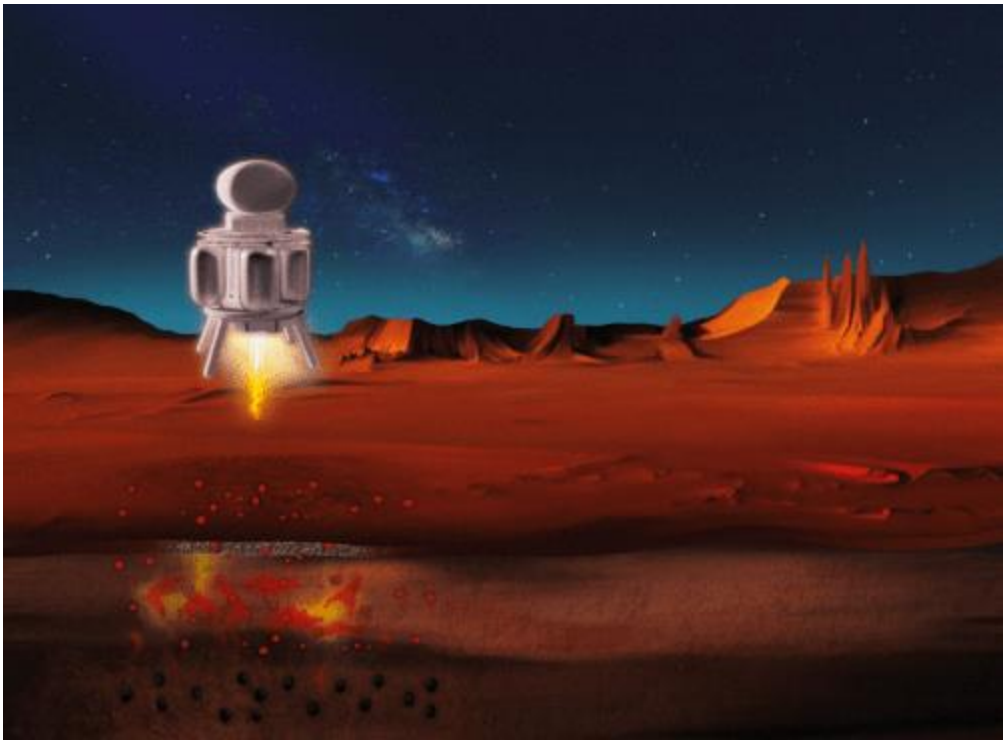

INSTITUTION: Texas A&M Engineering Experiment Station

NIAC FELLOW: Sarbajit Banerjee, Davidson Chair in Science, Professor of Chemistry, Professor of Materials Science & Engineering, Texas A&M University

CONTRIBUTING AUTHORS AND PROGRAM PERSONNEL: Anita, Dr. Nicholas I. Cool, Jingxiang Cheng, Daniel Bronner, Elbert Wang, Christian Kornelis, Dr. Natalia Rivera-Gonzalez, Dr. Saul Perez-Beltran, Prof. Jeffrey W. Bullard, Prof. Bjorn Birgisson

Texas A&M University, College Station, TX 77845-3345

Prof. Kevin Cannon

Geology and Geological Engineering Department, 1516 Illinois St., Colorado School of Mines, Golden, CO 80401

PROGRAM ADVISORS: Nicole Shumaker, Prof. Patrick Suermann

Texas A&M University, College Station, TX 77845-3345

NIAC NASA Innovative Advanced Concepts

TEES | Texas A&M Engineering Experiment Station

TABLE OF CONTENTS

LIST OF FIGURES

Figure 4. Schematic depiction of proposed progression of the RAMS process

Figure 5. Crystal structure and three different surfaces of α-Fe_2O_3 examined for reactivity with metallic magnesium in *ab initio* molecular dynamics simulations

Figure 6. Snapshots acquired during a 60 ps *ab initio* molecular dynamics simulation of $Fe_2O_3(001)||Mg(001)$ reaction underscoring the mechanism of thermite-triggered steel formation on the surfaces of extraterrestrial objects

Figure 7. Sequestration of molten iron by MgO and two distinctive heat release regimes evidenced in an *ab initio* molecular dynamics simulation of the reaction of $Fe_2O_3(104)||Mg(001)$ underscoring the mechanism of thermite-triggered steel formation on the surfaces of extraterrestrial objects

Figure 8. Final product configurations and heat release profiles for different facets of Fe_2O_3 reacted with Mg in a thermite reaction resulting in phase segregation and stabilization of iron as a precursor to *in situ* synthesis of advanced high-strength steels

Figure 9. Heat ramp (33 K/ps) *ab initio* molecular dynamics simulation of the $Mg/FeTiO_3$ nano-thermite system resulting in Ti—Fe alloy formation.

Figure 10. Initial configuration of $TiO_2(101)||Mg(0001)$ before initiation of the thermite reaction

Figure 11. The cumulative particle-size distribution curve of the LMS-1 simulant and schematic illustration of laboratory setup for performing thermite reactions

Figure 12. Characterization of reaction products of Fe_2O_3 and Mg thermite reaction indicating desired formation of iron

Figure 13. Laboratory scale experimental reaction of Mg with Fe_2O_3

Figure 14. Characterization of products of thermite reactions of Mg with $FeTiO_3$

Figure 15. Characterization of products of thermite reactions of Mg with TiO_2 in air

Figure 16. Characterization of products of thermite reactions of Mg with SiO_2

Figure 17. Characterization of products of thermite reactions of Mg with Al_2O_3

Figure 18. Reaction conditions for stabilization of Mg particles of different geometries and surface planes.

Figure 19. Initial configuration for the system silica/geopolymer precursors. **(A)** Siloxo and sialate oligomers. **(B)** Side view of the hydroxylated slab α-SiO_2 $(01\bar{1}0)$ packed with these oligomer precursors at a molar ratio Si/Al = 1

Figure 20. Schematic illustration of the matrix transformation process

LIST OF TABLES

1. EXECUTIVE SUMMARY

Establishing human habitation on the Moon or Mars requires a palette of reaction chemistries for deconstructing extraterrestrial soils to extract structural metals, fuels, and propellants, as well as consolidating the soils into load-bearing forms. This report outlines progress related to the fundamental chemistry of *in-situ* resource utilization that is the focus of our Regolith Adaptive Modification System (RAMS) NIAC project. The RAMS concept is a breakthrough approach for

preparing surfaces for early landing sites– and subsequent settlement operations– on the Lunar and Martian surface, among others. The RAMS concept is aligned with aspirations and capabilities of planned NASA Artemis mission. The approach is predicated on the ***sequential delivery of microcapsules onto lunar and Martian surfaces, which upon rupture, release payloads that react with regolith to yield geopolymerized subsurface slabs and surface high-strength steel skin and anchors***. Through successively more exothermic reactions, we are seeking to build subsurface geopolymer slabs and use thermite reactions to constitute micro-alloyed advanced high-strength steel (AHSS) and Ti—Al—V pads on surfaces of planetary bodies, thereby circumventing the need for energy-intensive sintering technologies. As a precursor delivery system used to constitute landing pads, RAMS can be scaled for robotic, human-class, and more prominent (i.e., Starship) landers and will be configured within pressurized delivery systems that use radio beacons to outline coordinates for precision landings. Microcapsule delivery systems are designed to impel precursors (nanothermite mixtures and organosilanes), which activate in response to stress, heat, or impact to constitute deep geopolymerized slabs and AHSS skins. Dust mitigation is accomplished by reaction/solidification chemistry that yields a subsurface slab and advanced high-strength steel skin and anchors.

Our NIAC project has three primary thrusts:

(**1**) the development of thermite chemistry for metal recovery and preparation of advanced high-strength alloy skins;
(**2**) the discovery of matrix transformation chemistries to enable rapid and low-power regolith consolidation; and
(**3**) the design of microcapsule delivery systems to affect chemical transformations of regolith with 3D spatiotemporal control of reaction fronts across the surface and subsurface porous regolith.

We have completed the proposed tasks in all three areas using a combination of scoping studies, multiscale simulations, laboratory-scale synthesis and characterization, mechanistic studies of *in situ* transformations, and prototyping. Over the project period, we have established a palette of Mg thermite precursors and demonstrated unprecedented control over the microstructure of obtained metal composites. Using a combination of *ab initio* molecular dynamics simulations, experimental studies of thermite reactions, detailed microstructural analysis, and micromechanics measurements, we have ***designed ceramic-embedded sintered steel and Ti—Al alloy composites that can be accessed from Lunar regolith and represent promising structural materials for lunar infrastructure***. In the second thrust of this effort, we have developed formulations of matrix transformation precursors custom-designed to enable the ***construction of tiles and bricks from modified Lunar regolith***. Crack-free modified regolith bricks have been obtained with unprecedented thermal resistance from -196 to 1430°C that can further withstand repeated loadings of >1000 lbs/in^2. Multiscale simulations have informed the optimal design of formulations with setting kinetics that enable rapid solidification of subsurface regolith. In the final thrust of the project, we have developed scalable jetting methods for preparing microcapsules with finely tunable shell materials that allow for controlled positioning and activated release of precursors to enable *in situ* resource utilization and regolith consolidation. We have further developed models for controlling microcapsule delivery, which is informing the design of integrative models and delivery systems incorporating precise reaction sequences for 3D control of reaction fronts on extraterrestrial soils.

2. INTRODUCTION

An intense new space race has begun, with significant powers competing to build long-term human habitats on the moon, explore the unbounded opportunities enabled by the cis-lunar economy, and to use the moon as a launchpad for exploring the furthest frontiers of space. A wide range of technological challenges stands in the way of lasting human habitation on the moon. Two interconnected problems pertain to the need to manufacture building materials in the Lunar environment and the interconnected challenge of processing lunar materials to extract the elements needed to sustain our way of life. Transporting metals and concrete from Earth is cost prohibitive, so we must find ways to make the materials we need using only Lunar resources. Regolith Adaptive Modification Systems (RAMS) is a game-changing technology for selective reinforcement and fusion of Lunar regolith to landing pads and other early landing surface structures needing load-bearing capacity. RAMS does not require an extensive infrastructure for deployment. The novel technologies include: (1) a built-in microcapsule-based welding and regolith solidification system consisting of nano-thermite mixtures and soil stabilizers designed to activate sequentially to form advanced high-strength and ductile steel anchors; (2) the use of energy stored within the chemical bonds of regolith components for *in situ* spot welding and creation of embedded alloys.

RAMS can significantly reduce the cost of building early landing infrastructure required to enable repeated landings and provide additional load-bearing capacity to other Lunar structures while mitigating the need for large landing structures with substantial mass, energy, and time requirements. RAMS can also be used as the primary strategy to construct platforms that protect sensitive equipment and samples from contamination by extraterrestrial dust plumes.

An animated view of the RAMS NIAC Concept has been developed over the project period and is available at: https://youtu.be/hFTaP4QlBSo. The animation has been widely disseminated on Twitter and LinkedIn as part of a media release timed to coincide with the 2021 (virtual) NIAC Symposium. In the following few sections, we provide a broad context for chemical transformations of extraterrestrial soils; review progress on three of the critical aspects of this effort related to (i) thermite reactions, (ii) matrix transformation reactions to achieve regolith consolidation, and (iii)

microcapsule delivery; finally, we describe efforts to build and test large prototypes; and discuss ongoing outreach and dissemination efforts.

2.1 Background: Chemical Transformations of Extraterrestrial Soils

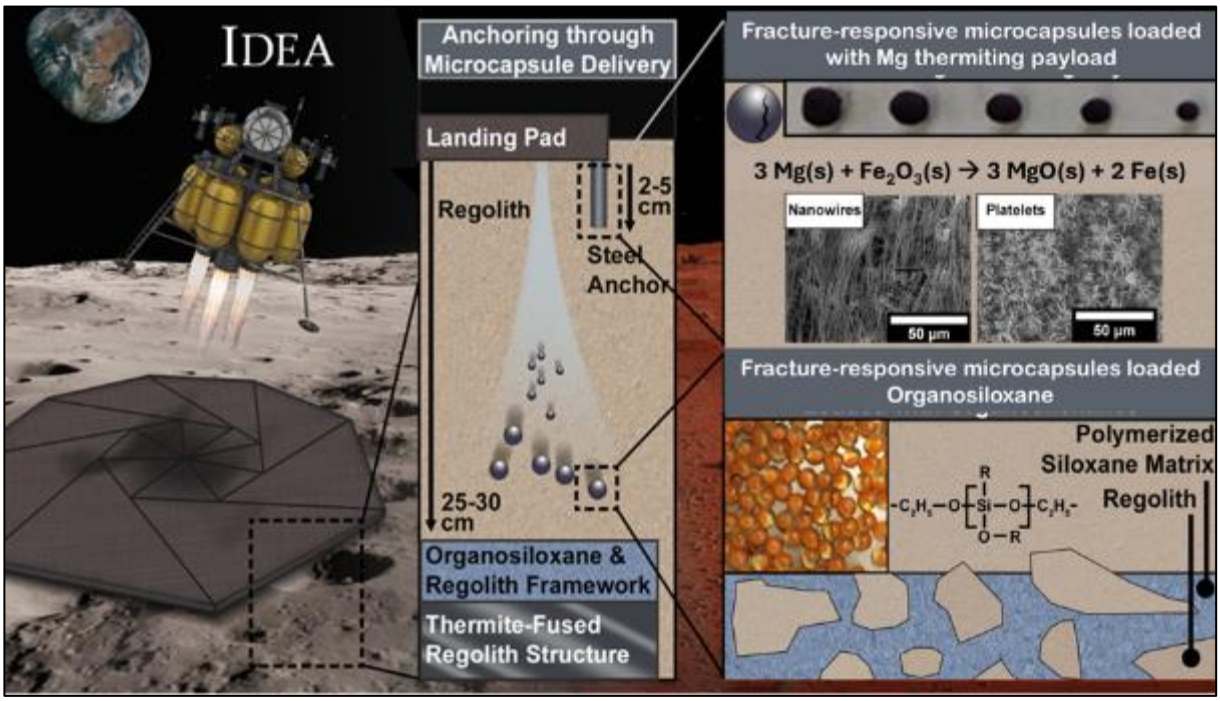

***Figure 1**. Conceptual sketch of our NIAC concept for Regolith Adaptive Modification Systems to support early extraterrestrial planetary landings (and operations).*

Establishing human habitation on the Moon or Mars requires a palette of reaction chemistries for deconstructing extraterrestrial soils to extract structural metals, fuels, and propellants, as well as consolidating the soils into load-bearing forms. We have performed a detailed study, which we briefly summarize to identify key research needs relevant to the fundamental chemistry of *in-situ* resource utilization.[1]

Humankind's space aspirations rely in considerable measure on mounting a sustained presence on the Moon, Mars, and outer planetary bodies, which requires building a self-sustaining infrastructure. Much of the physical components of this infrastructure, landing pads, roads, and scientific outposts equipped with power and data transmission capabilities, will need to be built from mineral resources extracted from regolith, the fine-grained, partially amorphized, and often highly charged soil that covers planetary bodies. Considerable advances are required, not just in excavation, surface preparation, paving, and additive manufacturing, but also in the fundamental understanding of chemical transformations of regolith into load-bearing forms. A closely intertwined challenge involves beneficiation, the deconstruction of extraterrestrial soils to extract valuable metals, semiconductors, fuels, and propellants. All of this must be accomplished under extreme

conditions characteristic of space: low gravity, high vacuum, and significant temperature variations. Razor-sharp fine-grained regolith that blankets rocky planetary bodies represents a major hazard for landing and operations. During propulsive landings, plumes of fine particulate dust are launched outwards with escape velocities of up to 2 km/s; this shrapnel poses a risk to sensitive equipment, obscures vision at critical junctures of human-crewed landings, and can shred

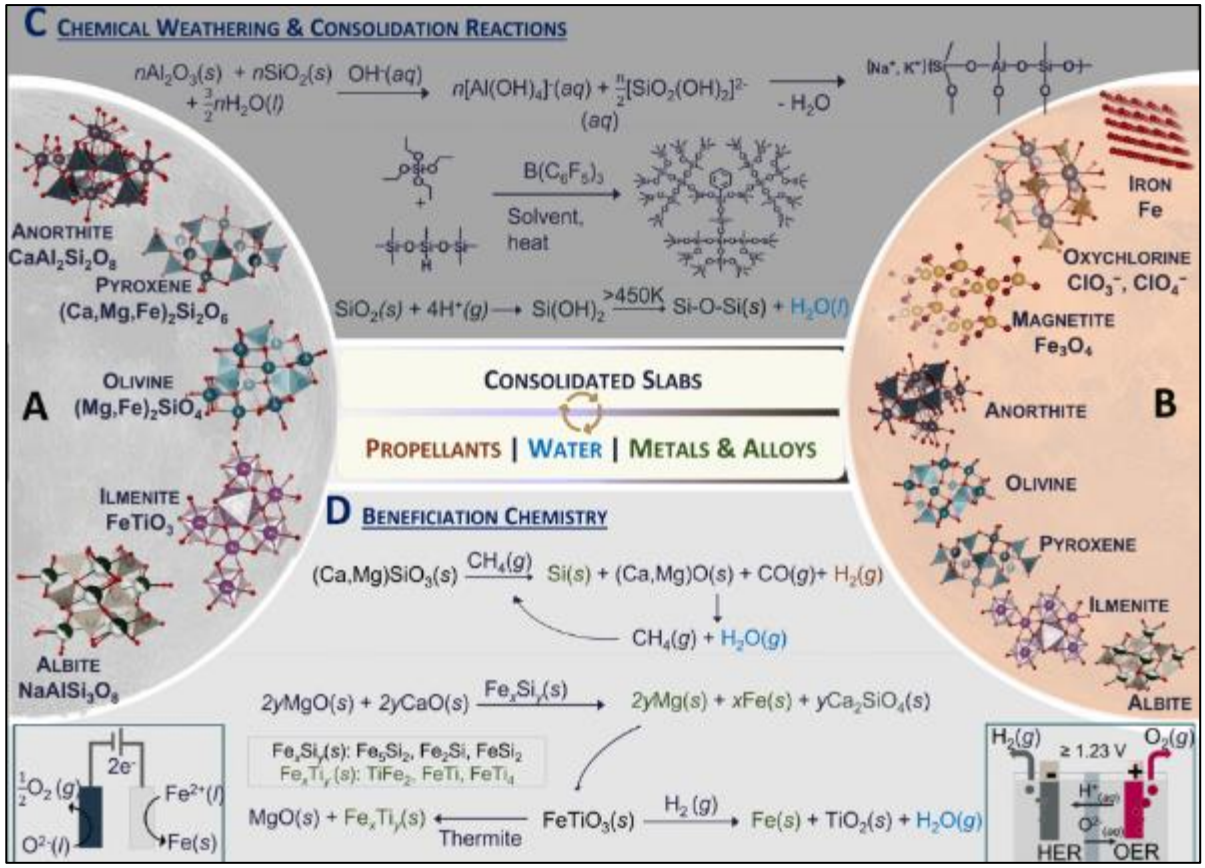

Figure 2. *Palette of reaction chemistries. Crystal structures of compounds present in* ***(A)*** *Lunar and* ***(B)*** *Martian regolith.* ***(C)*** *Reactions under consideration for regolith consolidation including polycondensation of aluminosilicate frameworks under hydrolytic and non-hydrolytic solvents. H^+-implantation from the solar wind leads to hydroxyl formation at defect sites across a variety of regolith compounds. The hydroxylated compounds represent a rich source of potential reactants for initiating fuel recovery, benefaction, and consolidation reactions.* ***(D)*** *shows some representative reactions for extraction of propellants (H_2 & O_2), water, and metals and alloys (Fe, Ti, Fe_xTi_y). Mg precursors for thermite reactions are accessible from lunar regolith via reduction of MgO (mined from olivine) with ferrosilicon (Fe_xSi_y). Fuel and metals can also be electrochemically extracted from molten salts or water as shown in the figure.*

spacesuits and infiltrate interiors of spacecraft. Famously, the Curiosity rover's wheels were mangled by sharp rocks along its traverse on Mars. As space missions target repeated landings, "taming" regolith has become an urgent imperative. The palette of chemical reactions that must be developed for this purpose is constrained not just by the extreme environments

but also by the limited amounts of earth-sourced precursors that can be transported, modest available power budgets, and requirements for fast kinetics to enable rapid deployment.

Lunar regolith is derived from the disintegration of basaltic and anorthositic rocks through thermal weathering, atom/ion implantation mediated by the solar wind, and relentless bombardment from micrometeorites. It comprises particles that range from ca. 40—800 μm in size, albeit nanoscopic crystallites are also prevalent. The chemical composition of regolith varies every few kilometers. Current information is derived from samples returned to Earth and spectra measured from remote-sensing and lunar-derived meteorites.[2,3] Lunar highlands soils are predominantly composed of Ca-rich plagioclase feldspar or cation-intercalated aluminosilicate framework compounds ($NaAlSi_3O_8$ (albite)–$CaAl_2Si_2O_8$ (anorthite)) with relatively smaller amounts of Fe and Mg incorporation.

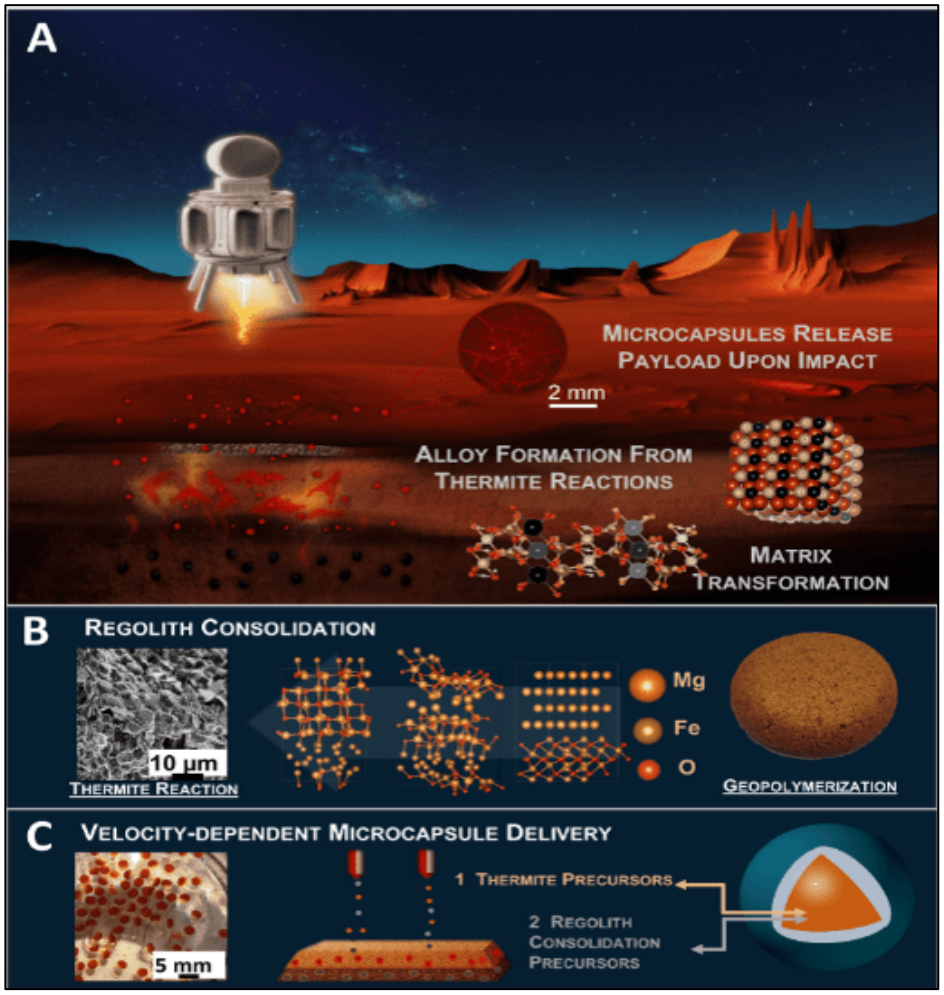

Figure 3. *Schematic depiction of* ***(A)*** *an approach for building of landing pads for repeated take-offs and landing based on consolidation of Lunar or Martian regolith based on delivery of microcapsules to initiate thermite and regolith consolidation reactions.* ***(B)*** *shows representative images of regolith consolidation. Combining thermite and matrix transformation chemistries can yield hardened ceramic slabs with steel/high-strength-alloy metal skins as cohesive building blocks for structural applications surface. Panel B shows a scanning electron microscopy image of a thermite product obtained from a reaction between iron-rich oxide & magnesium. The right images depict a hardened slab obtained from matrix transformation of the lunar regolith from polycondensation of silicates and aluminates. Molecular simulations further our understanding of thermochemical properties and reactivity of regolith; such simulations are guiding rational precursor selection and more deterministic control of reaction kinetics. Shown above is a representative simulated thermite reaction of an iron-rich oxide with magnesium. For a given regolith composition, the temperature and kinetics of the thermite can be tuned by the varying the dimensions and geometry of Mg particles.* ***(C)*** *shows microcapsule delivery of (i) thermite and (ii) matrix transformation precursors across different depths. Microcapsules of precursors can be implanted deeper within the regolith. Heat release from thermite reactions can trigger release of matrix transformation precursors in the subsurface enabling consolidation of regolith into continuous slabs. The panel also shows a representative digital photograph of microcapsules containing a dye tracer.*

In contrast, shadowed Mare regolith comprises silicates such as pyroxenes $(Ca,Mg,Fe)Si_2O_6$) and glass-rich basalt, $CaAl_2Si_2O_8$, olivine ($(Mg, Fe)_2SiO_4$, perovskites such as ilmenite ($FeTiO_3$), and minor amounts of Fe and Ni. **Figure 2A** depicts the structures of some notable regolith compounds. Martian surfaces contain loose- and fine-grained (15—25 wt.% is <4 μm) particles. The basaltic components observed in Lunar regolith, i.e., $NaAlSi_3O_8$—$CaAl_2Si_2O_8$, $(Mg^{2+},Fe^{2+})_2SiO_4$, $(Ca,Mg,Fe)_2Si_2O_6$, $FeTiO_3$, and Fe_3O_4 are the preponderant species;[4] in addition, several S-, Cl-, and mixed-anion compounds, as well as nanophase iron/chromium oxides, have been detected (**Figure 2B**).

2.2 Beneficiation: Extracting Water, Propellants, and Structural Elements

Chemical transformations of regolith to recover water include direct extraction of crystal-lattice-bound water in permanently shaded craters, protonation of hydroxylated minerals, and hydrogen treatment of oxide phases.[5] Water recovered in this manner can be electrocatalytically or photocatalytically split to generate H_2 and O_2 fuels.[6] Solar-wind-implanted volatiles are further expected to contain hydrogen (as well as species such ^3He), and are recoverable from regolith through annealing and degassing. **Figures 2C** and **D** illustrate intertwined water and H_2/O_2 generation reaction pathways associated with several representative regolith compounds. For instance, reducing $FeTiO_3$ with hydrogen yields oxygen, iron, and valuable titanium for developing structural alloys. Vapor phase pyrolysis, molten-salt electrolysis, and reduction with methane also hold promise for oxygen and metal extraction (**Figure 2D**).[7] By using solar concentrators and photoelectrochemical cells, the considerable energy inputs associated with *in situ* resource utilization can be sustainably provisioned.

Combustion-based thermite reactions have gained interest for both beneficiation and regolith consolidation. Such reactions unlock chemical energy stored in the regolith and can reduce many oxides down to the base metal (e.g., Fe or Ti) whilst further enabling regolith consolidation at low external energy inputs (**Fig. 2C**). Thermite reactions initiated by a short thermal impulse propagate a self-sustained combustion wave and can attain temperatures as high as 3000°C yielding a combination of *in-situ* molten metal via combustion of metal oxide and active metal. These will be discussed at length in the next section. Of the two most common metal powders, i.e., Al and Mg, the latter is preferred given its higher energy density, faster reaction rates, and higher autoignition temperature.[8] For components of extraterrestrial soils, the Ellingham curve of Mg lies below most metals across a wide range of pressures and temperatures (with the exception of Ca). Thus, Mg can be employed as a reducing agent, and the mixture of oxides in the regolith can be reduced under the high-vacuum conditions down to molten metals, providing a viable route to the production of steel, lightweight Ti—Al alloys and silicon from regolith **(Figure 3).**[9]

2.3 Regolith Consolidation

A set of reaction chemistries focuses on fashioning the different components of regolith into load-bearing forms that can be used to construct landing pads or 3D printed into habitats. Extraterrestrial solids can be consolidated directly by sintering, which fuses together particles and reduces interparticle porosity at temperatures 60—90% of the melting point. The Lunar Mare and Highlands regolith comprise compounds with melting points of 1000—1300°C; glassy agglutinated inclusions have T_g considerably lower than this value. Even so, sintering requires significant thermal energy and time, but

often both can be decreased dramatically by adding ca. 5 vol.% of a suitable liquid, often water or alcohol. Known as *cold sintering*, the process is thermodynamically driven by chemical potential gradients arising from surface energy and—if pressure is applied—strain energy distribution within the powder compact. The liquid phase draws the particles together by capillary forces and provides a transport medium for the rearrangement of matter by dissolution—precipitation reactions.

The liquid must therefore be a modestly suitable solvent for the solid at processing temperatures, which can be as low as 50—300°C. Cold sintering could be an attractive option for regolith consolidation in the Lunar or Martian environment where power budgets are limited.

Solubility is a key factor in choosing a liquid for cold sintering; aqueous acids or bases are good candidates. Considering $CaAl_2Si_2O_8$, a solution with pH 3 will dissolve anorthite to an equilibrium calcium concentration of about 0.1 $mmol \cdot L^{-1}$ at 25°C, which is sufficient to induce modest mass transport over micrometer-scale distances provided a sufficient gradient in surface or strain energies at interparticle contacts.

The kinetics of consolidation processes of the mineral components depends both on temperature and material characteristics. The specific surface area and crystallinity have the greatest impact on reaction rates. Dissolution rates for scale with the number density and excess Gibbs energy of reactive surface sites, such as the kink sites near the core of dislocation outcroppings for crystalline phases.[10] In 3D network silicates that are major components of extraterrestrial soils, the rate is often controlled by the detachment of network tetrahedra and is accelerated by conditions that favor a nucleophilic attack on Si—O or Al—O bonds. Aluminosilicates with lower-dimensional networks (olivine, pyroxene) are more easily dissolved than 3D networks, and poorly ordered or amorphous structures are yet more reactive.[11]

Sintering is not the only feasible route to consolidation, either. **Figure 2C** illustrates hydrolytic and non-hydrolytic crosslinking routes for regolith consolidation based on forming siloxane and aluminosilicate frameworks connecting and entrapping crystalline particles. Such a structural framework has been demonstrated for the consolidation of Muskeg soil in Northern Alberta as well as to develop a fast-setting 3D printable soil formulation.[12,13] Matrix transformation reactions such as those illustrated in this panel can be initiated from a versatile set of precursors delivered from Earth or recovered from regolith through activation of mineral phases such as Ca/Na-$AlSi_3O_8$ with nucleophiles **(Fig. 2C).**[13] Of particular interest are non-hydrolytic Lewis acids or bases such as $B(C_6H_5)_3$ that can activate Si—O or Al—O bonds in silicates and aluminates **(Fig. 2C)**.[14]

In situ analysis of the Martian surface suggests up to 6 wt.% of volatile sulfur. Little is known about the chemical nature of sulfur binders, but a possible mechanism involves the diffusion of polysulfides across grain boundaries of regolith minerals, which activates the formation of covalent networks that reinforce relatively unreactive components. Assuming that sulfur can be extracted from troilite (FeS), it is a possible binder for Lunar or Martian regolith, albeit there is much that needs to be learned about the mechanistic origins of its cementitious properties.[15]

2.4 PRECURSOR DELIVERY

Whether for beneficiation or consolidation, Earth-sourced precursors to initiate chemical transformations must be delivered to Lunar or Martian surfaces at the appropriate locations and injected at the correct depths to maximize their benefits. Microencapsulation of precursors represents an attractive strategy to ensure the safe delivery of precursors and controlled release with precisely tunable propagation of reaction fronts and heat dissipation across the surface.[16,17] Microcapsules can be delivered within regolith at desired depth profiles by propelling them from a nozzle at prescribed velocities, thus enabling sequential reaction chemistry upon stress-, heat-, or impact activation as sketched in **Figure 3** and further illustrated in **Figure 4**.

Understanding chemical transformations and the surface chemistry of regolith and learning to deterministically drive 3D reaction fronts on extraterrestrial soils with a high degree of spatiotemporal control will be pivotal to permanent extraterrestrial bases, mining outposts, and a sustained human presence beyond Earth. This requires an atomistic understanding of reaction mechanisms in extreme, far-from-equilibrium environments through a combination of simulations, experiments on model systems, and *operando* studies of high-energy processes to enable another giant leap for mankind. The subsequent sections will describe progress towards our ambitious RAMS objective encompassing modeling, experiments, mechanistic studies, compositional and microstructural characterization, and scale models.

3. THERMITE REACTIONS FOR *IN SITU* PREPARATION OF ADVANCED HIGH-STRENGTH ALLOYS

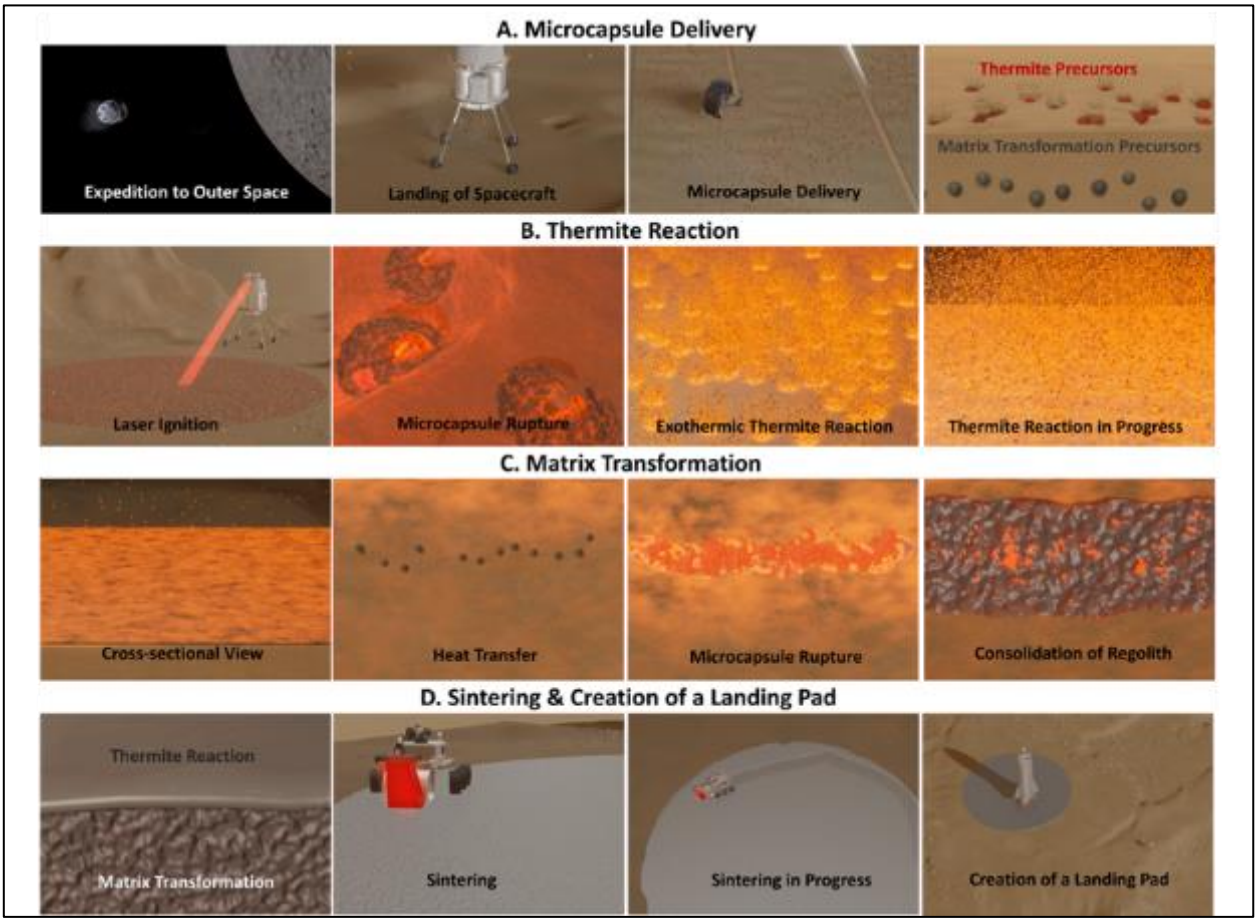

Figure 4. *Schematic depiction of RAMS process.* ***(A)*** *Microcapsules containing thermite and matrix transformation precursors are impelled into regolith.* ***(B)*** *A strongly exothermic thermite reaction initiated by Mg nanoparticles-activated upon impact—precipitates formation of advanced high-strength steel and Ti—Al—V alloys on the surface.* ***(C&D)*** *The released heat induces release and reaction of matrix transformation or geopolymerization precursors—silanes and bifunctional alcohols—that enable consolidation of regolith into load-bearing slabs. The sequence of images illustrates the approach of spacecraft, deployment of microcapsules at varying depths, formation of a subsurface slab, and a steel skin, thus enabling repeated landings and early settlements.*

Figure 4 shows a sequence of images illustrating our RAMS concept. The complete animation can be viewed at: https://www.youtube.com/watch?v=rtq-FE2BQ1k. Our initial step is the deployment of microcapsules containing thermite precursors to initiate the preparation of advanced high-strength alloys. Thermite reactions find widespread use in welding, metal refining, incendiary devices, etc. Such reactions are strongly exothermic and, once initiated, can be self-

sustaining across large areas. As such, they hold great potential for rapid deployment on Lunar and Martian surfaces at low external power budgets and with minimal earth-sourced precursors. Two model thermochemical reactions include:

$$Fe_2O_3(s) + 2\,Al(s) \longrightarrow Al_2O_3(s) + 2\,Fe(s) \qquad \Delta H^\circ_{298} = -849\ kJ/mole \qquad \ldots(1)$$

$$3\,Mg(s) + Fe_2O_3(s) \longrightarrow 3\,MgO(s) + 2\,Fe(s) \qquad \Delta H^\circ_{298} = -981\ kJ/mole \qquad \ldots(2)$$

Typically, Al is used in recovering molten metal for the different applications mentioned above. We've selected Mg as

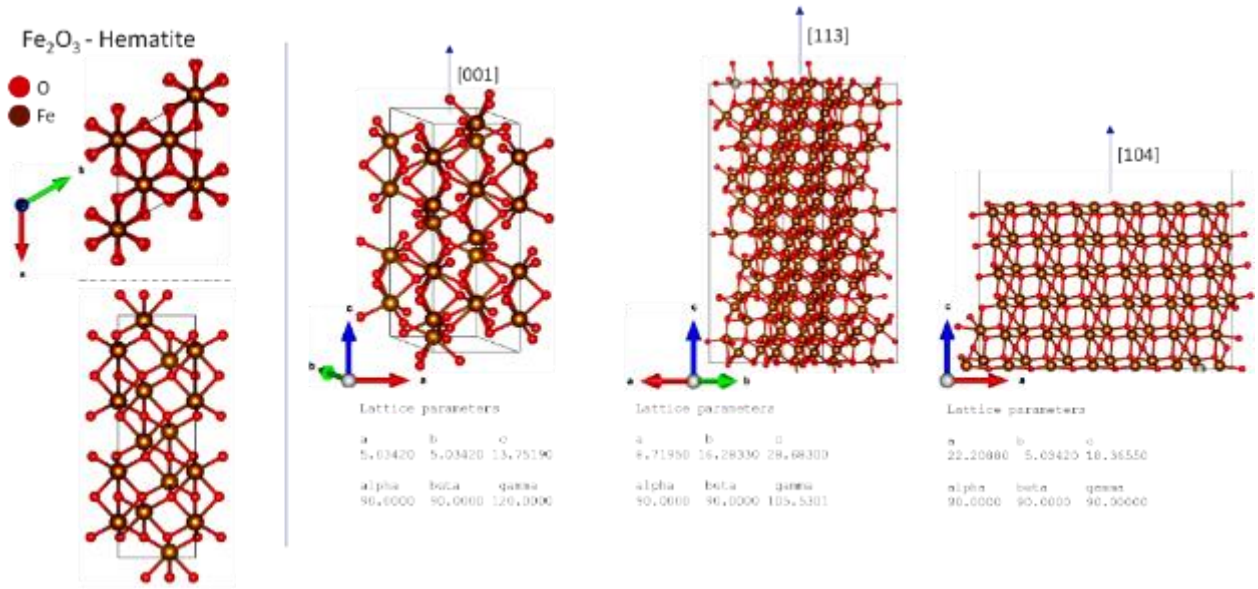

Figure 5. *Crystal structure (left), and three different surfaces of α-Fe_2O_3 examined for reactivity with Mg in ab initio molecular dynamics simulations.*

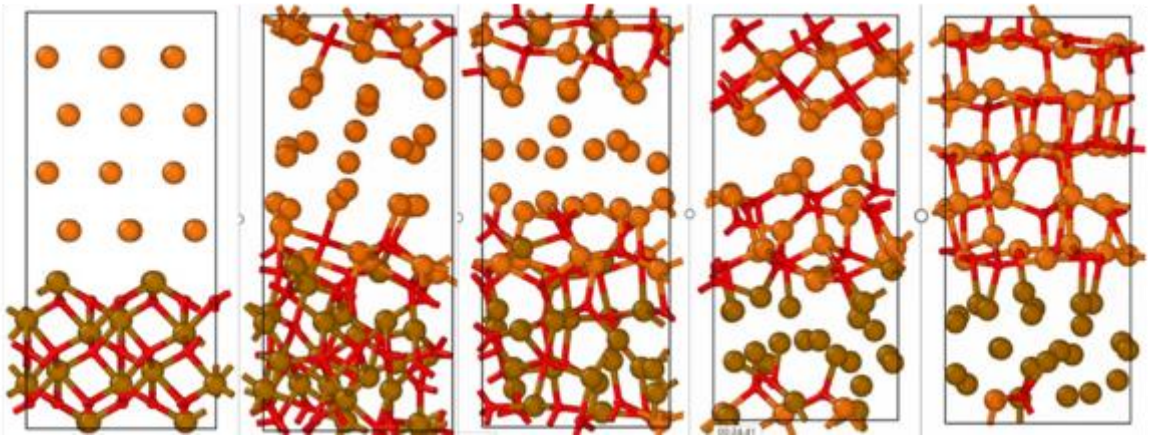

Figure 6. *Snapshots acquired during a 60 ps ab initio molecular dynamics simulation of Fe_2O_3(001)||Mg(001) reaction.*

our active precursor of choice given the higher energy released in thermite reactions, relatively lighter weight of the

material, favorable Ellingham diagrams that allow for the reduction of most regolith constituents down to the elemental metal under demanding vacuum conditions characteristic of extraterrestrial environments, and the ability to access Mg through *in situ* utilization of Martian or Lunar regolith as illustrated in **Figure 2**.

Ellingham diagrams show that Mg can reduce all but calcium oxides down to their metallic form, rendering it a beneficial agent for initiating *in situ* metal recovery. We envision the initial delivery of thermite precursors to build landing pads and initial scientific and mining outposts, which in turn will be activated to ensure the harvesting of metallic Mg from regolith, enabling widespread application of the chemistry developed in this project to build the fundamental infrastructure needed for repeated landings and human habitation.

3.1. Molecular Dynamics Simulations of Thermite Reactions

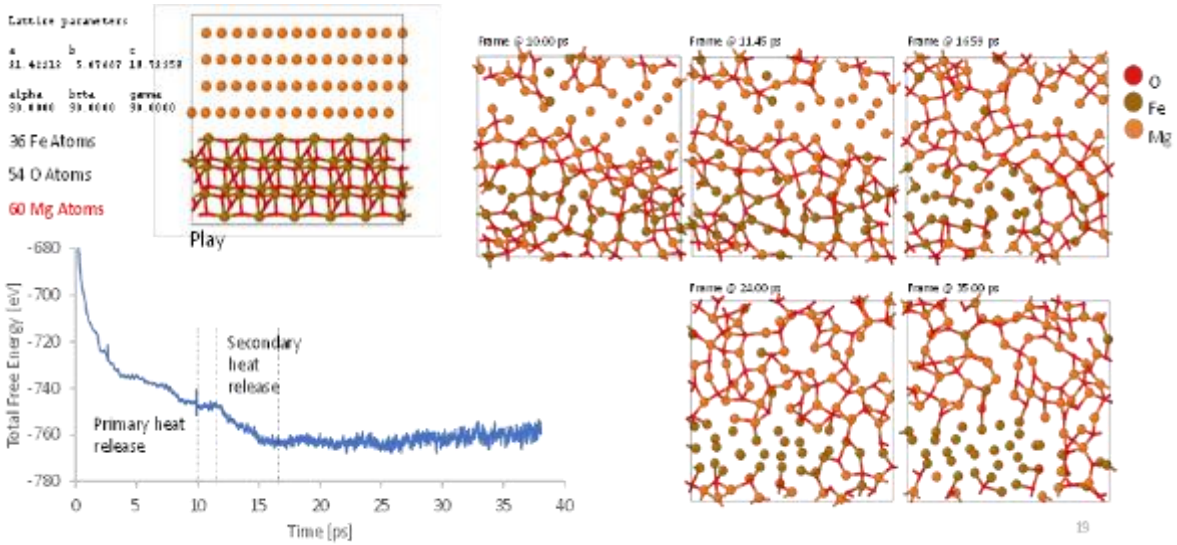

***Figure** 7. Snapshots acquired during a 60 ps ab initio molecular dynamics simulation of Fe_2O_3(104)||Mg(001) reaction indicating sequestering of molten iron by MgO and two distinctive heat release regimes.*

Extensive *ab initio* molecular dynamics simulations have been performed to examine the reaction of Fe_2O_3 (as a model component of regolith) with Mg particles. The reactivity of Fe_2O_3 shows some parallels to that of ilmenite, which is abundant in specific sites on the lunar surface. In the simulations, we examine the reactivity of different exposed surfaces of Fe_2O_3 with various surfaces of Mg. The simulations provide direct insight into varying heat release profiles, formation of passivation layers, and illustrate the paramount role of oxide diffusion. As such, these simulations provide essential quantities needed for continuum simulations of heat release across macroscopic scales needed to deterministically guide reaction fronts along specific areas of the lunar/Martian surface. **Figure 5** shows the crystal structure of Fe_2O_3 and the different crystal surfaces examined in our simulations based on lattice compatibility with Mg. This figure illustrates interfaces where reasonable interfacial contact can be established (<5% lattice mismatch across the interface) enabling the initiation of the thermite reaction.

Figure 7 shows snapshots along a 60 ps NVT-AIMD reaction simulation for the $Fe_2O_3(001)||Mg(001)$ thermite reaction indicating oxide diffusion and segregation of iron, a precursor to steel formation, which ultimately crystallizes into an

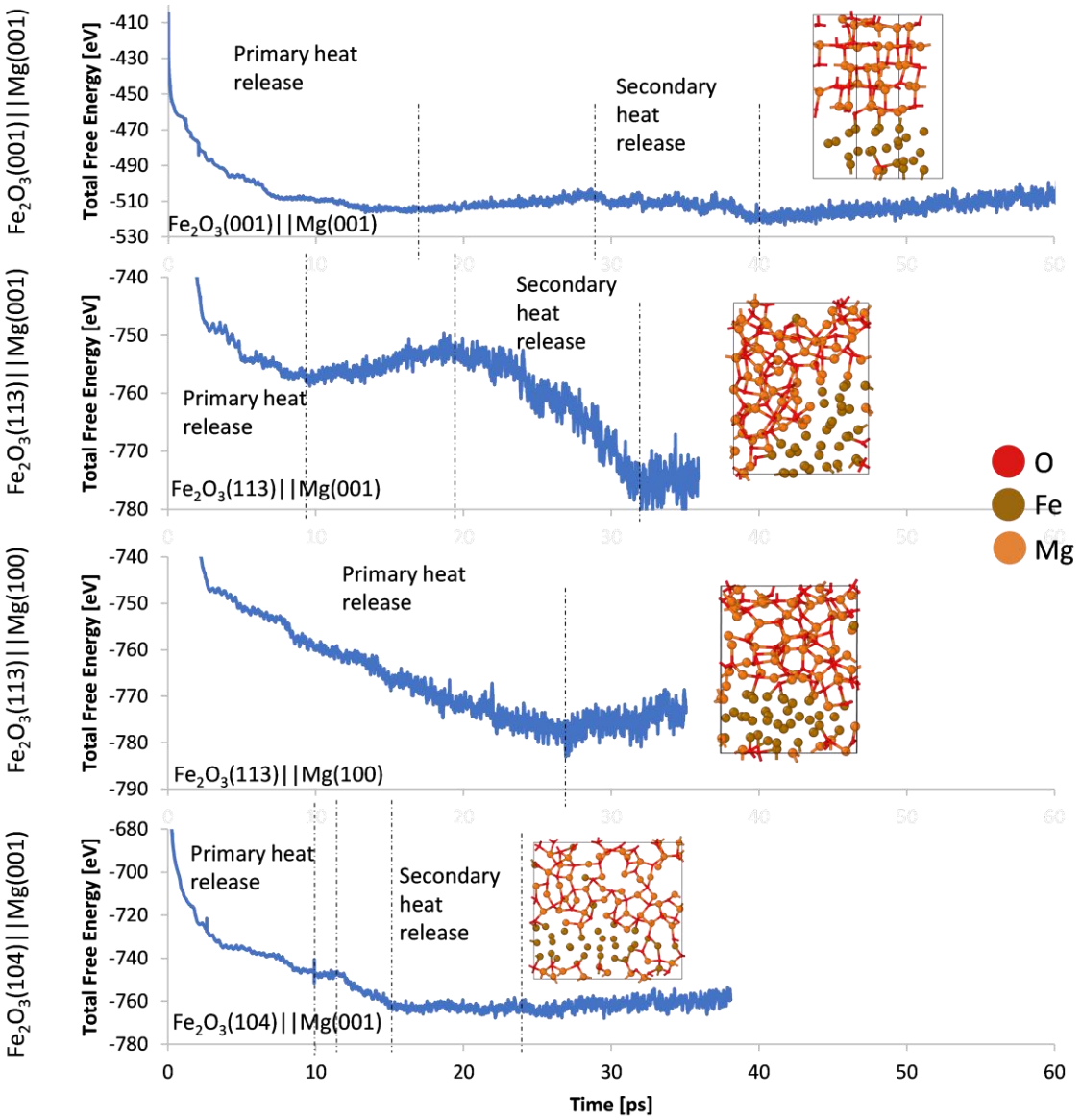

***Figure 8**. Final product configurations and heat release profiles for different facets of Fe_2O_3 reacted with Mg in a thermite reaction to recover Fe or advanced high-strength steel.*

ordered configuration. The graphic illustrates the distinctive regimes, interfacial reaction, anion diffusion, and

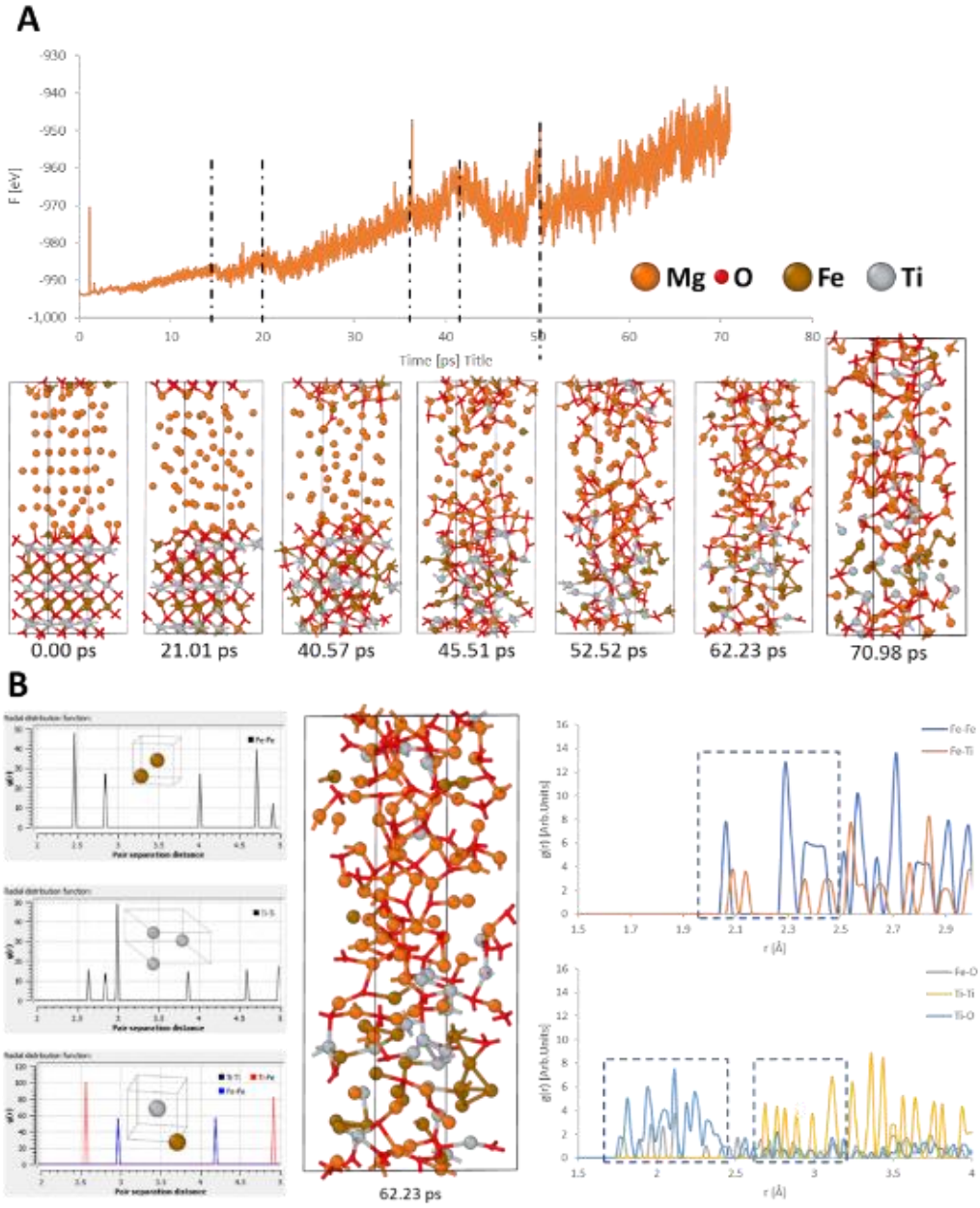

Figure 9. Heat ramp (33 K/ps) AIMD simulation of the Mg/FeTiO3 nanothermite system*: **(A)** Free energy profile for system Mg/FeTiO3 throughout a heat ramp from 10 to 3000 K. The inflections highlighted with the black dotted vertical lines correspond phase transitions triggered by oxygen diffusion towards the mg phase. Selected frames at the bottom illustrate the oxygen diffusion leading to MgO formation and reduction of the Fe and Ti species. **(B)** Partial radial distribution functions (PRDF) for the crystalline systems, iron, titanium, and iron-titanium compared to the PRDF profiles for the Mg/FeTiO3 system after 62.23 ps heat ramp. The Fe-Fe and Ti-Ti peaks between 2.0 and 2.5 Å evidence the Fe-Fe and Ti-Ti aggregation.*

crystallization and suggests that careful control of heat release in this sequence of reactions can be used to obtain molten

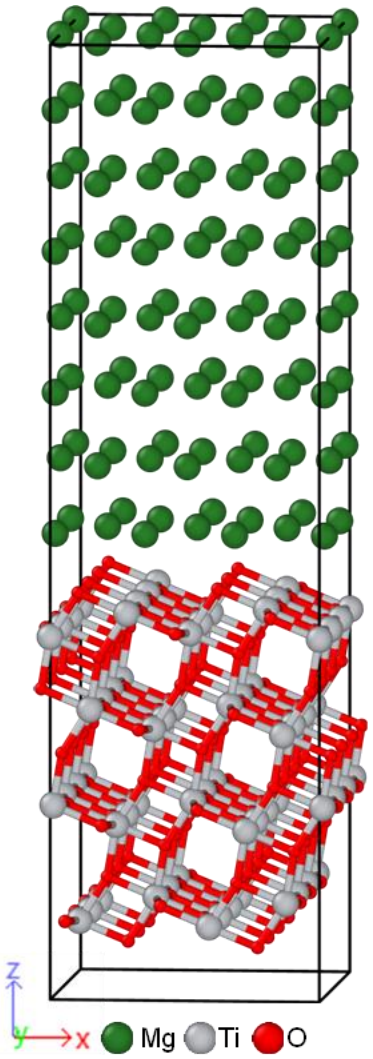

Figure 10: *Initial configuration TiO2(101)||Mg(0001)*

iron, which can be further alloyed to access advanced high-strength steels. **Figure 8** shows analogous data for the different facets (such as $Fe_2O_3(104)||Mg(001)$) of thermite reaction indicating two distinctive heat-release regimes, which can potentially be harnessed to (a) initially propagate thermite reactions and (b) active-matrix transformation reactions in the subsurface to form a consolidated regolith slab as envisioned in **Figure 4**.

The set of AIMD simulations in **Figure 9** shows the heat release profile of the $Mg/FeTiO_3$ nano-thermite system needed to elucidate the reaction front dynamics and illustrate the oxygen diffusion mechanism that triggers the Mg oxidation that produces the reduced Fe and Ti clusters.

Ongoing work is focused on exploring the effect of varying the heat ramp rate on the reaction between Mg nanoparticles and titanium dioxide (initial configuration shown in **Figure 10**). Additionally, investigating the impact of different crystal orientations and sizes of the simulation cell is under investigation and will provide valuable insights into the role of interfacial effects and surface chemistry on the formation of passivation layers. Furthermore, studying the reaction kinetics and the effect of different environmental conditions, such as pressure and gas composition, can lead to a comprehensive understanding of the thermite reaction mechanism. Many of our initial predictions are concordant with and have been validated by experimental findings as will be discussed below.

3.2. Laboratory-Scale Thermite Reactions and Discovery of Hard Metallic Composites

3.2.1 Methods and Materials

LMS-1 (Lunar Mare Stimulant-1) regolith simulant (a coarse powder) was obtained from the Exolith lab. Based on the ASTM C136 standard test method for sieve analysis of fine and coarse aggregates, **Figure 11A** illustrates the cumulative particle-size distribution curve for LMS-1 stimulant. A 2.5 mL polystyrene vial of LMS-1 powder was ball-milled with methacrylate balls for 30 minutes prior to use for thermite reactions. High-energy ball mills with dual clamps (8000D Mixer/Mill) were used for ball milling. Mg and TiO_2 from Sigma Aldrich and Fe_2O_3, $FeTiO_3$, SiO_2, and graphite crucibles purchased from Etsy were used as received.

An uniaxial hydraulic press (Carver) was used to compact the thermite mixtures into cylindrical pellets of 5 mm in diameter and 2—5 mm in height. In order to carry out the thermite reaction, a windowed plexiglass chamber (diameter 60 cm, height 80 cm) was placed inside a 60" × 72" plastic glove box (**Figure 11B**). In order to perform the reactions, an argon gas cylinder and vacuum pump were attached to the glove bag.

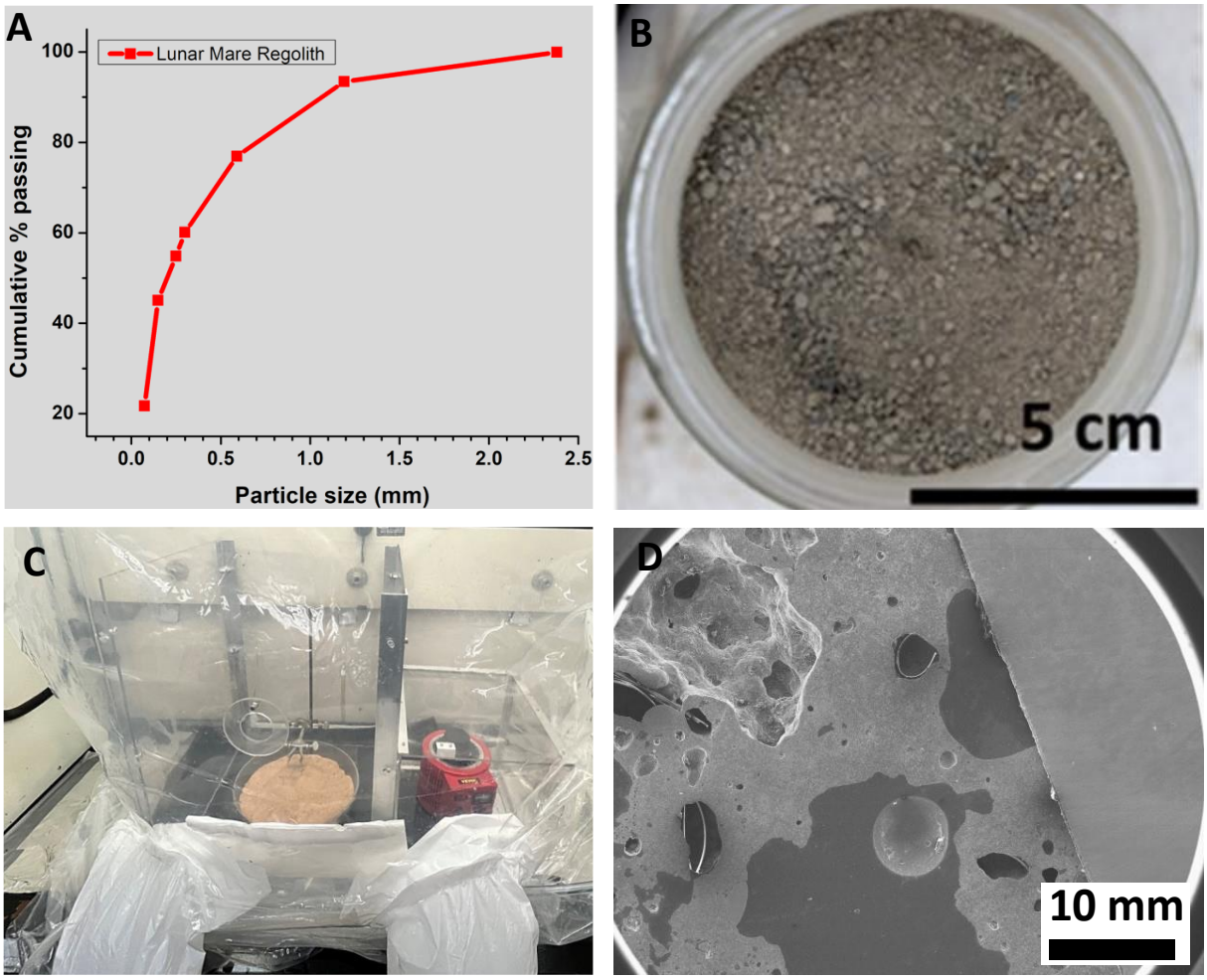

Figure 11. ***(A)****The cumulative particle-size distribution curve of the LMS-1 Stimulant on the left. Right panels shows a digital image of the LMS-1 regolith.* ***(B)*** *Laboratory setup for performing thermite reactions.* ***(C)*** *Polished sample surfaces for SEM-EDX analysis.*

The experiments were performed under controlled conditions in an argon environment at a pressure of 1 atm (14.7 psi), as depicted in **Figure 11B**. The pellet was carefully placed within a graphite crucible inside the chamber and ignited at the bottom using a tungsten wire, which was operated with a Variac to maintain a steady flow of current. Upon completion of combustion, the product was ground with a mortar and pestle into a fine powder. Powder X-ray diffraction and scanning electron microscopy (SEM) were used to determine the composition and morphology of the product. EDX analysis was conducted using the JEOL JSM-7500F, which enabled the identification of the sample's elemental composition. Prior to

imaging, it is essential that the sample is both homogeneous and flat in order to ensure accurate quantitative EDX analysis. An alumina/diamond slurry (made up of particles of up to the size of one micron) was used to polish the samples. A micrograph of the polished surface is shown in **Figure 11C**, which illustrates the flatness and uniformity of the sample.

3.2.2 RESULTS AND DISCUSSION

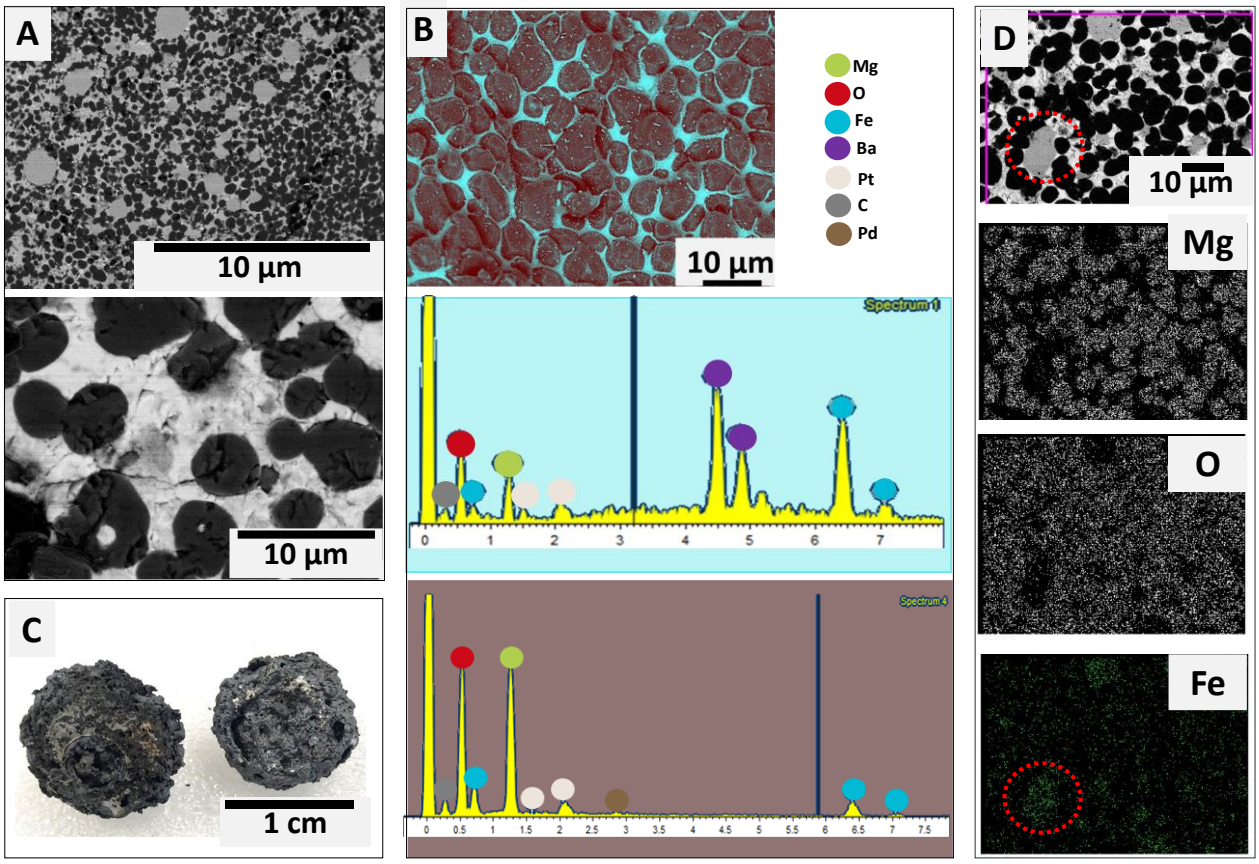

Figure 12. Characterization of reaction products of Fe_2O_3 and Mg thermite reaction. ***(A)*** *Backscattered electron SEM image of MgO micro-inclusions embedded within a continuous steel matrix.* ***(B)*** *EDX spectra acquired in two different regions. The inset shows a polished cross-section of the surface. Microstructure of obtained hard consolidated slab showing well-defined fused grains.* ***(C)*** *Digital photographs of hard sintered slabs.* ***(D)*** *EDX maps obtained for polished cross-sections showing embedded MgO particles within a continuous Fe matrix.*

In this study, we present an elemental composition and phase analysis of the products of thermite reactions. Specifically, we have examined the reaction between magnesium and ferrous oxides; the latter serve as proxies for iron-containing compounds found in the lunar regolith. We have particularly emphasized approaches that yield molten metal or alloy in its elemental form as a means of realizing the steel skin concept of RAMS. Based on our reactions, we have gained valuable insight into the metal/alloy extraction and consolidation from lunar regolith, which provides access to critical load-bearing components of lunar infrastructure.

A recurrent motif observed in products of thermite reactions with ferrous oxides are MgO particles embedded within a matrix of molten iron. **Figure 12A-D** shows back-scattered scanning electron microscopy images and EDX maps illustrating MgO particles embedded within a continuous Fe matrix. Owing the high temperature of the self-sustaining thermite reaction,[18] the molten metal crystallizes with a well-defined interconnected grain structure embedding MgO particles. A digital photograph of the hard macroscopic core recovered from the thermite reaction is shown in the **Figure 12C**. **Figure 13** shows a laboratory-scale thermite reaction between Fe_2O_3 and Mg. During the thermite combustion, most of the melted product coalesces to form a solidified consolidated product. The densified core recovered from the reaction (shown in **Figure 13**) is strongly magnetic as a result of the formation of a continuous Fe matrix. Refinements of poweder X-ray diffraction patterns further indicate that the MgO-embedded iron metal matrix contains about 31.6 wt.% Fe and 68.4 wt.% MgO.

Key Conclusion 1: The formation of a steel slab with a sintered microstructure evidenced here provides an important proof-of-concept demonstration and illustrates the hard consolidated regolith component that can be accessed from thermite reactions and used as a structural material.

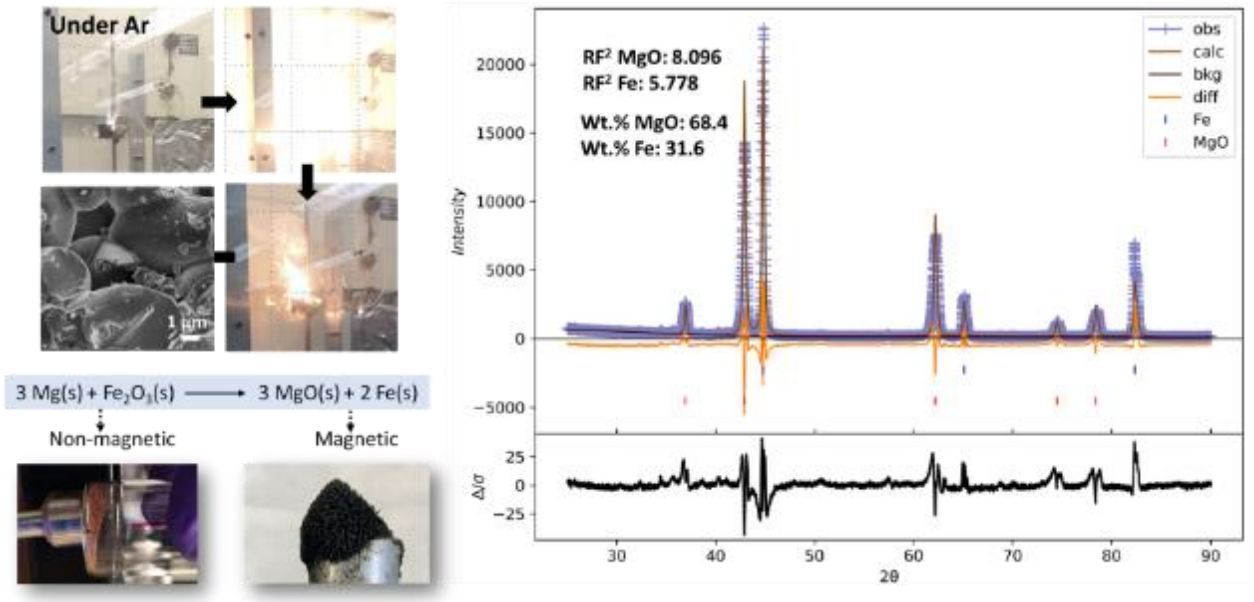

Figure 13. From left to right. Laboratory scale reaction of Mg with Fe_2O_3. *A hard sintered magnetic residue is obtained. Rietvield refined X-ray diffraction pattern indicates MgO embedded iron matrix tat contains about 31.6 wt.% Fe and 68.4 wt.% MgO.*

Mineral/ metals oxides	First major product	Second major product	The physical form of the product
Fe_2O_3	MgO	Fe	Solid
FeO	MgO	Fe	Solid
Fe_3O_4	MgO	Fe	Solid
TiO_2	MgO	Mg_2TiO_4	Powder
SiO_2	MgO	Mg_2SiO_4	Powder
V_2O_5	MgO	Mg_2VO_4	Solids and Powder
Al_2O_3	MgO		Solids and Powder
$FeTiO_3$	MgO	$BaTiO_3$	Solids and Powder
$(Mg,Fe)SiO_4$	MgO	Mg_2SiO_4, FeTi	Powder
$TiO_2+Fe_2O_3$	MgO	Mg_2TiO_4	Powder
$TiO_2+Fe_2O_3+Al_2O_3$	Fe0.3Mg0.7O	$AlBaO_4$, Fe	Powder
$V_2O_5+Fe_2O_3$	MgO	Fe3O4/BaO	Solids and Powder
Magnetic regolith	FeTiO3	Mg_2SiO_4	Powder

Table1: *Major reaction products recovered from the thermite reaction of various metal oxides with Mg*

A variety of such stoichiometric mixtures at the laboratory scale have been attempted using model components of lunar regolith and regolith simulants. **Table 1** summarizes the results in terms of primary and secondary products identified by X-ray diffraction and the physical state of the products.

Figure 14 shows micrographs and EDX maps of promising sintered reaction products obtained from ilmenite, which is found in reasonably high abundance in Lunar regolith. The formation of a continuous Ti/Fe matrix illustrates the excellent transferability of our Mg thermite concept from model systems to actual constituents of lunar regolith. X-ray diffractograms in **Figure 14B** show the changes in the bulk products formed in the ilmenite thermite combustion. The product contains some minor phase fractions that might not have reacted entirely. We observe a similar product profile in

the molecular dynamics simulation, as shown in **Figure 9**. **Figure 9A, C-D** details the formation of a molten metal/alloy matrix that embeds the MgO grains. The products are readily attracted to a magnet. They can be separated from unreacted powder materials based on density differentials or with the help of a hard magnet (see schematic in **Figure 4**), thereby yielding a hard metallic composite material immediately applicable for infrastructure applications.

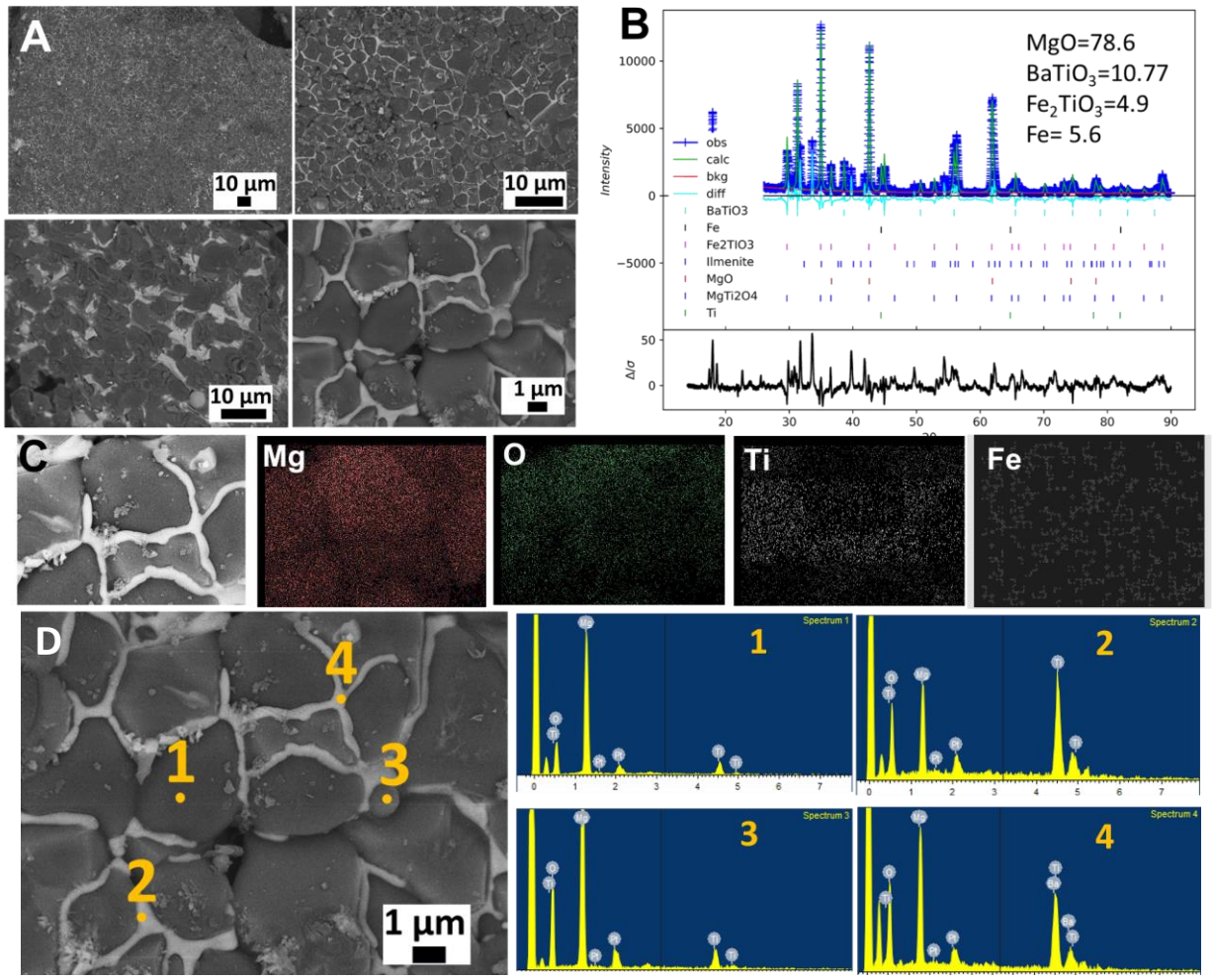

Figure 14: *Characterization of products of thermite reactions of Mg with ilmenite.* ***(A)*** *Microstructure of recovered products,* ***(B)*** *Rietveld refinements to powder X-ray diffraction patterns,* ***(C)*** *EDX maps, and* ***(D)*** *EDX spectrum are shown illustrating the formation of a continuous Ti/Fe matrix encapsulating MgO and Fe-Ti oxide particles.*

Some other abundant and valuable metal oxides in the regolith composition are SiO_2 (46.9 wt.%), Al_2O_3 (12.4 wt.%). and

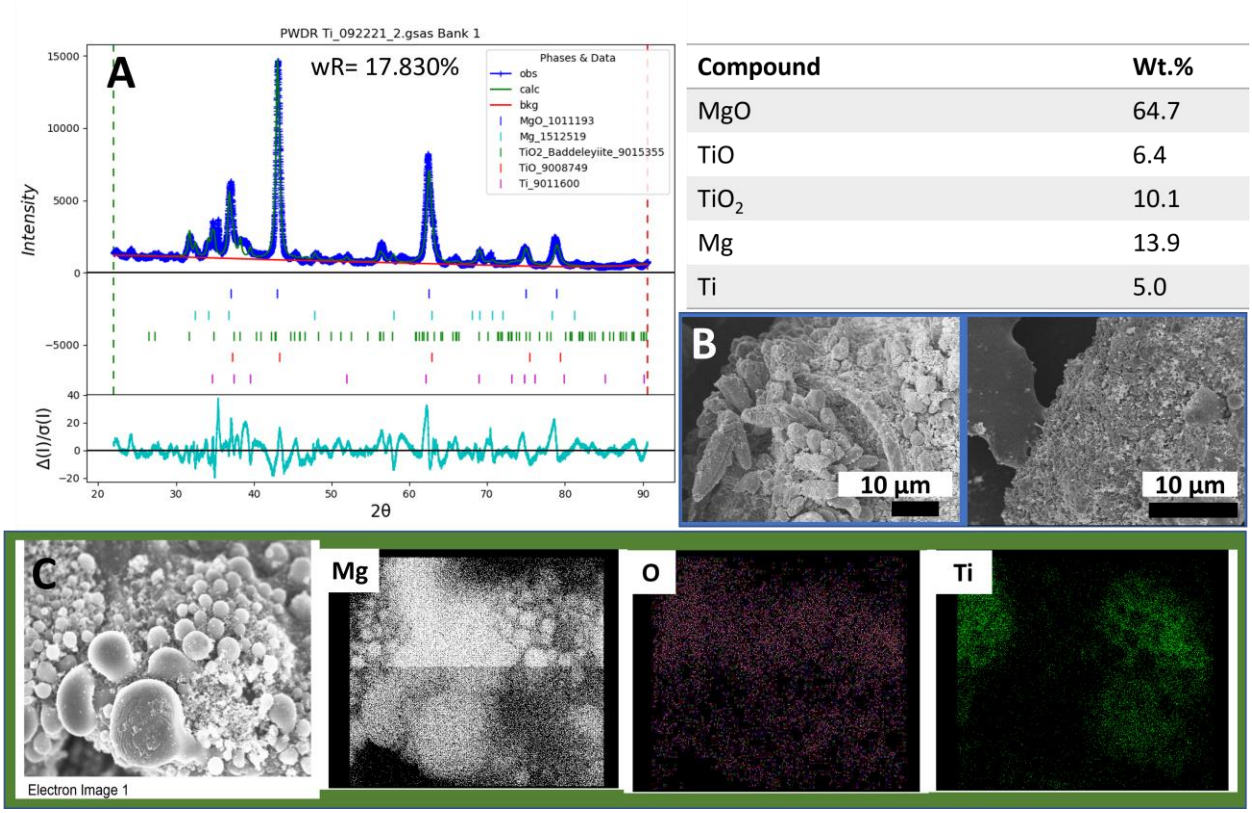

Compound	Wt.%
MgO	64.7
TiO	6.4
TiO_2	10.1
Mg	13.9
Ti	5.0

Figure 15: *Characterization of products of thermite reactions of Mg with TiO_2 in air.* ***(A)*** *Rietveld refinements of powder XRD pattern,* ***(B)*** *scanning electron micrographs,* ***(C)*** *EDX map illustrating the formation of a reduced TiO_2 to TiO and Ti matrix and oxidized Mg to MgO matrix.*

TiO_2 (3.6 wt.%). **Figures 15—17** show characterization of productions of thermite reactions between TiO_2, SiO_2, and Al_2O_3 with Mg, respectively. The recovered materials have been characterized using XRD refinements; EDX maps show a reduction of respective metal oxide and oxidation of Mg.

The X-ray diffraction pattern in **Fig. 13A** shows that the reaction products from bulk ignition of the Mg–TiO_2 mixture in the air are MgO, Ti/TiO, and some unreacted TiO_2 and Mg. The XRD pattern (not shown) for Mg–TiO_2 mixture under argon does not produce a stable combustion mixture and remains essentially unreacted. This could be because Mg requires a higher initial energy input to reach combustion temperatures under inert conditions. Ongoing efforts are focused on the addition of oxidizers to the reactant mixture to reach high combustion temperatures needed to react titanium oxides.

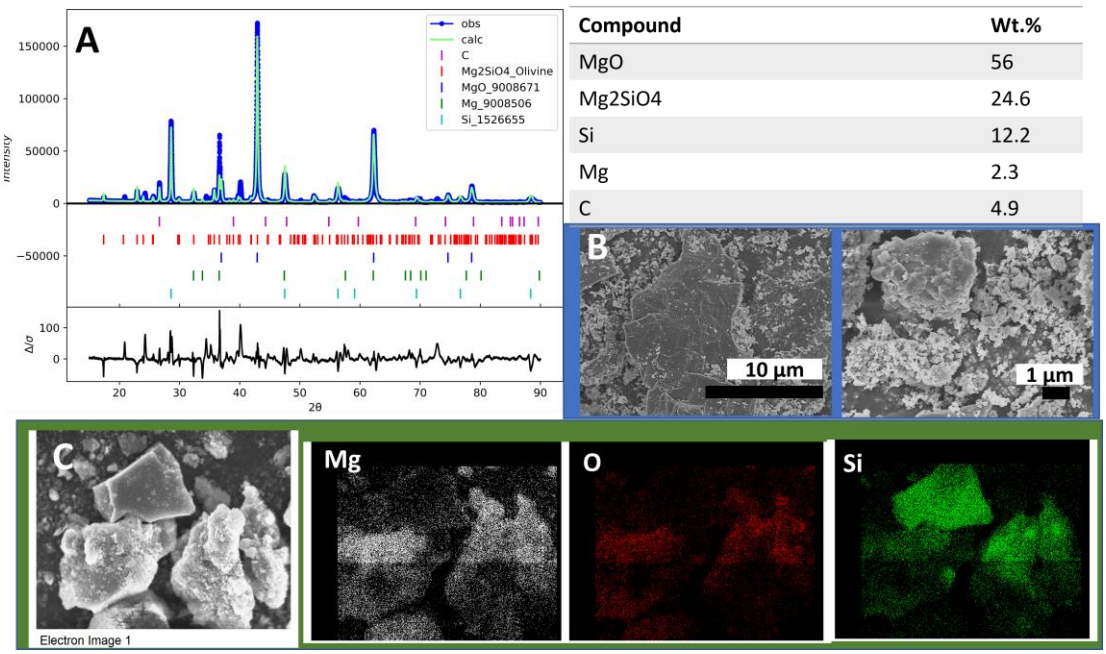

Compound	Wt.%
MgO	56
Mg2SiO4	24.6
Si	12.2
Mg	2.3
C	4.9

Figure 16: *Characterization of products of thermite reactions of Mg with SiO_2.* ***(A)*** *Rietveld refinements of powder XRD patterns,* ***(B)*** *scanning electron micrographs of the recovered prducts,* ***(C)*** *EDX maps illustrating the formation of a reduced SiO_2 and oxidized Mg matrix.*

We observe a similar pattern with SiO_2 and Al_2O_3, as shown in **Figure 16** and **Figure 17**, respectively. The reaction products from Mg–SiO_2 mixture in the air are MgO, Mg_2SiO_4, Si, and weak identification of unreacted Mg. While from

$Mg–Al_2O_3$ mixture, we observe MgO and complex Al-Mg oxides that are difficult to refine/characterize.

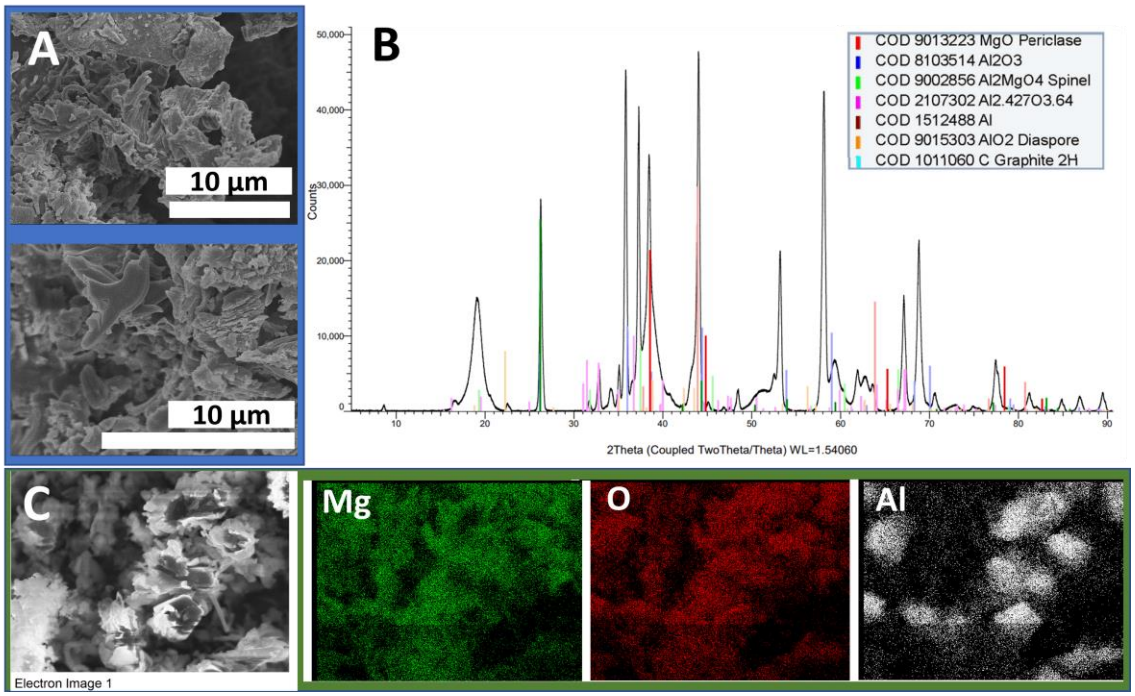

Figure 17. *Characterization of products of thermite reactions of Mg with Al_2O_3.* ***(A)*** *Scanning electron micrographs of recovered reaction products* ***(B)*** *XRD pattern and,* ***(C)*** *EDX maps illustrating the formation of a reduced form of Al_2O_3 and oxidized MgO matrix.*

Our experiments further reveal that the strength of the combustion products in SiO_2 and TiO_2 is insufficient for use as load-bearing materials based on the physical state of the product. However, it would be interesting to investigate how this behavior changes when a small amount of Fe_2O_3 or Ilmenite is added to the reaction mixtures. Based on our observations, an iron-rich phase can essentially aid in the formation of a high-strength load-bearing matrix wherein other less reactive components are embedded. Nano-indentation investigations on Fe-rich products are part of our ongoing research to determine the material's strength. Our future goal is to deduce the reaction paths based on XRD that allows the formation of densified elemental metal from different metal oxides. This will eventually help us achieve increased reactivity of lunar regolith components (or self-propagating high temperatures) in thermite reactions.

We are now also working on the magnetic characteristics of thermite products, which could be useful for detecting the presence of thermite products. Because the magnetic characteristics are controlled by the size and distribution of the metal particles formed in the reaction, magnetic susceptibility measurements are further expected to provide insight into the microstructure of the thermite product.

Additionally, in the future, we intend to use nanoindentation to explore the mechanical properties of our thermite products. The process of nanoindentation can provide useful information about the mechanical properties of materials at the nanoscale level. Nanoindentation can test attributes such as hardness, modulus, and toughness by indenting the surface of

the material with a well-defined. This will assist us in understanding how the each component of the regolith affects the mechanical properties of our overall thermite products and what components have potential applications for structural materials.

Simulations have further proven to be beneficial in deducing these reaction paths. **Figure 8** shows the final products and heat release profiles of different surface planes of Mg with Fe_2O_3. The results illustrate the promise of using differently shaped Mg particles to control both the extent of conversion and the specific heat release profile and are the subject of active research in our project.

3.3. PALETTE OF THERMITE PRECURSORS

Our selection of Mg as a precursor is further informed by our distinctive ability to stabilize Mg particles of different geometries and with different exposed surface facets. As per the molecular dynamics simulations in Section 3.1, this will enable tunability of heat release and control of embedded MgO/Fe microstructure. **Figure 18** shows different Mg precursors available to us from the chemical and electrochemical reduction of Gringnard's reagents in the presence of different capping ligands.

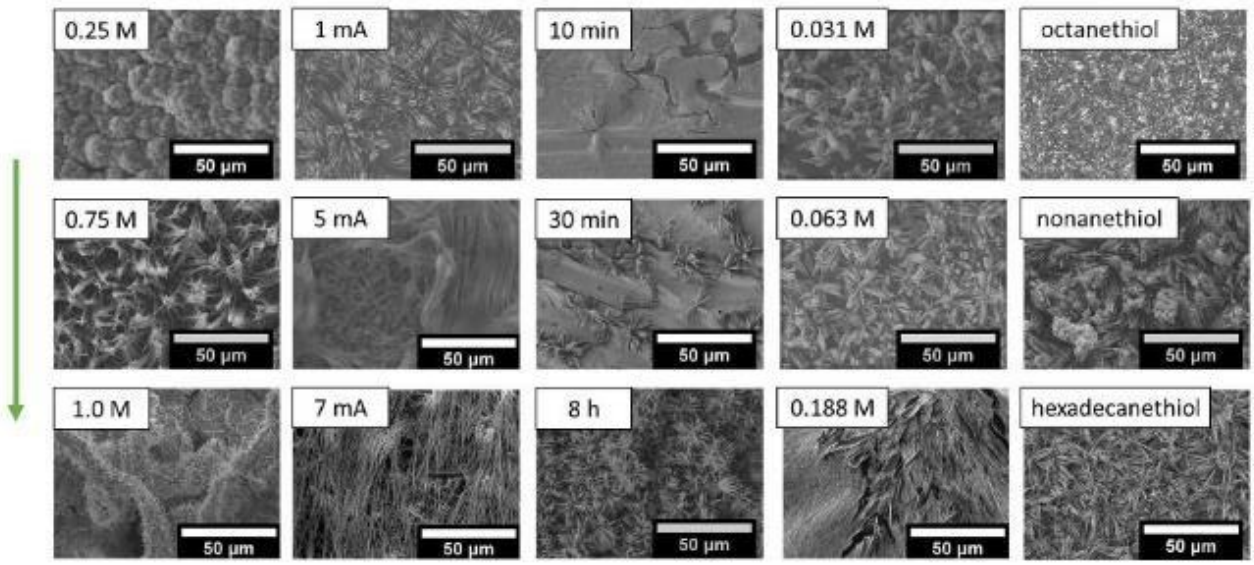

Figure 18. *Reaction conditions for stabilization of Mg particles of different geometries and surface planes.*

4. REGOLITH CONSOLIDATION THROUGH MATRIX TRANSFORMATION

4.1 SOLIDIFICATION AND 3D PRINTING OF LUNAR REGOLITH

We describe here a versatile approach for consolidating a regolith simulant through forming siloxane networks enmeshing mineral particles by surface dissolution—precipitation reactions. The composite formulations are then used as feedstock for 3D printing into near-net-shape load-bearing objects.

Soil topographical transformation techniques include methods such as polymerization and solidification through crosslinking.[12,13] In the former, alumino-silicates form a three-dimensional network upon activation under typically alkaline conditions. The critical underlying mechanism is the complete dissolution of alumino-silicates into monomers, dimers, and trimers, followed by the rapid hardening of the produced slurry through the formation of a 3D alumino-silicate network.[19] The incipient network comprises diverse polysialates ranging from poly(sialates) to poly(sialatedisiloxo) moieties depending on the Si/Al ratios and the alkali species used.[20] Increased compressive strengths are obtained when there is a higher ratio of 3D bonding motifs as compared to 2D sheets and chains.

In contrast, solidification through matrix transformation involves the formation of a crosslinked matrix holding together individual particulates of the soil rather than the direct dissolution and reconfiguration of alumino-silicate frameworks. This includes a variety of applications where a silica precursor is added and initiates a series of polycondensation reactions.[21] Several alternative crosslinkers can additionally be incorporated to form a more robust interlinked network. Combining these processes provides a means of obtaining consolidated reaction products wherein surface dissolution and recombination yield a network of necked particles. This occurs upon adding small quantities of water or alcohol or under modest excursions from neutral pH, which promotes surface dissolution. The surface dissolution and reprecipitation bring about the necking of adjacent particles as capillary pressure draws the particles together.[1,22,23] Unlike bulk diffusion and reconfiguration in geopolymerization, matrix transformation allows for the necking of individual particles through surface

diffusion, resulting in a much lower energy input than bulk diffusion.[24,25] Furthermore, a relatively lower liquid content is sufficient since the complete dissolution of the minerals is not necessary to form necked networks.

Mineral-derived building materials produced on Earth require large amounts of water and substantial energy expenditure, which precludes their deployment in extraterrestrial bodies.[6,12] Sustainable construction with minimal waste production requires not just topographical transformation of regolith, such as through geopolymerization and crosslinking, but also the structuring of regolith into load-bearing structures. The latter can be achieved with the considerable economy of materials used with the help of additive manufacturing techniques such as extrusion-based 3D printing.[26,27] Such techniques can be coupled with generative design to yield complex shapes and forms, inaccessible using conventional construction methods, which minimize materials use and imbue additional functionality.[28] For instance, the generative design allows for minimizing a structure to its fundamental load-bearing components resulting in mass reductions approaching 25—75%.[29] However, the 3D printing of lunar regolith formulations in a manner that realizes the promise of generative design remains to be developed.

Several characteristics must be considered when considering the feedstock design for additive manufacturing. The feedstock must be readily extrudable through a printer's nozzle, adhere to subsequent layers, and support the weight of subsequent layers.[30,31] These characteristics depend on a combination of rheological and interfacial properties, which can be mapped to density, viscosity, particle size, wettability, and crosslinking kinetics. The printability, pumpability, and buildability (mechanical strength) of formulations must be optimized in order to produce a functional feedstock. As such, the interfacial reactivity and particulate dimensions of lunar regolith must be understood to enable judicious selection of crosslinking chemistries and the design of formulations with the appropriate rheology to yield printed structures that support the weight of and adhere to subsequent layers of extruded material. Matrix transformation represents an ideal candidate for incorporation with additive manufacturing to facilitate construction on the lunar surface using primarily locally sourced materials. This article combines regolith with small amounts of water, hydroxyethyl cellulose, sodium silicate, and ammonium hydroxide to form a sintered network of regolith particles at a low energy input. The consolidated regolith is further reinforced through silica and hydroxyethyl cellulose crosslinking between necked particles. In addition to limiting the number of Earth-based additives used in the matrix transformation process, the recoverability of these additives can significantly increase the efficiency and feasibility of this process. While the consumable materials directly used in crosslinking the regolith particles cannot be recovered after printing, the liquid phases, including water, isopropanol, and ammonium hydroxide, can be quickly recovered through condensation of the evaporated solution.

4.2 Materials and Methods

Regolith solidification was conducted by mixing lunar mare simulant (Exolith Labs LMS-1) with hydroxyethyl cellulose (Sigma Aldrich), DI water (ρ = 18.2 MΩ-cm using a Barnstead International NANOpure Diamond system), 35—40 wt.% aqueous solution of Na_2SiO_3 (Spectrum Chemical Mfg.), 2-propanol ($\geq$99.5%, Fisher Scientific), glycerol ($\geq$99%, Sigma Aldrich), and NH_4OH ($\geq$95%, Fisher Scientific) under ambient conditions in weight ratios given in **Table**

1. Four formulations F1—F4 are compared in this study with each formulation being made through the combination of the regolith simulant, hydroxyethyl cellulose, DI water, Na_2SiO_3, 2-propanol, and glycerol using a KitchenAid mixer. NH_4OH was added and mixed using the KitchenAid mixer for 5 min and then the formulations were placed into rubber molds with varying dimensions. Sample mixtures were then left to air dry in rubber molds for 4—6 days in a fume hood. Solidified samples were cut into 1 cm × 1 cm slabs using a Dremel rotary tool.

Solidified regolith slabs were polished on an Economet 3 variable speed grinder-polisher using silicon carbide sandpaper. Sandpaper of increasing fineness was used (320, 600, 1200, 2400 grit) on the polished face of each sample; the thickness of each sample was reduced to ca. 1.0 mm by sanding the inverse face using coarse sandpaper.

Formulation	**F1**	**F2**	**F3**	**F4**
Mare Regolith	10.0 g	10.0 g	10.0 g	10.0 g
Hydroxyethyl cellulose	1.0 g	1.0 g	1.0 g	1.0 g
DI Water	0 Ml	1.0 mL	1.0 mL	2.0 mL
Na_2SiO_3	3.50 mL	3.50 mL	3.50 mL	3.50 mL
2-propanol	1.0 mL	1.0 mL	2.0 mL	2.0 mL
Glycerol	1.0 mL	1.0 mL	2.0 mL	2.0 mL
NH_4OH	1.0 mL	1.0 mL	2.0 mL	2.0 mL
Solid Vol.%	55.4%	51.9%	43.5%	41.3%
Density before curing [g/mL]	1.54	1.69	1.51	1.53
Density after curing [g/mL]	1.63	1.65	1.71	1.74

Shrinkage Vol.%	19.0%	24.2%	32.5%	39.2%

Table 2. Formulations used in the matrix transformation of lunar mare regolith

4.3 CHARACTERIZATION OF CONSOLIDATED REGOLITH

Powder X-ray diffraction (XRD) measurements were performed on the individual formulations using a Bruker D8-Focus Bragg Brentano X-ray Powder Diffractometer with a Lynxeye PSD detector and a copper Kα source (λ = 1.5418 Å).

29Si and 27Al solid-state magic-angle spinning nuclear magnetic resonance (MAS-NMR) measurements were performed for mare regolith formulations before and after modification using a Bruker AVANCE NEO 400 instrument. The frequency was set as 79.50 MHz, MAS rotation rate as 5 kHz for 29Si; the corresponding values were 104.28 MHz and 5 kHz for 27Al NMR measurements. All samples were ground into a fine powder before recording NMR spectra.

Scanning electron microscopy (SEM) was performed on lunar mare regolith before and after modification. SEM images were acquired using a JEOL JSM-7500F at a 5 kV accelerating voltage and 10.50 μA emission current. All samples after modification were polished before imaging (vide infra).

Fourier transform infrared (FTIR) spectroscopy was performed on solidified regolith formulations by first grinding the regolith into a fine powder, which was analyzed in attenuated total reflectance (ATR) mode using a Bruker Vertex 70 FT-IR spectrometer equipped with a SiC globar as a MIR radiation source. A Pike Technologies MIRacle ATR accessor with a diamond single reflection plate was used for the measurements.

Nanoindentation was performed using a Hysitron TI 950 Triboindenter. Testing was performed on solidified and polished regolith specimens. Three 10 × 10 grid indents were performed with a grid spacing of 10 μm, measuring the displacement under a loading force from 0—1000 μN.

Compressive strength was measured using cylinders of solidified regolith with an average height of 92 mm and an average diameter of 45 mm using an Instron 5984 universal testing machine at a strain rate of 1% per minute.

Density measurements were acquired for F1—F4. The weights of the modified regolith were measured using an analytical balance immediately after preparation and then after the samples were fully cured. Measurements of volume were conducted by packing formulations into a cubic mold.

In order to investigate the flow and printability properties, the viscosity of formulations were measured various shear rates (0.01 to 20 s-1). Investigations were conducted using a Discovery Hybrid DHR-2 rheometer (TA Instruments) based on a parallel plate setup in rotational mode. The system was configured to maintain a steady temperature of 25°C. The formulations were placed between 40 mm parallel plates separated by a gap of 3000 μm. Origin and TRIOS software from TA instruments were used to process the data.

3D printing of the formulations was performed on a 3D PotterBot Micro 10 printer. Regolith formulations were extruded through the printer using a 6 mm nozzle in a hexagonal structure with a layer thickness of approximately 3 mm and a print rate of 23 s/layer. A total of 17 layers were printed and then the material was allowed to cure overnight in a

fume hood at 25°C. X-ray CT of printed structures was performed using an X-ray microscope (XRM, Zeiss, Inc., Model Xradia 520 Versa). The printed objects were scanned and reconstructed using Scout-and-Scan Reconstruction software and 3D images and videos were constructed using 3DViewer. The X-ray microscope yields image resolution ranging from ca. 0.5 μm voxel size for a 0.5 mm diameter specimen to ca. 55 μm voxel size for a 50 mm diameter specimen. Videos were constructed in 2D and 3D formats.

4.4 COMPUTATIONAL METHODS

Two of the main components of lunar mare simulant are SiO_2 (46.9 wt.%) and Al_2O_3 (12.4 wt.%). As such, α-SiO_2 (quartz) and α-Al_2O_3 (corundum) were used as aggregates in simulations of the crosslinking process. Molecular dynamics simulations were performed to examine the interfacial transition zone (ITZ) formed between the heterogeneous aggregate and oligomeric binders, which determines the chemical and mechanical properties of the transformed matrix. Periodic α-SiO_2 and α-Al_2O_3 structures were sliced along $(01\bar{1}0)$ and (0001) planes to create fully hydroxylated surfaces that ultimately interact with the added oligomers.[32,33] Repeating siloxo and sialate oligomers together with Na atoms were incorporated with the simulation to balance electronic charges (one Na per Al atom).[34] **Figure 19** shows a composite comprising two repeat units of the oligomers and the α-SiO_2(0110) slab corresponds to a Si/Al molar ratio of one. The cell dimensions are 9.83Å×43.03Å×10.81Å; the silica slab and the vacuum space are 24 and 20Å thick along the *y*-coordinate; a more straightforward cell construction and visualization was achieved by transforming the hexagonal α-SiO_2 unit cell to a cubic supercell. Packing of the oligomeric precursors into the simulation cell was executed in the Materials Studio tool "Amorphous cell" (Materials Studio version 8.0). The resulting structures were visualized using the open visualization tool (OVITO) (version 3.7.4).[35]

Table 3 lists the initial number of sialate and siloxo units, and the total number of atoms for each system studied; the Si/Al

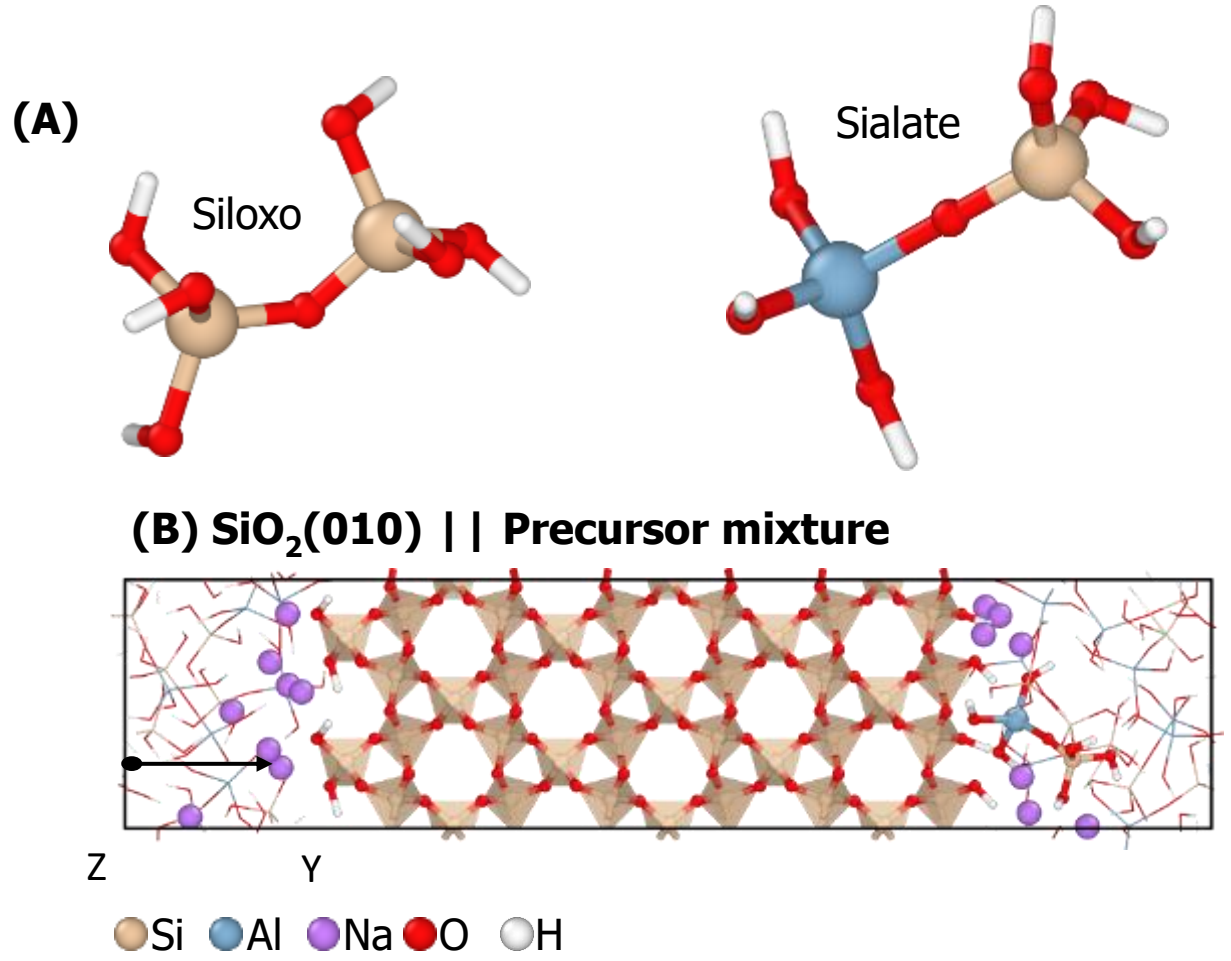

Figure 19. Initial configuration for the system silica/geopolymer precursors. ***(A)*** *Siloxo and sialate oligomers.* ***(B)*** *Side view of the hydroxylated slab α-SiO_2 (01$\bar{1}$0) packed with these oligomer precursors at a molar ratio Si/Al = 1. The semitransparent peach orange polyhedra depict SiO_4 tetrahedra, whereas the rock blue polyhedra correspond to AlO_4 tetrahedra. The left figure bottom provides the atom coloring palette*

molar ratio is the control variable that helps evaluate morphology changes in the ITZ between the aggregate and the added oligomers.[34] The cell dimensions for the system with the α-Al_2O_3 slab are 9.56Å × 8.28Å × 45.00Å. The bulk properties of the oligomeric binders were calculated using cubic cells (14.0Å × 14.5Å × 15.0Å) packed only with oligomeric precursors (same Si/Al ratios as in the equivalent composite systems). **Table 4** summarizes the number of sialate and siloxo units packed in each case.

Si/Al	# Sialate units	# Siloxo units	# Atoms
	α-SiO_2		
No Al	0	17	495
1	15	0	480
2	11	6	491
3	8	8	488
	α-Al_2O_3		
No Al	0	15	481
1	13	0	464
2	9	5	475
3	13	13	473

***Table 3**. Initial configurations for the α-SiO_2 and α-Al_2O_3 composite systems*

Si/Al	# Sialate units	# Siloxo units	# Atoms
∞	0	32	480
1	28	0	448
2	10	19	454
3	15	15	465

***Table 4.** Initial configurations for the bulk geopolymer calculation*

An atomic view of the ITZ zone was developed with the help of hybrid *ab initio* and reactive (HAIR) simulation schemes.[36,37] The HAIR scheme uses in sequence, *ab initio* molecular dynamics (AIMD) and reactive force field (ReaxFF) methods to provide a more accurate calculation than purely classical molecular dynamics methods while extending the achievable simulation time to hundreds of picoseconds (ps). AIMD describes condensation reactions accurately, whereas ReaxFF captures longer-range mass transfer processes.

The Vienna ab initio simulation package (VASP, version 5.4.0) is the engine for AIMD calculations.[38–40] AIMD parameters included the projected-augmented wave (PAW) pseudopotential and the Perdew-Burke-Ernzerhof generalized gradient approximation (PBE-GGA) to handle the exchange-correlation functional.[41,42] Brillouin zone integration was achieved through the Monkhorst-Pack method with a grid mesh set to 1×1×1; partial occupancies for each wave function were handled by setting Gaussian smearing to 0.05 eV.[41,42] The convergence criterion for the self-consistent electronic loop was 10^{-4} eV. The Verlet algorithm integrates Newton's equation of motion; the hydrogen mass was changed to its

tritium isotope to allow for a longer time step equal to 1.2 fs.[43] Finally, AIMD simulation runs with the NVT ensemble, and the Nose-Hoover thermostat (Nose-mass parameter set to 0.5) maintained the temperature around the given setpoint.

The ReaxFF simulation was performed using the large-scale atomic/molecular massively parallel simulation package (LAMMPS, version 3 Mar 2020).[44] ReaxFF parameterization for the composite system with SiO_2 was derived from previous work on water interaction within H-ZSM-5 zeolites.[34,45] Parameterization of the calculations with the Al_2O_3 slab was based on prior work on the oxidation of Al nanoparticles.[46] The time step is 0.125 fs, integration of Newton's equations was performed using the Verlet algorithm, and the Nose-Hoover thermostat set with a damping parameter of 12.5 fs controls the temperature close to the setpoint.

The calculations started with room-temperature equilibration that ran for about eight HAIR cycles to 84 ps. The AIMD step ran 0.5 ps, whereas the ReaxFF simulation lasted 10 ps in each HAIR cycle. The ReaxFF step within the NpT ensemble was executed at a pressure of 1 atm. The annealing procedure was run at 1500K for about 315 ps using the NVT

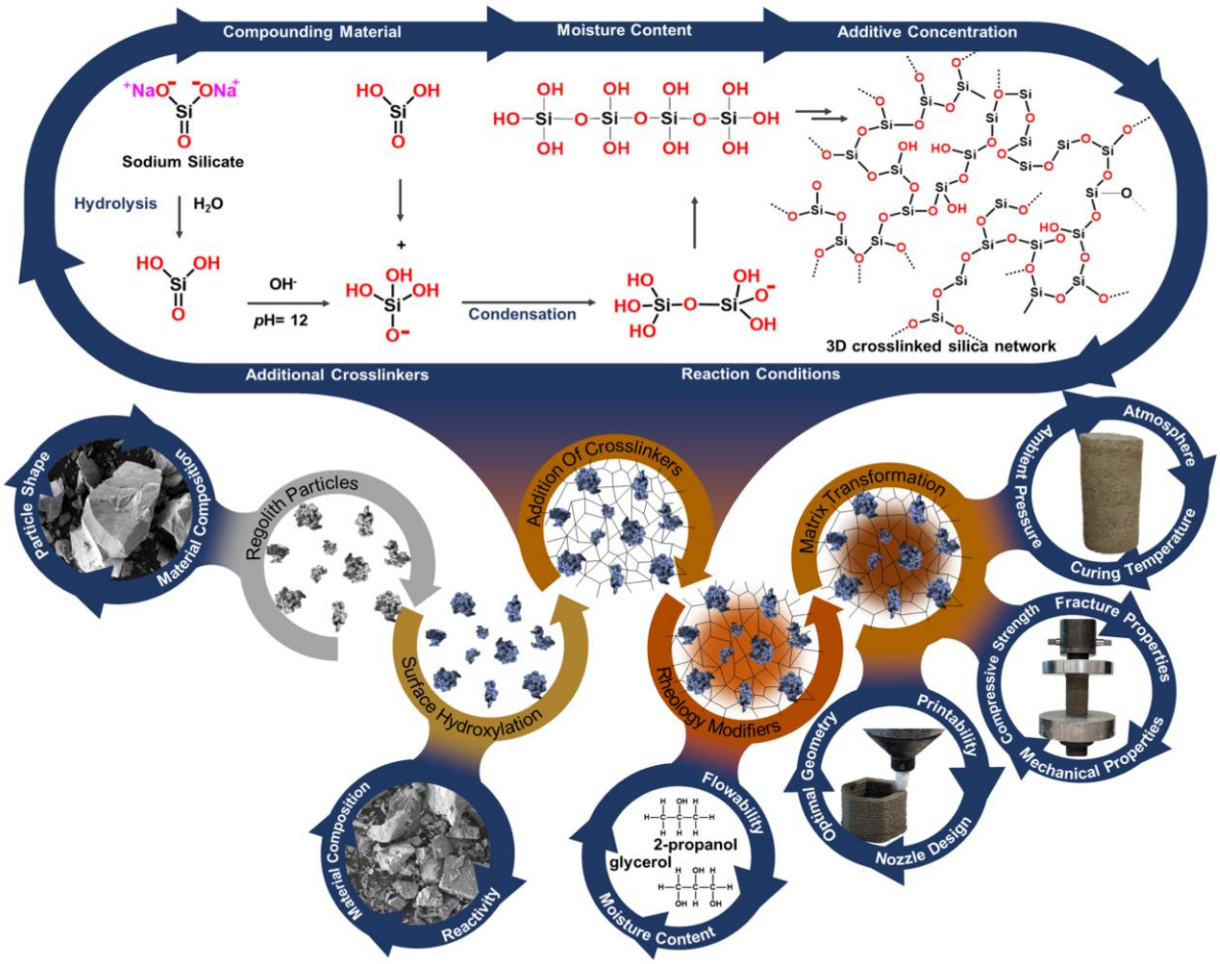

Figure 20. *Schematic illustration of the matrix transformation process*

ensemble in the AIMD and ReaxFF steps of each HAIR cycle. Water molecules formed in condensation reactions were removed after the ReaxFF steps. A linear cool down to 300K at a rate of 5 K/ps was executed, followed by thermal equilibration with the NpT ensemble at 1 atm for about 20 ps. A second equilibration was performed with the AIMD method for about 2 ps with the NVT ensemble. Water molecules were packed into the simulation cells to account for physically adsorbed water before a final thermal equilibration at 300K was performed using an AIMD/ReaxFF/AIMD sequence in the NVT ensemble. The AIMD calculations were run for 2 ps each, whereas the ReaxFF simulations were run for 20 ps. The same simulation protocol was applied to the composite aggregate/binder and bulk oligomer systems.

4.5 Results and Discussion

4.5.1 Bonding Frameworks and Interfacial Reactivity

Unlike Lunar highlands regolith, which has a high alumino-silicate concentration, Mare regolith contains a relatively lower amount of aluminum oxides. As such, this material represents a particularly useful test case for matrix transformation. **Figure 20** schematically illustrates the reaction scheme for surface dissolution, functionalization, and condensation, yielding mineral phases enmeshed in a crosslinked siloxane network incorporating additional multifunctional molecules such as glycerol and hydroxyethyl cellulose.

Figure 21 shows SEM images of the lunar mare regolith before and after modification with sodium silicate and hydroxyethyl cellulose, and additional additives, as described in **Table 2**. In addition to the silicate binder combination,

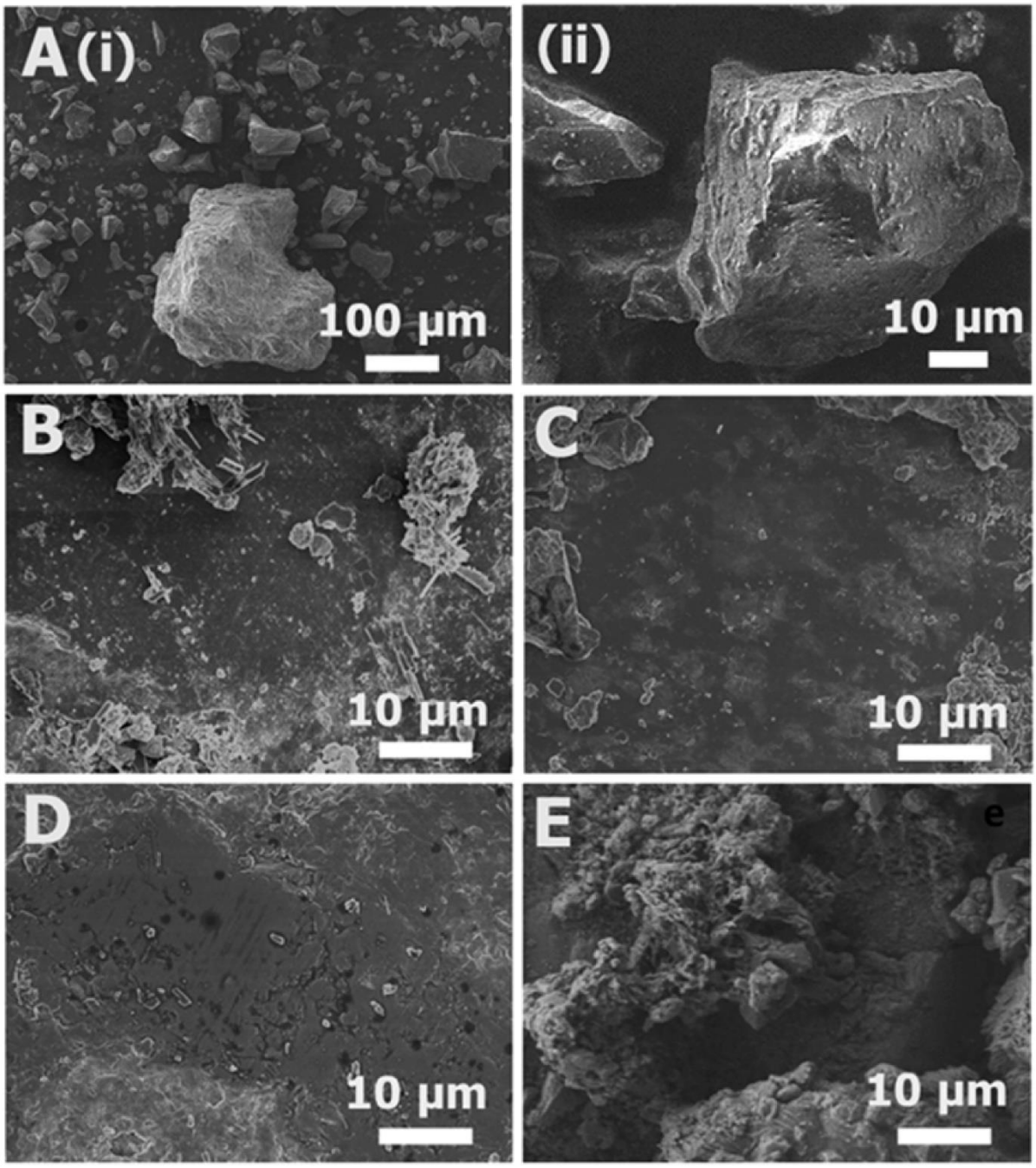

Figure 21. *SEM images of* ***(A)*** *unmodified regolith and consolidated regolith samples* ***(B)*** *F1,* ***(C)*** *F2,* ***(D)*** *F3, and* ***(E)*** *F4 after matrix transformation.*

different formulations have been developed, which include varying concentrations of water, 2-propanol, and glycerol as rheology modifiers and drying aids for using the material as a feedstock for additive manufacturing. A relatively smooth

surface could be achieved with formulations 1, 2, and 3. The increasing solution volume from formulation 1 to formulation 4 increases surface roughness, which is observed as a

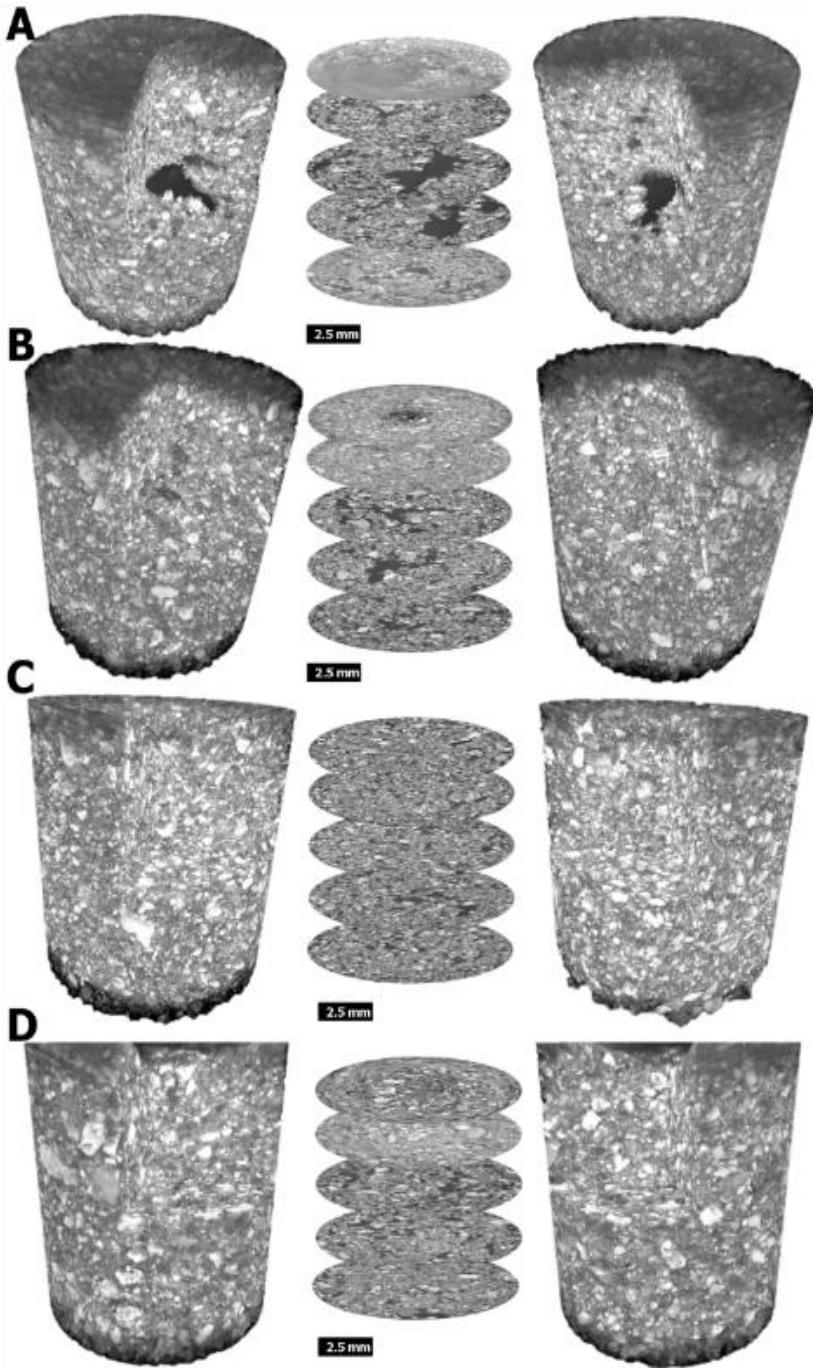

Figure 22. *X-ray CT 2D slices and 3D reconstructions of the 2D slices from two different perspectives for consolidated regolith specimens* ***(A)*** *F1,* ***(B)*** *F2,* ***(C)*** *F3,* ***(D)*** *F4.*

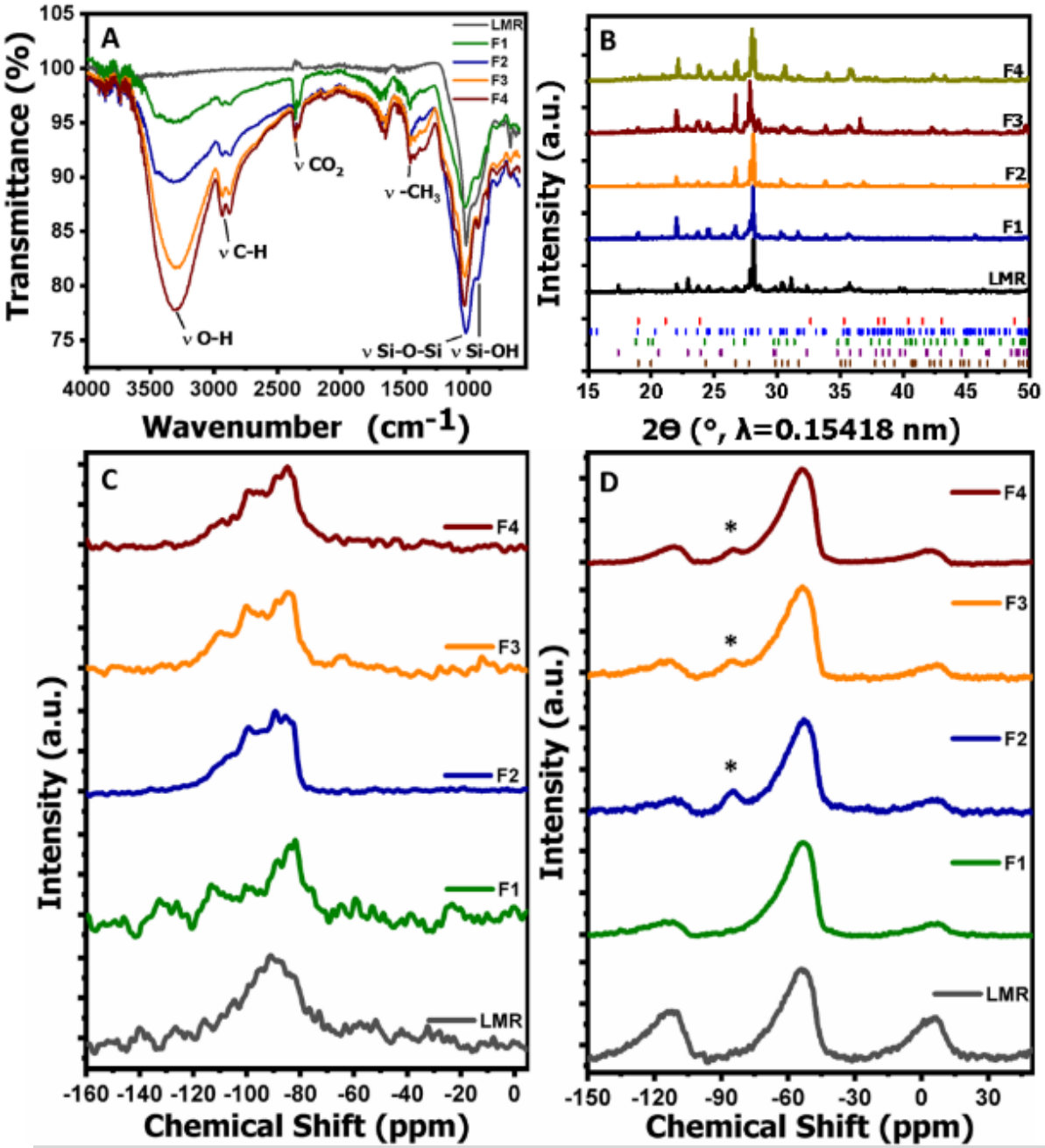

Figure 23. *(A) FTIR spectra acquired for lunar mare regolith prior to any alteration (black), F1 (green), F2 (blue), F3 (orange), and F4 (red).* ***(B)*** *Powder XRD data for lunar mare regolith prior to any alteration (black), F1 (blue), F2 (orange), F3 (red), and F4 (green). Referenced PDF cards are inset along bottom axes and correspond to pyroxene (PDF 86-0748, green), glass-rich basalt (PDF 88-0835, brown), anorthosite (PDF 83-1368, blue), olivine (PDF 84-1402, violet), and ilmenite (PDF75-0519, red).* ***(C)*** *^{29}Si solid-state MAS-NMR spectrum of Mare regolith and F1—F4 and* ***(D)*** *^{27}Al solid-state MAS-NMR spectrum of Mare regolith and F1—F4 with * denoting the appearance of an additional peak.*

higher density of cracks upon solvent evaporation. A higher density of pores and cracks compromises the mechanical

strength of the modified regolith (*vide infra*). Notably, while a higher moisture content results in an increased density of microcracks and pores, reconstructed X-ray tomography results show that the macroscopic porosity is appreciably lower for the latter formulations as a result of the homogeneous dispersion of regolith particles in the binder matrix (**Figure 22**). Indeed, **F1** is characterized by a large cavity at the center of the sample as a result of incomplete mixing of the material resulting from low water content. The limited availability of a liquid medium inhibits the long-range transport of reactants. In contrast, **F2—F4**, show much more homogenous dispersion of regolith particles with a decrease in density with increasing water incorporation (**Figure 22).**

Sample	^{29}Si NMR chemical shifts (ppm)	^{27}Al NMR chemical shifts (ppm)	Possible Q_n^m unit
Mare	-84, -94, -104	-55	Q_0^2, Q_0^3, Q_1^4
1	-81, -83, -88	-55	Q_0^2, Q_2^3, Q_4^4
2	-85, -89, -99	-55, -85	Q_0^2, Q_0^3, Q_2^4
3	-84, -88, -94, -100	-55, -85	$Q_0^2, Q_4^4, Q_0^3, Q_1^4$
4	-84, -88, -93, -95, -99	-55, -85	$Q_0^2, Q_4^4, Q_0^3, Q_1^4$

Table 5. *NMR results for lunar mare regolith and formulations 1-4*

Figure 23 shows FTIR spectroscopy data of the modified formulations. The resulting spectra show characteristics of vibrational modes of a hydroxyethyl cellulose network with -OH, -CH_2-CH_2-, and -CH_3 bands at ca. 3300, 2940/2880, and 1454 cm^{-1}, respectively. Additionally, a series of Si-O-Si and Si-OH vibrational modes are observed at 1115/1023 and 919 cm^{-1}, respectively, attesting to the formation of a siloxane network. **Figure 23B** shows a powder XRD pattern acquired for lunar mare regolith simulant obtained from Exolith Labs where reflections corresponding to pyroxene ($CaZnSi_2O_6$, PDF 86-0748, green), glass-rich basalt $(Mg,Fe,Al,Ti)(Ca,Mg,Fe,Na)(Si,Al)_2O_6$ PDF 88-0835, brown), anorthosite ($Ca_{0.65}Na_{0.32}(Al_{1.62}Si_{2.38}O_8$, PDF 83-1368, blue), olivine (Mg_2SiO_4, PDF 84-1402, violet), and ilmenite ($FeTiO_3$ PDF 75-0519, red) are labeled. Upon matrix transformation with the addition of sodium silicate and hydroxyethyl cellulose, no significant modification in relative ratios of the mineral phases is observed for formulations **F1—F4**. (**Figure 23B**)

Further characterization of the modes of bonding in the crosslinked network comes from solid-state MAS-NMR measurements. ^{29}Si and ^{27}Al solid-state MAS-NMR has been performed for the four formulations and unmodified regolith simulant. The mare regolith simulant comprises a high concentration of paramagnetic constituents, which obscures subtle changes in local chemical environments. The conventional notation of Q_n^m denotes SiO_4 tetrahedral coordinates where *m* refers to the bridging oxygens (*m* = 0 – 4), whereas *n* refers to bonded Al atoms (*n* = 0 – 4)[58]. ^{29}Si solid-state MAS-NMR in Figure 4C indicate pre-existing SiO_4 structures in all samples, as evidenced by the characteristic signatures of Q^2 to Q^4 coordination observed in the spectra (**Figure 23C, D, Table 5**). This is consistent with the presence of silicate moieties, specifically, SiO_4 tetrahedral building blocks. A comparison of the ^{29}Si MAS-NMR spectra of the modified samples **F1—**

F4 with that of the unmodified mare regolith shows a broader range of peaks in the former, mostly in the Q^3 and Q^4 regions (**Table 5**). The broader lineshapes and more complex spectra are indicative of a more diverse range of local chemical environments for Si atoms in the modified samples, which is ascribed to formation of new bonding modes within the interfacial transition zone, such as crosslinked networks binding together the aggregate particles. The changes to ^{29}Si MAS-NMR spectra upon dissolution—reprecipitation and condensation thus attest to the formation of a more complex crosslinked network than present in the unmodified regolith simulant. Further insight into binding modes, specifically the role of Q^4 coordination has been derived from *ab initio* molecular dynamics simulations (*vide infra*). In ^{27}Al solid-state MAS-NMR spectra (**Fig. 23D**), an additional peak can be identified ca. -80 ppm in formulation 2, 3, and 4 (**Figure 23C**, **D**) but not in **F1** and the mare regolith, which attests to surface dissolution, mobilization of Al-species, and subsequent condensation.

Matrix transformation involves the formation of a crosslinked network binding heterogeneous aggregates and binders. As noted above, the ITZ determines the chemical and mechanical properties of the binder.[32,33] However, the ITZ is buried within the matrix and is elusive to being probed by experimental techniques. As such, we have used MD simulations to develop an atomic-scale perspective of the ITZ.[32,35–37] **Figure 24** shows a side view of the silica/binder interface with four different Si/Al ratios. Matrix transformation proceeds through a sequence of condensation reactions.[32] The SiO_2 structure survives the simulated annealing step; instead, partial dehydroxylation of the surface creates Al—O—Si and Si—O—Si bonds that bind together the aggregates. The partial radial distribution function plots for Na—O interactions in **Figure 25** indicate that Na^+-O ionic bonding (2.4Å) is significant within the binder phase and might help strengthen the aggregate/binder interface.

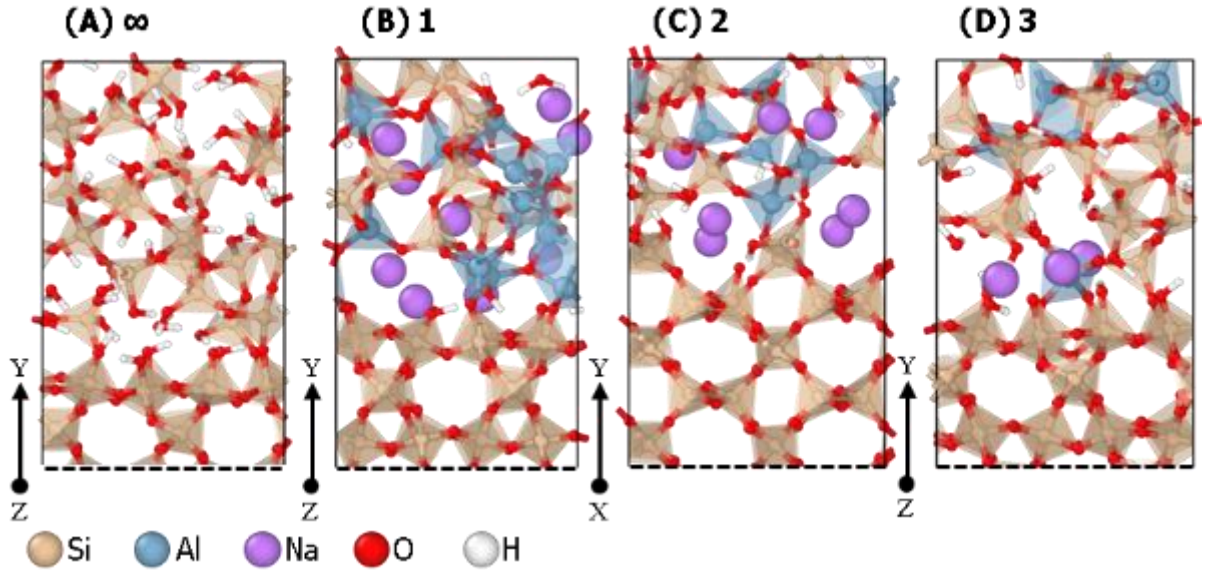

***Figure 24. ITZ zone silica surfaces for multiple Si/Al ratios**. **(A)** ∞, **(B)** 1, **(C)** 2, and **(D)** 3. The semitransparent peach orange polyhedra depict SiO_4 tetrahedra, whereas the rock blue polyhedra correspond to AlO_4 tetrahedra.*

The side view (Si/Al =1) in **Figure 26A** is a reference for the different profiles plotted in **Figure 26B**—**H**. The centered M-shaped pattern in the density profile corresponds to the silica aggregate. The silica/binder interface is characterized by a 4–5Å-thick region with a density ranging from 1.0 to 1.5 g/cm^3 irrespective of the Si/Al ratio. This region corresponds to the ITZ and has a lower density than the bulk density of the

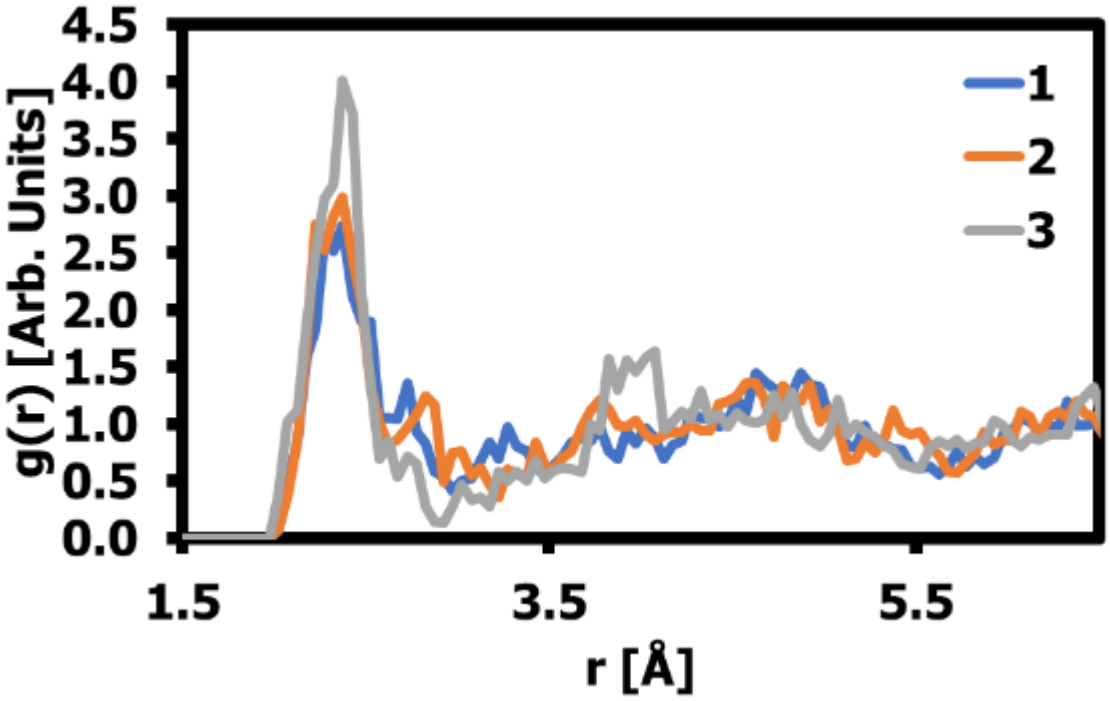

***Figure 25**. Partial radial distribution function profiles for the interactions Na-O for the three Si/Al molar ratios (1, 2, and 3) depicted in **Figure 22** for the silica/binder system.*

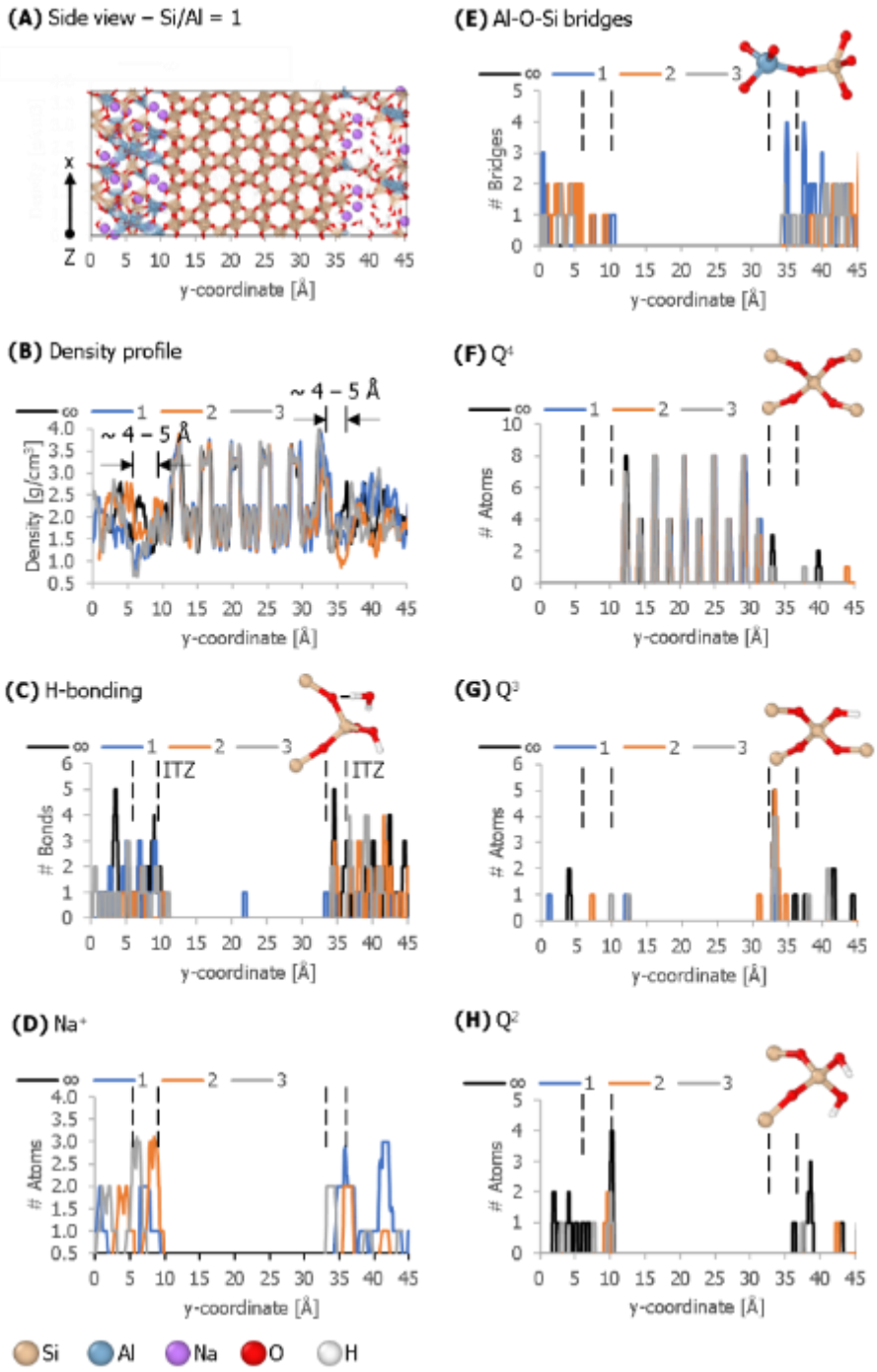

Figure 26. Density profiles for the composite silica/binder system with varying Si/Al ratios = 1, 2, 3. (A) *Side view of an optimized geometry (Si/Al = 1) serving as a reference for the y-projected profiles pictured from* ***(B)*** *to* ***(H).*** *The semitransparent peach orange polyhedra depict SiO_4 tetrahedra, whereas the rock blue polyhedra correspond to AlO_4 tetrahedra.* ***(B)*** *Total density profile.* ***(C)*** *H-bonding profile with a zoomed inset depicting the H—O bonding interaction.* ***(D)*** *Na^+ ion density profile. (E) Density of Al-O-Si bridges with the inset outlining the corresponding bonding interaction.* ***(F)*** *to* ***(H)*** *illusrate Q^4, Q^3, and Q^2 profiles with insets showing the respective structures.*

binder matrix regardless of the Si/Al ratio (**Figure 28**), which suggests a relatively lesser extent of oligomerization in this

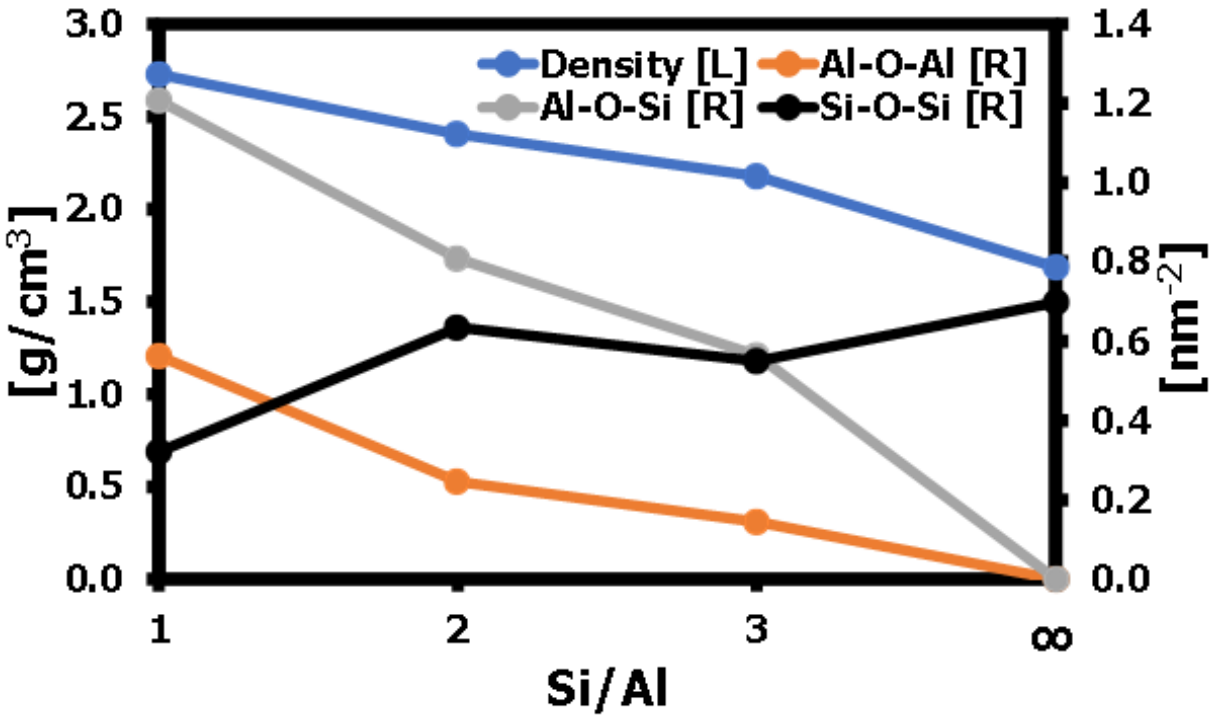

Figure 27. *Density (left vertical axis) and surface cross-linking density (right vertical axis) versus Si/Al ratio in the silica/binder composite.*

region and a preponderance of H-bonding interactions. **Figure 25** also shows the average surface density along the *z*-coordinate of crosslinking sites Al-O-Al, Al-O-Si, and Si-O-Si. The modeled trends in the average surface density of crosslinking sites suggest a higher extent of oligomerization with increasing Al content.

Figures 23C, **D** show an increase in H-bonding interactions and Na^+ concentration close to the ITZ zone. Formation of Al-O-Si bridges (**Figure 26E**) also correlates with the ITZ zone. The ITZ zone is a complex region where multiple interactions contribute to fusing together the aggregate/binder interface. The lowered density (~1.0 g/cm^3) suggests that H-bonding interactions dominate the ITZ zone in the case of a silica aggregate. The number of H-bonding interactions is higher in the transformed matrix without aluminum. In contrast, Na^+ ions and Al-O-Si bridges are more abundant at lower Si/Al ratios. This behavior shows that interfacial interactions are dependent on the Si/Al content (added to the matrix or mobilized through surface dissolution), which in turn governs the mechanical response of the material.

Figures 26F, **H** quantify the degree of polymerization based on the number of shared oxygens bridging the SiO_4 tetrahedra (Q^n, n = 2,3,4). Q^4 refers to a SiO_4 tetrahedron connected to three other silicon species through Si-O-Si bridges and is dominant within the silica phase. Only the phases sans Al (designated as ∞) and the Si/Al = 2 systems show Q^4 bonding within the transformed composite, which indicates a lower polymerization degree than in the aggregate. Instead, Q^3 and Q^2 tetrahedra are dominant within the matrix-transformed composites. The abundance of Q^3 species is greater in proximity

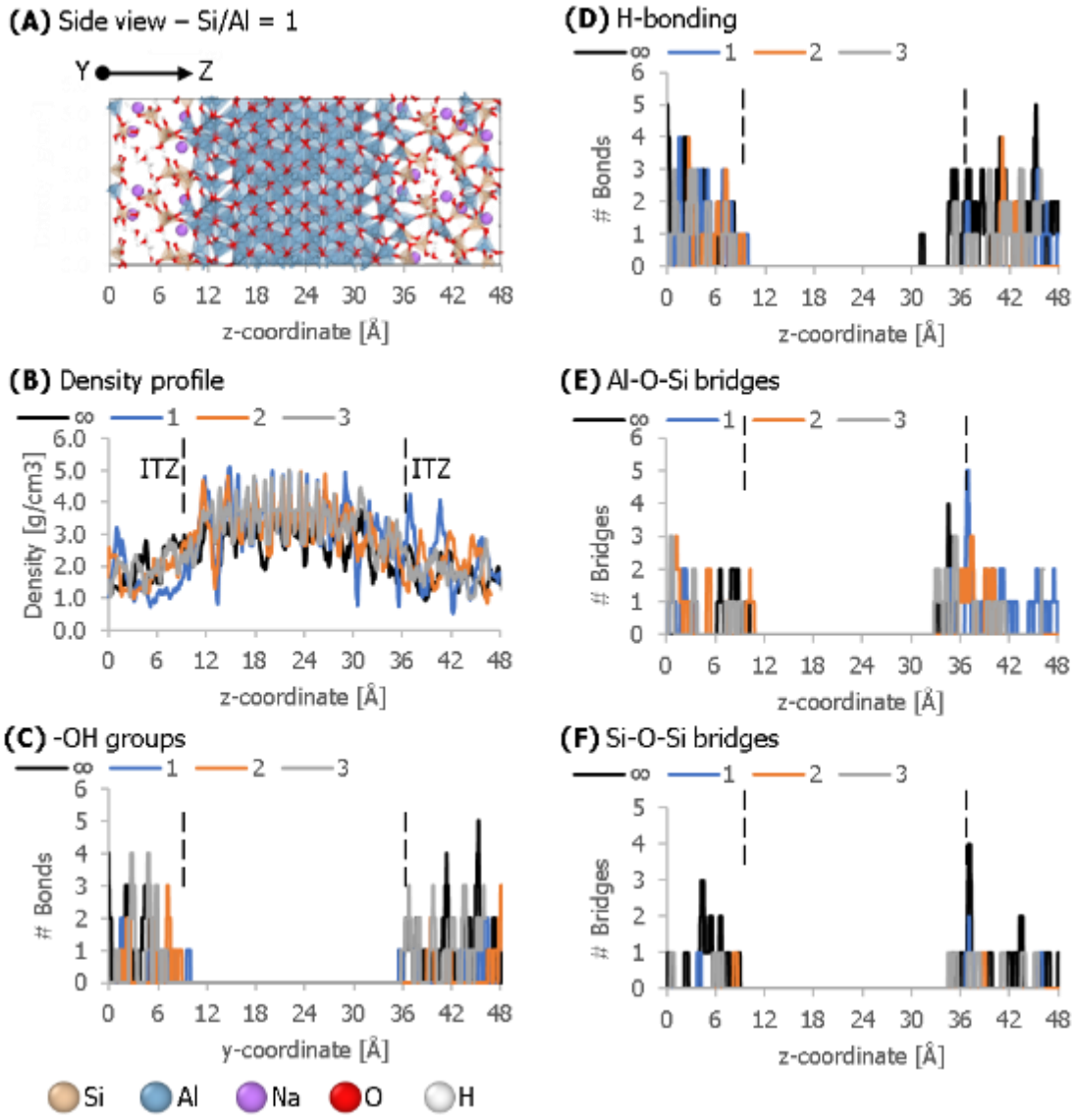

Figure 28. Density profiles for the composite Alumina/binder system with varying Si/Al ratios = 1, 2, 3. (A) *Side view of an optimized geometry (Si/Al = 1) serving as reference for the y-projected profiles pictured from (B) to (F). The semitransparent peach orange polyhedra depict SiO_4 tetrahedra, whereas the rock blue polyhedra correspond to AlO_4 tetrahedra.* ***(B)*** *Total density profile.* ***(C)*** *-OH profile* ***(D)*** *H-bonding* ***(E)*** *Density of Al-O-Si bridges.* ***(F)*** *Density of Si-O-Si bridges.*

of the ITZ zone after the Si/Al ratio increases from 2 to 3, whereas Q^2 species are preponderant in the ITZ when there is no aluminum.

Figure 29 shows multiple *z*-profiles for the system where Al_2O_3 is the aggregate. Again, the centered sawtooth pattern corresponds (**Figure 26A, B**) to the aggregate phase; this region shows an overall density higher compared to the matrix-transformed phase. However, the ITZ zone is less differentiated in this case and there is no clear dip in the density profile at the interface. The -OH and H-bonding profiles in **Figure 28C**, **D** do not show accumulation of these interactions at the aggregate/binder interface but a rather a fairly uniform distribution across the binder phase. **Figure 28E**, **F** show a spike in the number of crosslinking Al-O-Si and Si-O-Si linkages around the ITZ zone. This behavior indicates that Al-O-Si

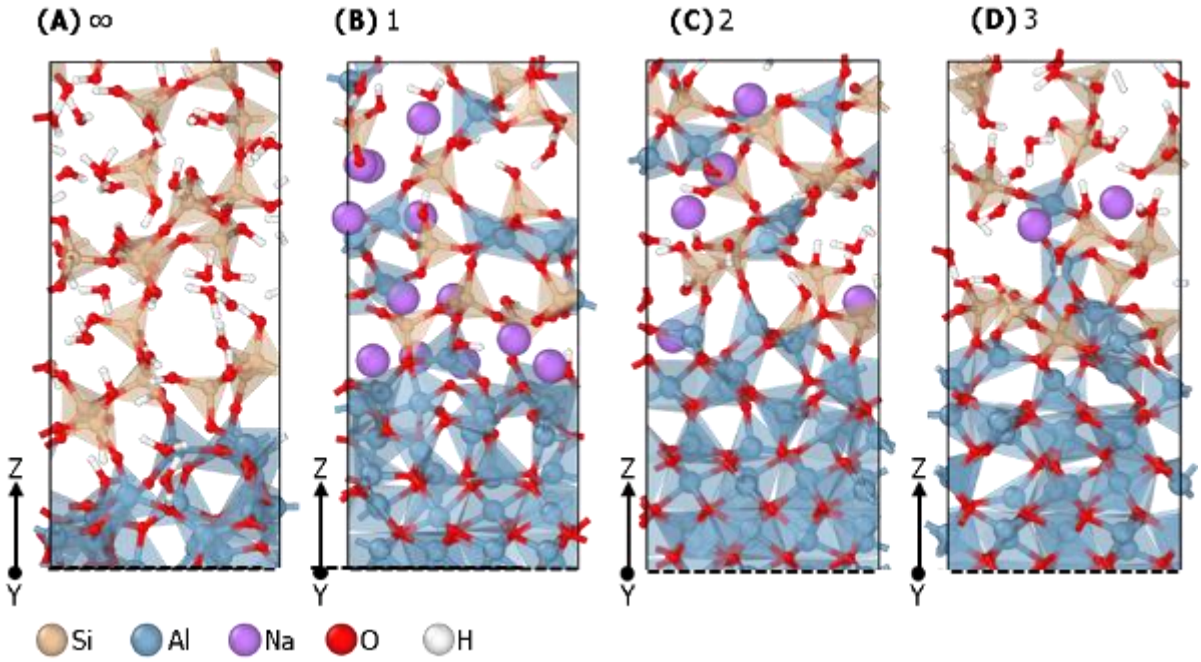

Figure 29. ITZ zone for the alumina/binder system at varying Si/Al ratios. (A) ∞, (B) 1, (C) 2, and (D) 3. The semitransparent peach orange polyhedra depict SiO_4 tetrahedra, whereas the rock blue polyhedra correspond to AlO_4 tetrahedra.

and Si-O-Si dominate over H-bonding interactions at the Al_2O_3/binder interfaces, which indicates a stronger interfacial interaction compared with the silica aggregate. The alumina/binder interfaces in **Figure 29** show no significant H-bonding interactions at the interface and further have a lower abundance of -OH moieties. As such, an increase in Al content through surface dissolution and mobilization strengthens the aggregate/binder interaction.

The formation of a crosslinked network in our MD simulations through condensation reactions, concomitant with the survival of the aggregate SiO_2 and Al_2O_3 structures, are in agreement with the FTIR and XRD patterns shown in **Figures 23A and B**, respectively. The simulations accurately capture the formation of a polycondensed network with surface modification of the SiO_2 and Al_2O_3 particles and formation of Al—O—Si, Si—O—Si, H-bonded, and electrostatic Na—O interactions within the ITZ but without reconstitution of the mineral phases (aggregates). The MD simulations are

consistent with the Q^4 coordination measured by ^{29}Si solid-state MAS-NMR (**Figure 23 C and D**) being derived primarily from SiO_4 moieties within the aggregate, whereas Q^2 and Q^3 coordination clusters are stabilized in the binder matrix and contribute to the greater diversity of local chemical environments observed in the consolidated regolith. Notwithstanding the limited spatial scale of our simulation cells, the denser aggregate/binder interface observed with the Al_2O_3 aggregate and lower H-bonding interactions with higher Al contents in the geopolymer matrix highlight the potential role that Al can play in strengthening the interfacial aggregate/binder interactions, which in turn has implications for improving the mechanical strength and load-bearing properties of the composite material. Indeed, ^{27}Al solid-state MAS-NMR measurements plotted in **Figure 23D** attest to the mobilization of surface Al species and their role in enhancing condensation. Indeed, Al could play a similar role as Ca-ions in the ITZ formed in geopolymer concrete with steel furnace slag (SFS) aggregates, strengthening interfacial bonding, reducing microcracking at the aggregate/binder interface, and improving compressive strength.

4.5.2 Emergent Properties of Consolidated Regolith and Application in Additive Manufacturing

We next examine the properties of consolidated regolith samples F1—F4. Nanoindentation has been performed in order to identify and determine the number of individual phases present and the reduced modulus. Nanoindentation maps have been obtained and statistical analyses have been performed (**Figure 30**). **Figure 30D** plots an example load—displacement curve. From this relationship, the reduced modulus can be determined providing valuable information about the

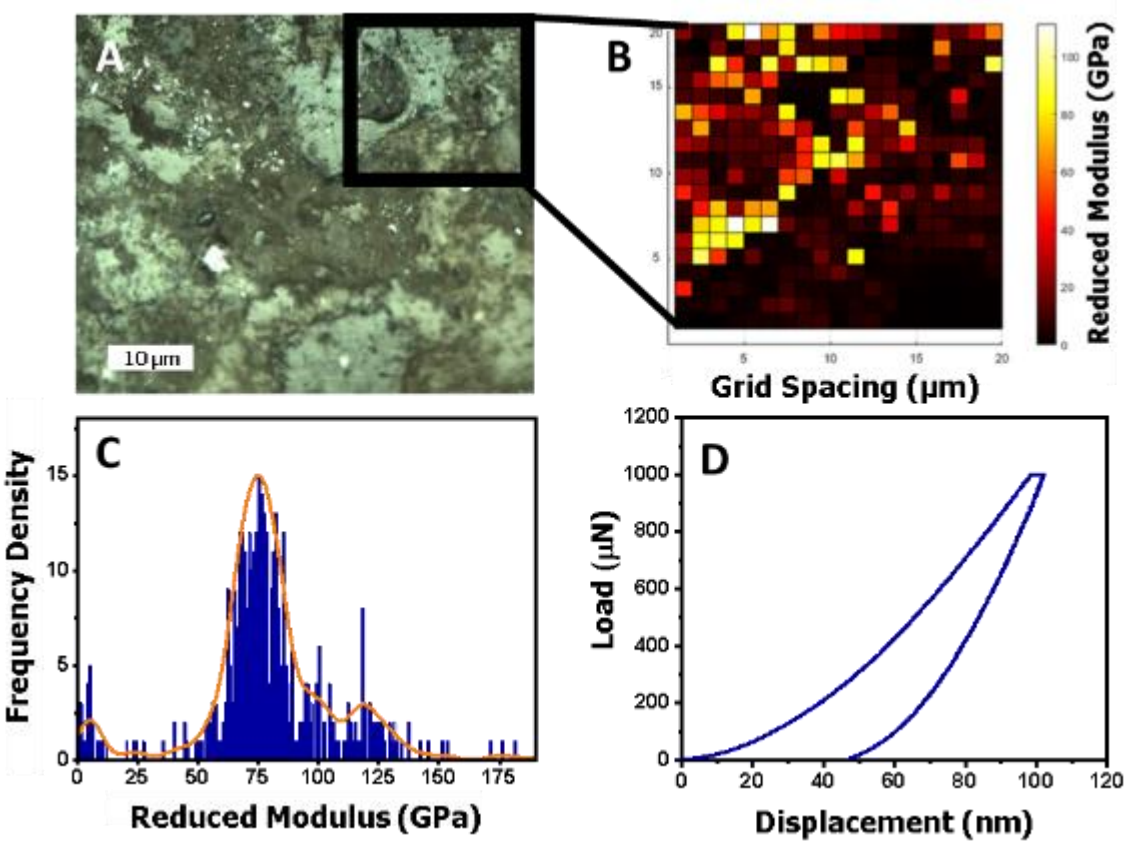

Figure 30. ***(A)*** *Optical micrographs of F1 showing the region where nanoindentation was performed.* ***(B)*** *A representative 20 µm × 20 µm grid with a color map demonstrating differences in the reduced modulus across the surface of F1.* ***(C)*** *Statistical analysis of a series of nanoindentation measurements across a 200 µm grid with a bin size of 1. A distribution curve is included (orange) using a kernel smooth.* ***(D)*** *A representative Load versus Displacement graph for F1.*

distribution of mechanical properties across the sample. Statistical analyses of reduced modulus values mapped across consolidated samples are shown in **Figure 30B** and used to examine the spatial distribution of phase heterogeneities. From the statistical distribution of reduced moduli, two distinct phases can be differentiated (**Figure 30C**). Based on the reduced modulus of these phases, it is postulated that they correspond to individual particles of regolith mineral phases, which have reduced modulus values distributed around ca. 80 GPa, and the hydroxyethyl cellulose/silica matrix with a reduced modulus between ca. 0.55–6.92 GPa. Furthermore, the binder phase exhibits viscoelastic properties characterized by a decrease in reduced modulus upon heating the material (**Table 6**).

Table 6. *Reduced modulus from the statistical distribution of the nanoindentation measurements*

In order to determine the composite mechanical strength of the consolidated regolith formulations, compressive strength measurements have been acquired for **F1—F4**. **Figure 31** shows that that lower moisture content in the samples correlates with higher compressive strength. The presence of high amounts of residual moisture within cylinders results in variances in crosslinking and plastic deformation as the primary mode of failure, whereas formulations with low moisture content

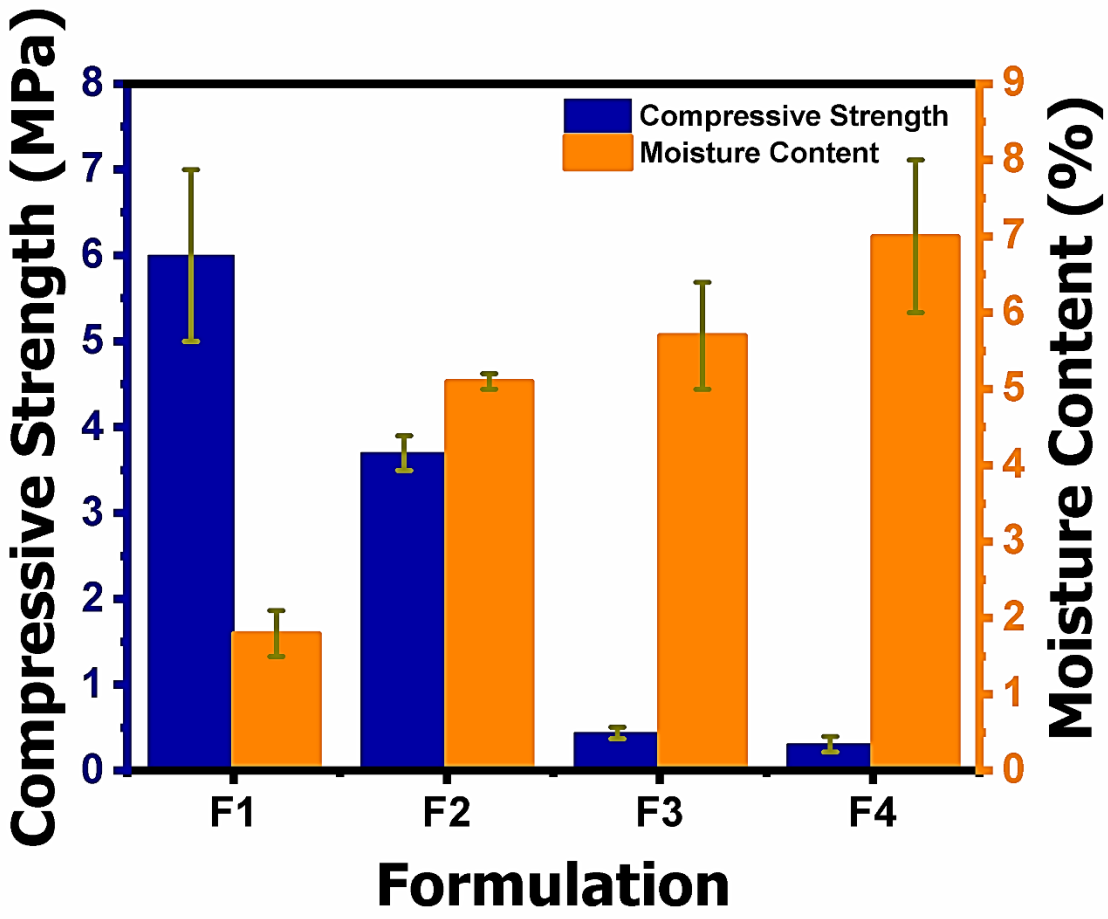

Figure 31. *Compressive strength measurements for the individual regolith formulations (blue). Residual moisture content for the individual formulations (orange).*

exhibit higher strength. While a compressive strength of 6 MPa is relatively high compared to other examples of matrix-transformed materials, the lower water content makes extrusion and adhesion to subsequent layers rather difficult.[12] As such, while a low moisture content yields a higher compressive strength, the resulting formulation would necessitate adoption of a more conventional building method such as the fabrication of tiles or bricks. The F1 formulation presents an optimal combination for fabrication of bricks with further strengthening possible through compaction and cold sintering.[50,51] In contrast, the higher-moisture-content formulations, **F2—F4**, are optimal for efficient extrusion of the material while still maintaining the strength to support subsequent layers.

Rheological properties of matrix transformation formulations are fundamental to understanding their printability. However, as a result of the substantial dispersion in particle size of Lunar mare regolith, ranging from 5 μm to >300 μm, an effective viscosity can only be deduced across a limited range of shear rates (0.01 to 20 s^{-1}). Indeed, the viscosity decreases with increasing shear rates, which is indicative of shear thinning in both formulations used for 3D printing. This shear thinning evidenced in **Figure 32** is indeed pivotal to the printability of the formulations. **F4**, which contains 41.3 vol.% solids, exhibits a lower viscosity and a better print quality (**Fig. 35**) in comparison to **F2**, which contains 51.9 vol.% solids. Although it is desirable to use a homogeneous formulation to enhance printing quality, we have attempted to print

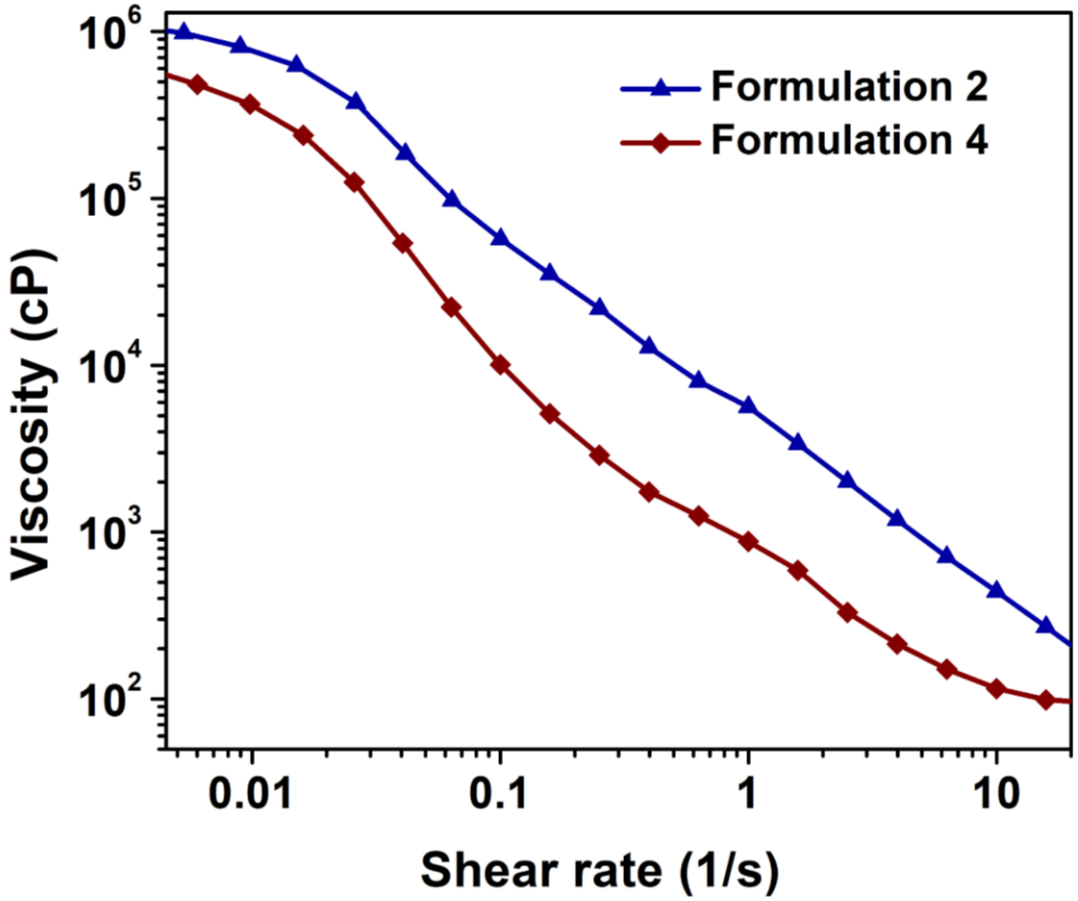

Figure 32. *Viscosity of matrix transformation formulations **F2** and **F4** as a function of shear rate*

regolith without energy intensive grinding. Future work will examine the influence of particle dimensions and geometry on the extrudability, print quality, and ultimate load-bearing properties of the 3D printed objects.

In contrast to hot sintering methods, a matrix-transformation-based approach coupled with extrusion-based printing minimizes the energy budget required while still mitigating the need for sourcing a large amount of Earth-based materials. Water, 2-propanol, and glycerol are added to ensure homogeneous dispersion of the binder and aggregate (the importance

of this is exemplified in **Figure 22**) and have the effect of decreasing the viscosity of the formulation to enable facile extrusion. **Figure 35** shows digital photographs of printed objects. **F4** can be readily extruded through the nozzle of the 3D printer while supporting the weight of subsequent layers. Printing and curing the material inside an enclosed tent will allow recovery and recycling of evaporated liquids, further increasing the efficiency of the matrix transformation process. Increasing the moisture content of **F4** still further led to apparent compression of lower layers indicating that lower moisture content or faster curing are necessary to prevent deformation of the resulting structure. Notably, a print performed under near vacuum conditions is expected to cure much more rapidly. With this in mind, future work will focus on optimization of formulations for near vacuum conditions along with additional investigation into generative design to identify optimal print geometries.

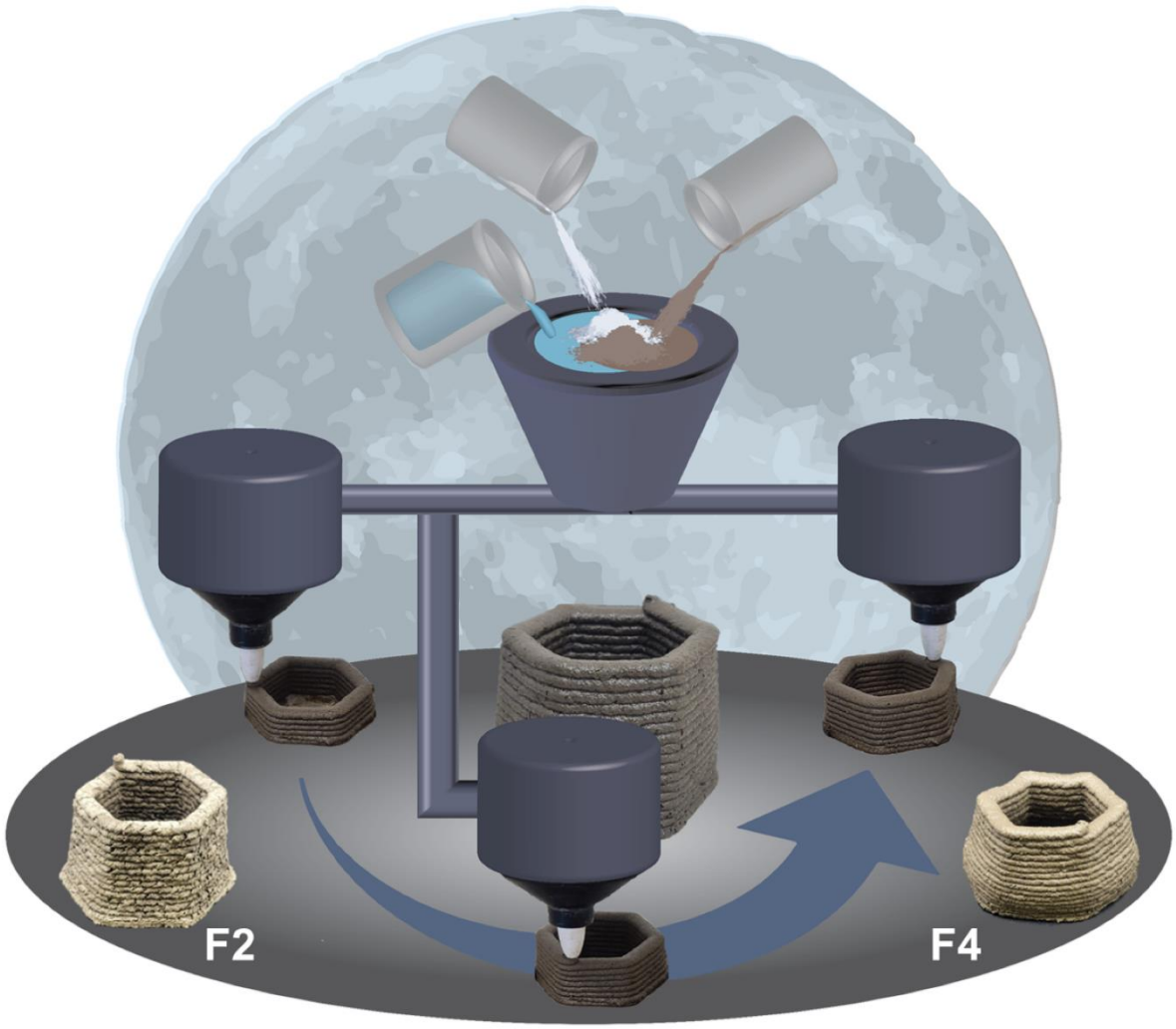

Figure 33. *Illustration of the additive manufacturing process. Digital photographs of example prints of a hexagonal structure using formulation 4 (F4). Cured prints are demonstrated on the left (formulation 2 (F2)) and the right (formulation 4 (F4)).*

4.5.3 EXTRUSION-BASED 3D PRINTING

In contrast to hot sintering methods, a matrix-transformation-based approach coupled with extrusion-based printing diminishes the energy budget required while still mitigating the need for sourcing a large number of Earth-based materials.[54,55] Bottom panel in **Figure 33** shows printing of formulation **F4** under ambient conditions. Water, 2-propanol, and glycerol are added to ensure homogeneous dispersion of the binder and aggregate (the importance of this is exemplified in **Figure 22**) and have the effect of decreasing the viscosity of the formulation to enable facile extrusion. **Figure 33** shows digital photographs of printed objects. As demonstrated in **Figure 33,** the formulation can be readily extruded through the nozzle of the 3D printer while supporting the weight of subsequent layers. Printing and curing the

material inside an enclosed tent will allow recovery and recycling of evaporated liquids, further increasing the efficiency of the matrix transformation process. Increasing the moisture content of **F4** still further led to apparent compression of lower layers indicating that lower moisture content or faster curing are necessary to prevent deformation of the resulting structure. Notably, a print performed under near vacuum conditions is expected to cure much more rapidly. With this in mind, future work will focus on optimization of formulations for near vacuum conditions along with additional investigation into generative design to identify ideal print geometries.

4.6 Conclusion

Key Conclusion 2: A series of surface dissolution and crosslinking modification chemistries have been developed to enable the solidification and consolidation of lunar mare regolith for use as a building material and feedstock for additive manufacturing. Through the addition of sodium silicate and hydroxyethyl cellulose as a binder and ammonium hydroxide as an activator, a matrix transformation process is engendered that binds together regolith particles within a cohesive matrix.

FTIR spectroscopy and MAS NMR measurements attest to formation of crosslinked bonding frameworks including siloxane, -Al-O-Si-, and hydroxyethyl cellulose crosslinked frameworks. Molecular dynamics simulations suggest formation of a low-density region ITZ region between the aggregate and binders where hydrogen bonding and electrostatic interactions are preponderant over siloxane linkages. Surface dissolution and mobilization of Al species further facilitates the formation of -Al-O-Si- bridging moieties. Consolidation is facilitated by the solvent-mediated necking of adjacent particles as capillary pressure draws the particles together. The overall extent of oligomerization is lesser at aggregate/binder interfaces as compared to the crosslinked matrix. Water, 2-propanol and glycerol are used to aid in the dispersion of binder species and serve as rheology modifiers to enable extrusion of the modified regolith through a nozzle. Low-moisture-content formulations are challenging to print but can achieve relatively higher compressive strength values, suggesting potential application in fabrication of tiles and bricks. In contrast, higher-moisture-content formulations serve as viable additive manufacturing feedstock and yield high-resolution printed objects. XCT reconstructions suggest that lower-moisture-content samples evidence greater heterogeneity traceable to uneven dispersion of the binder, whereas higher-moisture-content formulations show more homogeneous dispersion of aggregate and binder but show deleterious emergent porosity resulting from solvent evaporation. Future work will focus on optimization of printing formulations for high vacuum environments and exploration of generative design to identify optimal 3D load-bearing geometries.

We also aim to explore the many options which has been proven to increase the mechanical strength of the modified regolith, starting with K, and Na.[56] Both of the ions can substitute Si sites through alkaline bases or specific precursors, offering a wide range of selections for trials. Using the extensive simulation toolset developed in this effort as guidance, we will further expand our vision to identify a specific ratio of the different cations that yield optimal compressive strength. In the shorter term, we plan to test the modification process under lunar surface conditions and observe the impacts of extreme environments on the structural integrity of the 3D printed strucures. Simulating ambient air and regulating specific temperature, the modification process can be tested to its limits and should reflect valuable information about the physical

properties of the modified process.[57–60] We further aspire to modify regolith to access distinct physical properties: porosity for controlling heat and moisture dispersion,[61] and extrudability for 3D printing.[62]

In general, our the regolith consolidation chemistry elaborates upon our distinctive geopolymerization concepts deployed successfully at scale in the sub-Arctic to build all-weather roads but has been tuned to match specific Lunar Mare regolith compositions. Our initial laboratory scale results show bricks that are able to withstand temperatures ranging from -196 to 1450°C and substantial impact as indicated in **Figure 34**. The potential for building infrastructure from such consolidated regolith is further illustrated in the bottom pannel of **Figure 34** which shows that the bricks are able to withstand the weight of a 5000 lb SUV, which can be driven over them repeatedly without any discernible damage.

4.7 Limitations of the Study

One of the primary limitations of this study was the implementation of this technique under ambient conditions. Variations in the temperature and pressure of the lunar environment could possibly modify the experimental results. Reducing the

Figure 34. "Taming Regolith": *Bricks of Lunar Mare regolith constructed using silicate condensation chemistry. The bricks survive repeated impact on a stone surface as well as large extremes of temperature ranging from -196 to 1450°C and the bottom panel shows that the* ***bricks can sustain >5000lbs of weight.***

pressure under which the formulations are cured would result in much more rapid curing as the liquid phase evaporates. While this has not been directly studied in this work, it is postulated that the rapid curing would lead to a less dense albeit stronger print as suggested by the reverse correlation between residual moisture content and compressive strength. Furthermore, one of the key challenges of lunar construction is the need to transport earth-based additives which can be incorporated with lunar-sourced materials for construction. While matrix transformation limits the number of earth-based additives that are used, it has not been demonstrated that these incorporated additives can be recycled for repeated construction on the lunar surface. As sketched in **Figure 4**, a critical innovative feature of RAMS is the release of precursors that can form surface-bound silicate and aluminosilicate linkages between regolith particles and thus bind the materials within low-porosity load-bearing slabs. Such reactions will be initiated within the subsurface by positioning microcapsules that are activated by the heat of surface thermite reactions. In thia report, we have described the reaction chemistry initially investigated for regolith consolidation.

Silicate condensation yields robust and thermally resilient tiles but is prone to surface cracks. Additional crosslinking modes that yield some degree of elasticity is needed to avoid entirely brittle consolidation processes. This has been addressed through incorporation of oligomeric or polymeric crosslinkers. The incorporation of crosslinkers yields a means of elastic deformation and mitigates crack formation.

The surface cracking visible in these bricks has been further reduced by developing a solidification approach using 2-propanol and glycerol. **Figure 34** shows some of our current best-in-class formulations. The formulations have been developed based on extensive Raman and Fourier transform infrared spectroscopy studies in conjunction with microstructure evaluation by scanning electron microscopy, compressive testing, and nanoindentation studies. Multivariate experimental matrices have been navigated using a "design of experiments" strategy.

5. MICROCAPSULE DELIVERY SYSTEMS

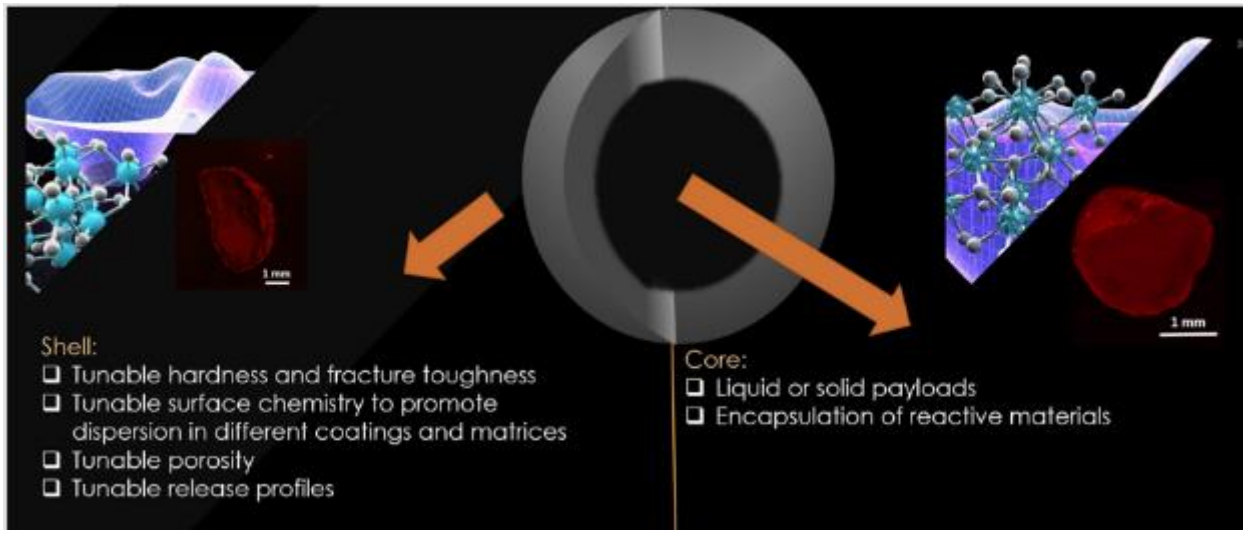

Figure 35. *Sketch of microcapsule delivery systems listing desired properties for core and shell. Insets show confocal light microscopy images of microcapsules.*

A distinctive aspect of RAMS is the design of microcapsule delivery systems (**Figure 35**) to ensure the strategic positioning of precursors for the transformation of regolith at different depths from the surface. This is critical to ensure deterministic propagation of reaction fronts to form subsurface consolidated slabs and surface metal sheets, anchors, and skins. Microcapsules release their precursors in response to activation from impact or heat. The former is desirable for thermite precursors that activate upon impact on Fe/Ti-containing minerals through strongly exothermic thermite reactions. The latter is sought to be used to release organosilane and oligomeric crosslinker precursors deployed in the subsurface to initiate and propagate matrix transformation reactions.

5.1. PREPARATION OF MICROCAPSULES

Microencapsulation is a well-established method of covering active compounds with protective coatings that creates microcapsules ranging in size from 0.2 to 5000m. The inside payload can be a solid, liquid, or gas, while the external shell is typically a solid that is cross-linked upon application. The payload is released in reaction to mechanical stress that causes shell rupture or a stimulus that causes shell depolymerization or breakdown.

Solidification through the microencapsulation approach transforms the liquid geopolymerization precursors into solid-phase microcapsules, pucks, pellets, or bricks, which greatly enhances their safety during delivery/transportation. We have designed single-nozzle and dual-nozzle approaches to prepare a diverse range of microcapsules with shell materials spanning the range from asphaltenes to various polymers. Sodium alginate was used in the making of oil-core microcapsules for corroborating impact testing results from computational modeling.

An automated jetting system equipped with a concentric nozzle facilitates the preparation of the core-shell microcapsules.

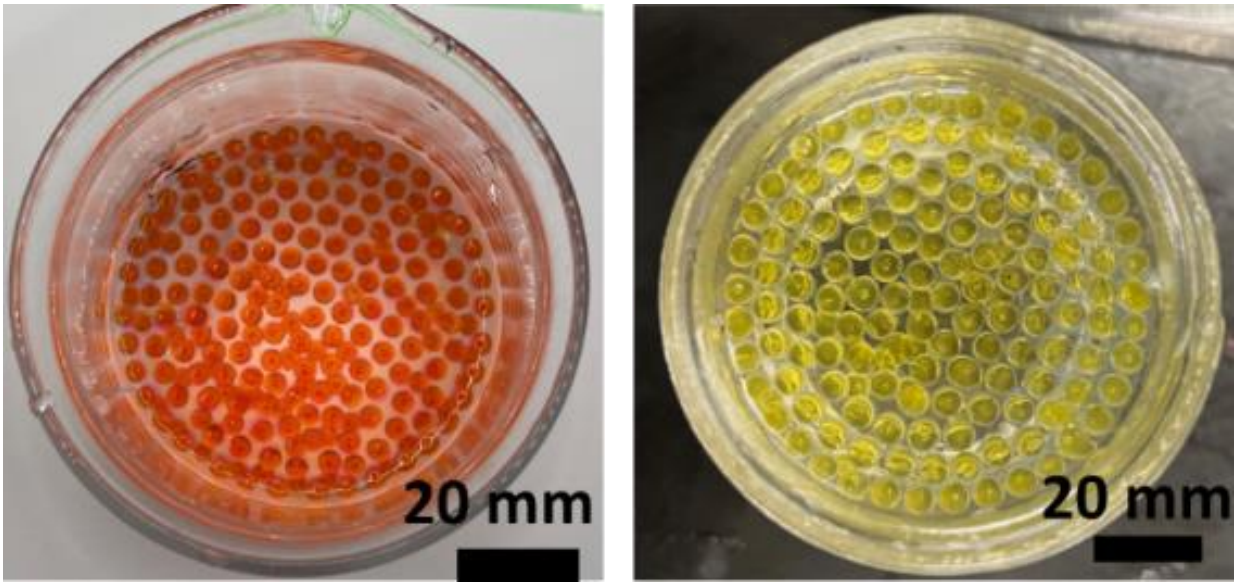

Figure 36. *Microcapsules containing about 65% core material prepared for model studies.* ***(A)****Vegetable oil dyed with olyisobutylene-1000 bound para- methyl red and encapsulated within 2 wt.% sodium alginate shells. Average diameter= 4.1 ± 0.21 mm* ***(B)*** *Castor oil dyed with olyisobutylene-1000 bound para- methyl red and encapsulated within 2 wt.% sodium alginate shells. Average Diameter= 4.7 ± 0.40 mm.*

Figure 36 shows a digital picture of microcapsules prepared for model studies. The inner flow stream of concentric nozzles comprises vegetable or castor oil, whereas the outer flow stream comprises a dispersion of 2 wt.% sodium alginate. The diameter of concentric nozzles is selected as 750 and 1000 μm for the inner and outer nozzle, respectively. The nozzle diameters affect the resulting capsules' size and shell thickness. The flow stream is mechanically disrupted with an attenuator to enable the formation of uniform microcapsules. Mechanical vibration is introduced to break the concentric flow. The vibration frequency, which also affects the size of the capsule, is set to 500 Hz. The microcapsules are collected in a water bath containing 2 wt % surfactant (poly(ethylene

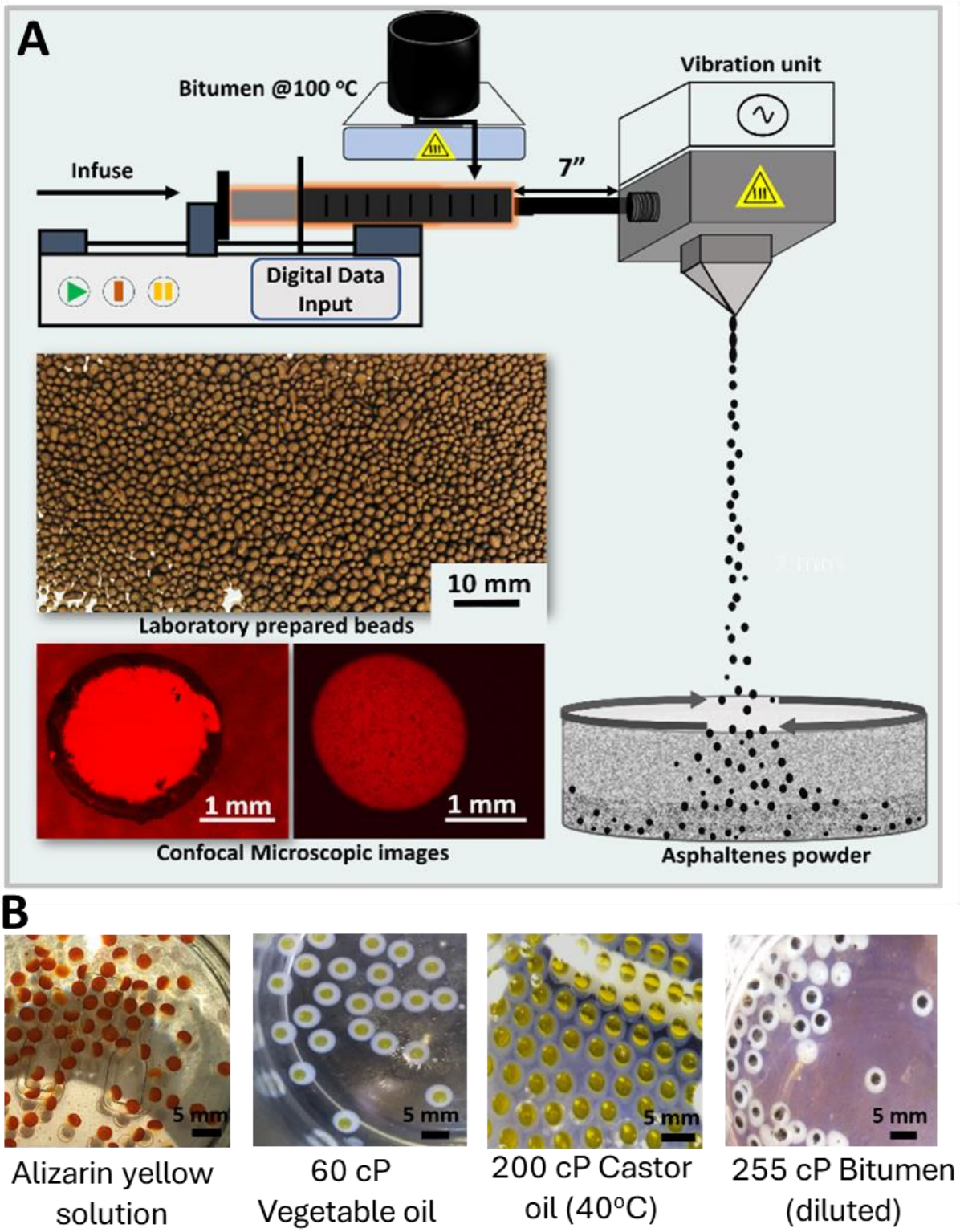

Figure 37. *(A) Powder coating for asphaltene-encapsulated bitumen.* ***(B)*** *various oils and dyes encapsulated within 2 wt.% alginate shells*

oxide)–poly(propylene oxide)–poly(ethylene oxide)) (industrially known as pluronic F127) and 2 wt.% aqueous solution of $CaCl_2$. The shells containing sodium alginate are crosslinked upon contact with the $CaCl_2$ solution. 2 wt.% pluronic F127 solution during collection reduces the surface tension of water and prevents the rupture of the capsules upon impact.

The stirring rate during collection is set to 50 rpm. After the setup was established, the core solution was flown at 10 mL/min and the shell solution at 14 mL/min. Since crowding leads to particle agglomeration, the microcapsule collection was terminated at the first sign of crowding. The microcapsules were then left and stored in the same container to cure at room temperature. **Figure 37** shows a schematic of the synthetic apparatus we have designed alongside confocal light microscopy images of microcapsules. **Figure 37B** also shows shell materials ranging from asphaltenes to polymers developed in previous work by our group that is informing the design of microcapsule delivery systems for regolith modification.

The model system studies will help us further the encapsulation of RAMS material with various polymer shell materials surrounding a core composed of water, hydroxyethyl cellulose, and sodium silicate. Future work on microencapsulation will involve more rigorous testing of polymers for use in microencapsulation. Polymerizations that occur without reacting with core materials will be essential for the success of this project. Polyurethane shell material preparation and encapsulation effectiveness are under active investigation. The effects of varying the solvent concerning the core material will be examined more closely, and polymerization agents should be tested for reaction with the core material before more extensive microencapsulation experiments are conducted.

5.2. Simulations of Microcapsule Delivery

The delivery of chemical precursors via injection of microcapsules is a crucial capability required for RAMS processes. We must therefore acquire a complete understanding of the interactions between a high-velocity microcapsule and Lunar regolith particle beds. The research aims to model a delivery system for a visco-elastic material in a lunar environment. The capsule and material within will be shot out through a projectile system into a bed of lunar regolith. Precisely, we have examined how granular properties—particle size distribution, frictional and cohesive forces, etc.—and the microcapsule properties—size, density, velocity—influence momentum transfer, kinetic energy dissipation, penetration depth, impact crater formation and mixing, as well as microcapsule deformation and fracture. We are engaged in simulations of these phenomena to determine how these properties are likely to influence the effectiveness of chemical delivery to the soil.

The discrete element method (DEM) models the interactions of discrete particles, usually spheres, according to Newton's laws and any interparticle forces that may be prescribed. It is an explicit dynamic simulation, which tracks each particle's position and momentum vectors in time, and is, therefore, an attractive modeling strategy for simulating the behavior of granular media. After all forces and interactions have been calculated in each iteration, the simulation progresses the location of all particles by the time-step provided in the software.

The DEM simulations are being performed using LIGGGHTS. LIGGGHTS stands for LAMMPS Improved for General Granular and Granular Heat Transfer Simulations. This open-source software developed at Sandia National Labs is available on GitHub, https://github.com/CFDEMproject/LIGGGHTS-PUBLIC. The LIGGGHTS DEM simulations are being performed on a laptop using 4 processors. An input script for the software sets the particle and mesh properties, how particles are inserted, the time step magnitude, the gravity vector, and any other forces (cohesion, friction, etc.).

Current literature for impact craters studies the effect of the speed of the incoming particle and the angle of impact. However, most studies only use mono-sized particles for the bed of particles and do not include cohesive force between particles, which are especially likely to be present in Lunar soils. Both particle size distribution and cohesive forces are included in our simulations. Ultimately, we want to simulate realistic Lunar soils with a realistic size distribution. However, for simulating impact, this would require at least 10^9 particles. For now, our simulation contains more than 150,000 spherical particles. The particle bed size distribution in the simulation was chosen out of the sizes determined by the particle size analyzer. The particle sizes used in the simulation range from 80-400 μm. The microcapsule projectile has a radius of $1/10^{th}$ the size of the container. The particles are contained in a vessel roughly 20 cm in diameter and 25 cm high. The goal for particle insertion would be to completely fill the container with particles and assess the displacement of the surface particles.

The equation that is utilized in the computations of the forces of the particles is given by:

$$F = (kn\delta nij - \gamma nvnij) + (kt\delta tij - \delta tvtij)\ldots(3)$$

where δ_n is the overlap distance of two particles, k_n is the elastic constant for normal contact, k_t is the elastic contact for tangential contact, γ_n is the viscoelastic damping constant for normal contact, γ_t is the viscoelastic damping constant for tangential contact, and $delta_t$ is the tangential displacement vector between two spherical particles. Cohesive behavior between particles is governed by the equation $F = kA$ where k is the cohedive energy density and A is the particle contact area given by the equation

$$\frac{\frac{\pi}{4}(D - R_i - R_j)(D + R_i - R_j)(D - R_i + R_j)(D + R_i + R_j)}{(D^2)} \ldots(4)$$

where D is the distance between the centers of particles i and j, and R_i is the radius of particle i.

Paraview is being used to visualize the simulations. LIGGGHTS outputs .vtk data files that can be read directly into Paraview. Paraview offers a wide variety of options for color mapping to visualize different physical properties, such as velocity distribution and particle diameter.

The particle size distribution for the simulation was based on the sizes determined by the particle size analyzer, with the smallest particle size being slightly larger than 1 micrometer. The simulation, however, used particles with a size range of 1–1167 micrometers and did not include particles smaller than 1 micrometer. Larger particles were chosen to shorten the LIGGGHTs software's computing time. Several target particle beds were built throughout the investigation, with the first bed being a cylinder mesh with three different sized particles. The projectile shell's geometry led to changes in particle

bed size, with an initial bed of 53 particle sizes proving to be too computationally expensive. In order to combat this, the number of particle sizes was decreased, and the diameter of the cylindrical mesh was raised in order to lower the container's wall effect. However, the wall effect continued despite the addition of buffer particles to lessen its effects.

Our most recent simulations consist of 923,000 particles with 300,000 steps, each time step being 0.1 ms. We have indications that the time step must be even smaller at specific points within the system to ensure numerical stability. For example, when the incoming projectile collides with the particle bed, soil particles at the bottom of the container can erroneously pass through the bottom if the time step is too large. The particles will pass through the bottom of a container because the particles move too far with the current time step.

The characteristics of the spread of the material that are tracked in this study are the distance that the particles traveled from an established center point. Another aspect to track is the penetration depth versus width of the particle spread. Penetrating a bed of particles is more complex than spreading along a surface; if the penetration is larger than the spread, one can assume that the projectile transferred enough energy to allow the particles to infiltrate the bed of particles. However, if the particles spread along the surface, then the particles will clump and stagnate. The particles of the probing material are twice as small as the smallest particles in the target particle bed, allowing particles to fit and flow through vacancies in the particle bed. **Figure 38** shows different scenarios developed in response to the projectile impact. **Figure 38A** shows the penetration impact of a 110-mm diameter projectile within a granular bed. While **Figure 38B-C** illustrates simulation results where the projectile does not have enough momentum to penetrate the bed of particles. The capsules either form craters from the resulting impact or the impact cause the projectile to reflect with or without rupture.

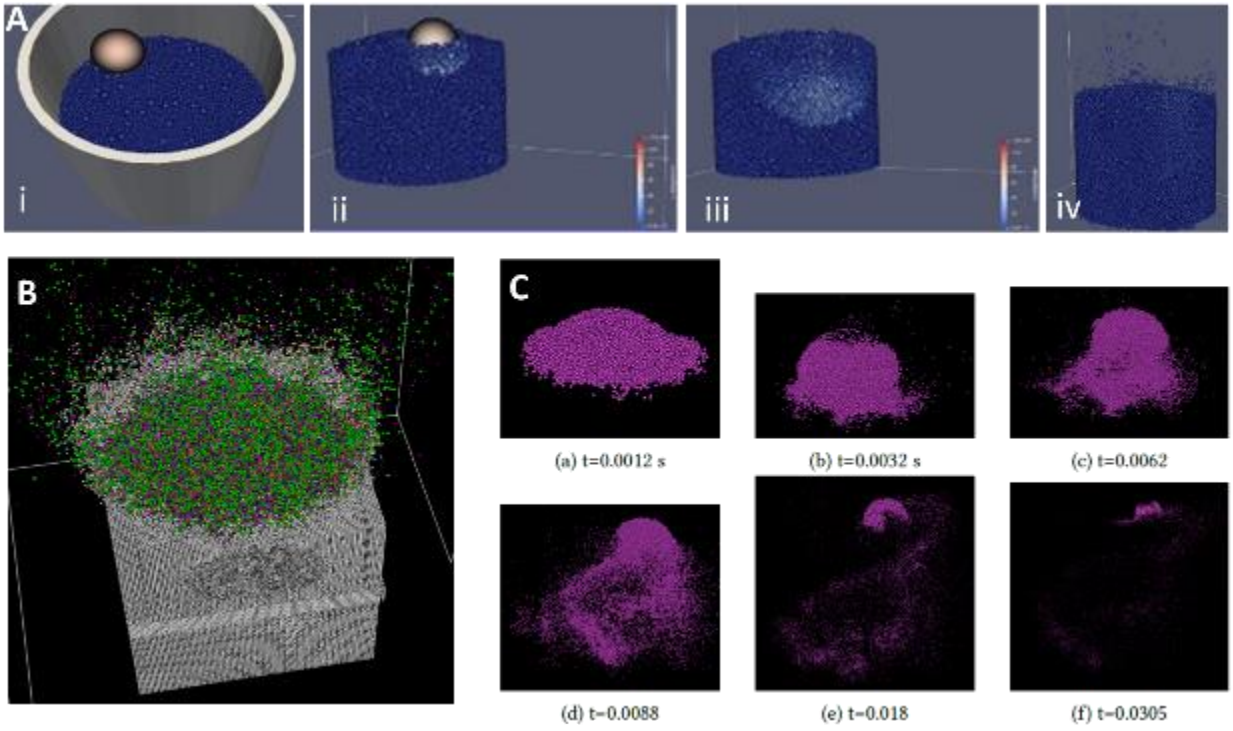

Figure 38. *Impact of projectiles:* ***(A)*** *Penetration of a 110-mm diameter projectile within a granular bed. (i) the moment of contact with the particle bed; (ii) 15 ms after first contact; (iii) 35 ms after first contact; and (iv) 80 ms after first contact. Particle speed is color coded on a scale from 0 m* s^{-1} *(dark blue) to 120 m* s^{-1} *(bright red).* ***(B)*** *The bed of particles after interacting with the rebounding projectile.* ***(C)*** *Impact of the granular bed causes the projectile to reflect. The refection does not allow the allow the inside probes to permeate the bed well.*

5.2.1 CAPSULE DESIGN

Figure 39 shows four capsule geometries at different time steps to illustrate the rupture of the capsule upon impact. The geometry of the capsule has gone through four design changes for this project. At the beginning of this project, the idea was to model a spherical impacting container/capsule that can deliver some material farther into a bed of particles. The LIGGGHTS command that creates a multi-sphere was then explored to create a multi-sphere in the shape of a sphere. A complete spherical multi-sphere was created, as seen in **Figure 39A**, then launched toward a wall and a bed of particles to explore the outcome of this geometry. Once the threshold value was met for one of the atoms in the capsule, all atoms were released from locked spatial constraints. This led to the geometry of the impact particle completely losing its shape during impact and seemed to diminish the delivery of the visco-elastic material. The second shape of the multi-sphere capsule, as seen in **Figure 39B**, duplicates a sphere split at the hemisphere. These two multi-spheres overlapped, so they stuck to each other until one broke during the simulation. Comparisons of three different projectile actions were compared. The apparent differences between the simulations were that in each simulation, the projectile acted differently; the particle did not break, the particle broke as a brittle object, and the bottom hemisphere of the projectile broke while the top

hemisphere maintained its geometry. The geometry from **Figure 39B** allowed the visco-elastic material to pass through holes and did not resemble a well-shaped sphere. Because of these problems, a third geometry was constructed; this new geometry can be seen in **Figure 39C**. **Figure 41C** capsule contained mechanics in the geometry to keep the pieces together and better resemble a sphere. The capsule is made out of nine pieces. Eight of the nine pieces are one-quarter of a sphere's surface. Both halves were divided into four equal sections, rotated, and aligned so that the overall geometry was still a complete sphere. The geometry of the bottom 4 pieces is slightly different than the top 4 pieces; one of the top pieces can be seen in **Figure 39C**. One last piece is added to the geometry, a belt that encompasses the equator of the shell, which constrains the shell. The belt's purpose is to support the structure of the shell when it collides with the bed of particles resisting the shell's urge to compress. This geometry was used to emulate a continuous event rather than a discrete event.

5.2.2 Analysis of Impact (work in progress)

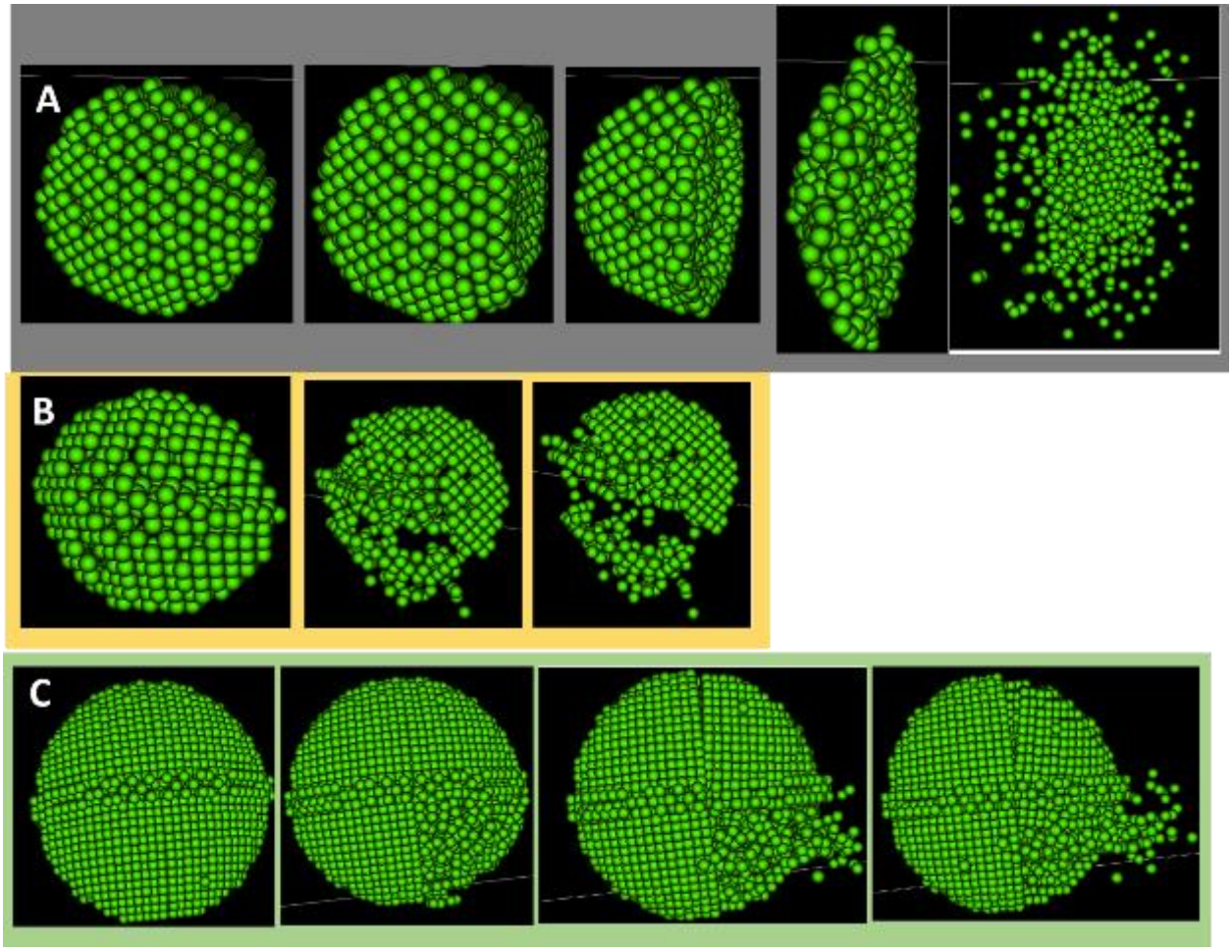

Figure 39. Capsule geometries at different time steps illustrating their rupture geometries. *The rupture shows that* ***(A)*** *the capsule broke as a brittle object,* ***(B)*** *half of the capsule break upon impact, (C) the capsule can break in specific locations without the entire capsule breaking.*

5.2.2.1 Crater Analysis

All analysis is accomplished using Python 3.9. The size and depth of the impact crater were calculated using a Python script that created a surface profile of the particle bed. The program divides the desired region into MxN equal squares. By repeatedly going over all of the particles in the region and adding any that fall within it to a list, the top portion of the particle bed is probed. In order to build a surface morphology of the particle bed, the particle with the greatest z-coordinate is then added to a different list that represents the highest particles in the probed area. A known initial condition of the simulation is the location of the crater's center. To discover where the crater's surface morphology deviates from the norm, linear regression is applied. The left and right sides of a 2D profile are subjected to linear regression after being constructed in the xz or yz plane. The left and rightmost particles are then eliminated, and a loop is formed to repeatedly evaluate the linear regression until the slope gets close to zero. The estimated radius of the crater is calculated as the distance from the center to this location. When the projectile shell has lost enough kinetic energy to no longer be able to penetrate the particle bed any further and when every particle in the bed is at rest, the crater is measured. The crater's diameter and depth at these two points demonstrate the crater's evolution. When the projectile is at its highest penetration depth but still contains moving particles and the hollow in the particle bed hasn't settled, the breadth of the crater is at its narrowest. The walls of the hollow have already started to flow and fall as the particles settle, resulting in a broader and shallower cavity in the particle bed. The evolution of the crater may be discovered by examining the crater at any intermediate points and compared to experimental results.

5.2.2.2 Ejecta Curtain

The curtain of particles that are launched from the bed of particles as a result of the dispersion of kinetic energy inside the bed of particles is another feature of the projectile impact analysis. There are a few methods that can be taken to analyze the ejecta curtain. Processing the particle locations and separating those that are above a particular z value would be the first step. Prior to the projectile's impact, this value should be just below the top of the particle bed. A 2D snapshot can be taken once the particles have started to move. Then, the particles that are still visible within a specific radius of the top of the particle bed are removed from this photo. Then, by measuring the distance from the majority of the remaining particles, outliers are eliminated. Last but not least, linear regression can figure out how steep the particles left are from a specific distance down from the top of the particle bed.

The evolution of the ejecta curtain during the collision will be seen after several time steps of analysis. By doing this, the granular material's dynamics can demonstrate how well the bed behaves as a fluid or a solid. When the crater implodes, the particles will collide and push themselves upward in a stream like a fluid if the material curtain spreads and dissipates.

5.2.2.3 Probing Particles Analysis

The spread of the probe particles that represent the viscoelastic material, the projectile's interior particles, is of particular relevance in this investigation. The geometry of the projectile was designed and altered so that the probe particles may be directed inwards toward the particle bed and disseminated during the ballistic impact. To properly replicate a viscous liquid, multiple trial runs were prepared and launched. LIGGGHTS provides a command that mimics the movements of a liquid; however, this would necessitate either all of the atoms in the simulation mimicking a liquid or only particular interaction pairs mimicking a liquid. This raises the issue of these particles interacting with any particle in the bed. If a pair is set to a liquid interaction, they will interact as if they are both liquids, or if the pair is set to a solid interaction, they will both act as solids. Because only one of the options is available, the only alternative that would better portray the interaction is an all solid interaction. The distance that the particles traveled from an established center point is one of the parameters of the spread of the material that will be tracked in this study.

5.2.3 Future Work to Overcome the Limitations of the Method

This research is aimed to predict the outcomes of experimental work. One of the limitations of LIGGGHTs is introducing a wide range of particles. The neighbor list is an essential feature for saving computation time. When the range of particles increases, the neighbor list for larger particles is much more extensive for smaller particles. As the smaller particles get smaller, the neighbor list gets further extensive, thus increasing computation time further. Currently, with 923 thousand atoms, the current run time of the simulation for 1,400,000 steps is 340,015 seconds, or 5,666.91 minutes, or 94.45 hours, or 3.935 days. Even though the run time for this simulation is less than four days, the time can expand exponentially. As stated previously, a buffer zone is added to the bed of particles to prevent the wall effect in the crater formation. If the buffer zone were replaced with the particle distribution of the central portion of the particle bed, the number of particles would increase to more than ten million particles, and the computation time would increase exponentially. For the simulation to run without crashing, the magnitude of the exponent had to be decreased. When young's modulus was too high, the simulation crashed because the particles did not allow any overlap with hard particles. The magnitude had to be decreased by 4 for LIGGGHTs to run without crashing. Since the machine utilized to simulate the ballistic impact of the projectile was not capable of successfully running the impact with the correct value of Young's Modulus of Elasticity. As we advance, a supercomputer would be ideal for running the simulations.

A supercomputer would be able to handle millions of particles and their interactions. For the setup of the simulations, a bed is created by allowing randomly dispersed particles to intermingle and come to rest in a container. The bouncing and intermingling of the particles are computationally cumbersome, and the process takes a long time to allow the particles to rest. With a supercomputer, the particle distribution will also contain more sizes to simulate the lunar regolith range better. A larger distribution size will also lead to more extensive neighbor lists and a rise in computation time. For the next steps

in the

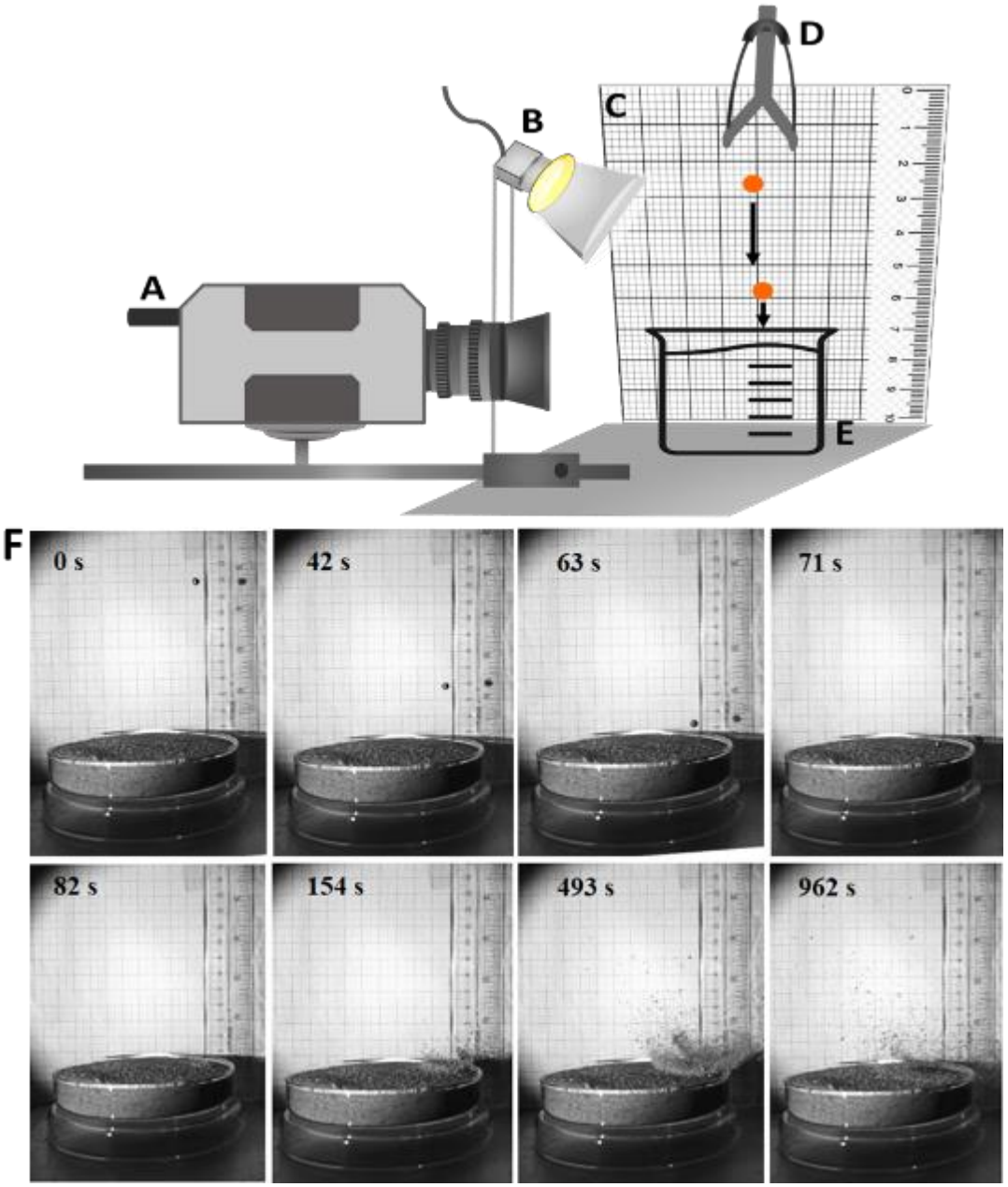

Figure 40. *Schematic representation of impact test setup.* ***(A)*** *High-speed camera fixed to 12000-20000 frames per second. The highspeed camera is connected to a laptop and Photron FASTCAM Viewer is used to count fps and calculate velocity of the microcapsules.* ***(B)*** *White light lamp to illuminate the target surface and the graph sheet.* ***(C)*** *Scale and graph paper adjusted perpendicular to the impact surface or parallel to the direction of the microcapsules.* ***(D)*** *Slingshot used to shoot the microcapsules.* ***(E)*** *A 10 cm wide container filled with Lunar regolith.* ***(F)*** *High-speed camera images of a microcapsule impelled into a powder bed.*

research, the projectile density and the powder bed particle sizes will also be varied so that the capsules can be penetrated.

High-performance computing resources available at the Texas A&M High-Performance Research Computing Center will be used to implement these more realistic simulations. We already have acquired 1M CPU hours on the Grace cluster, partially in support of these efforts.

5.3. Experimental Approach for Microcapsule Delivery into LMS-1 Beds

The delivery system of the thermite mixtures and soil stabilizers is a launching system that can accurately deliver a capsule into a regolith and allow a visco-elastic material to spread into the granular regolith. Experimental capsule delivery studies with the Lunar regolith stimulant are thus necessary to facilitate our delivery approaches in the project. Here we provide a series of impact experiments into the Lunar regolith stimulant (LMS-1) using the experimental setup shown in **Figure 40**. Using this arrangement, it is possible to capture 12000–20000 frames per while recording high-quality impact images into granular materials at rates as high as 50 m/s.

5.3.1 Experimental Design

	Passed through sieve number 200	**40-200**	**LMS regular**
Particle size (µm)	<74	74-425	<2401
Density (g/mL)	1.16 ± 0.01	1.37 ± 0.02	1.78 ± 0.10
			

Table 7. *Particle size distribution of Lunar regolith stimulant for powder baths*

The data presented here was collected using a Fastcam NOVA S9 camera mounted with EF-S 18-135 mm Lens, a collimated LED light source from Thorlabs, and an F-16 slingshot purchased from a local store. Velocity impact tests were designed to mimic the microcapsule's drop into a regolith powder bed. The velocity impact tests were carried out on a regolith powder bed filled in a 7.3 cm wide container (as shown in **Figure 40F**). The simulant material poured into the container was left uncompressed because the compaction level of the stimulant material at the surface could not be well determined in our experiments.

The micro-capsules were shot onto the target surfaces using a slingshot. The terminal velocity on the impact was calculated from the distance traveled and time elapsed as recorded by a high-speed Fastcam NOVA S9 camera. A schematic of the experimental setup is shown in **Figure 40**. The target surface was fixed perpendicular to the direction of the projectile. A scale was fixed perpendicular to the target surface to calculate the distance traveled by the micro-capsule before hitting the target. The high-speed camera was set up perpendicular to the scale. The path of the micro-capsule was lighted with a collimated LED light source. The micro-capsules were shot manually with a slingshot while the camera captured 12000-20000 frames per second. The multiple frames were combined into a single video sequence for review (snapshots included in **Figures 41 and 42**) by FASTCAM photo viewer software.

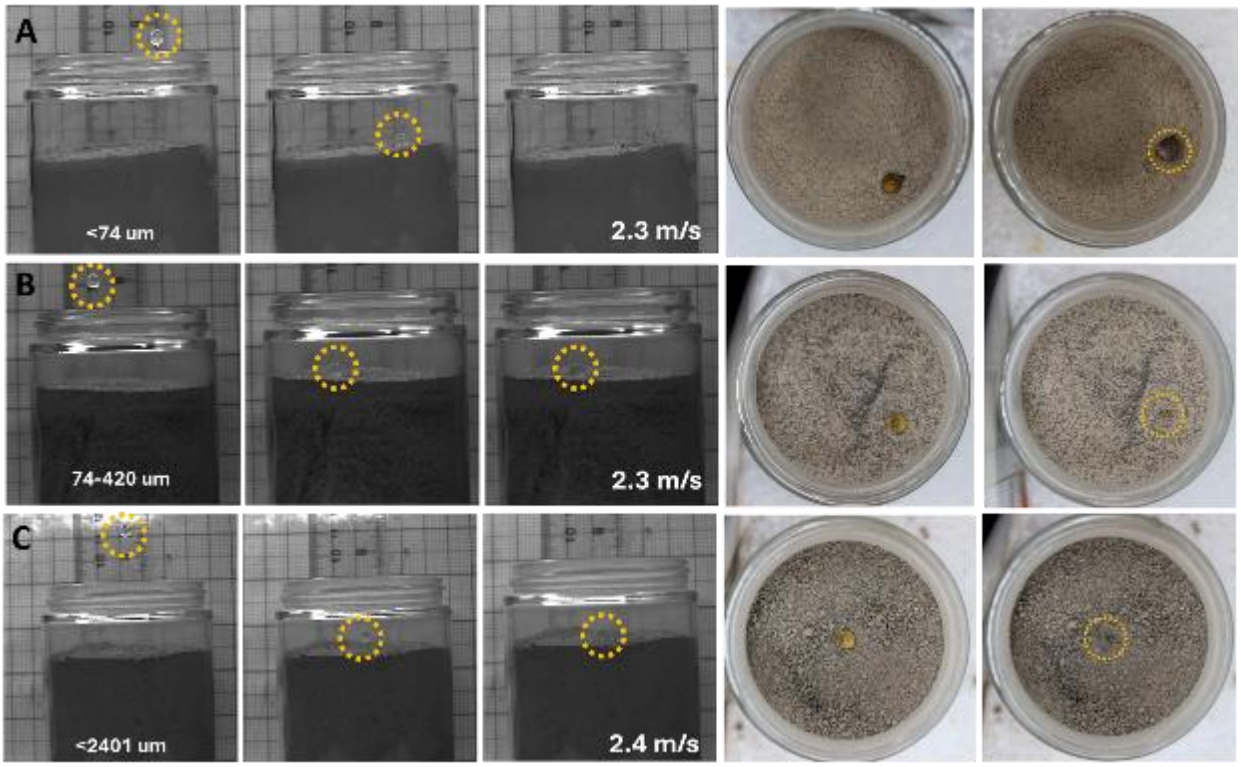

Figure 41. *Side and top view after impact of the microcapsule on the powder bed filled with particle size* ***(A)*** *<74 µm,* ***(B)*** *74-425 µm, and* ***(C)*** *<2401 µm; the launch speed ranges from 2.3-2.4 m/s.*

5.3.2 RESULTS AND DISCUSSION

Table 7 summarizes the particle size and density of a simulant material that was used to test the impact on microcapsule delivery. **Figure 11A** shows the particle size distribution of LMS-1, which ranges from 1 to 2401 µm. On the basis of the particle size of the simulant, powder baths were classified into three categories: (1) 74 m particles passing through a sieve size 200, (2) 74-425 m particles passing through sieve sizes between 40 and 200, and (3) regular LMS-1 stimulants with particle sizes up to 2.4 mm.

A microcapsule of castor oil encapsulated in a calcium alginate shell was launched into the powder baths previously described by launching them normal to the baths. **Figure 41** illustrates the snapshots that were taken when the capsules were launched at speeds of <2.5 m/s. A digital image is displayed on the right side of each panel after the impact is made, followed by a picture of a crater that was formed as a result of the impact. In **Figure 41A-C**, we compare the impact of a projectile about 4 mm in diameter dropped into a container containing different particle sizes of stimulants. Because the height of the container is at least 10X the size of the projectile, it is assumed that the bottom of the container does not influence the penetration depth of the projectile.[63] It is also assumed that the container side wall location had minimal or no influence on the impactor penetration. **Figure 41A** shows slight projectile penetration at speeds of 2.5 m/s with no significant amount of ejecta. In contrast, as shown in **Figures 41B and 41C**, containers filled with particles of larger sizes are resistant to microcapsule penetration.

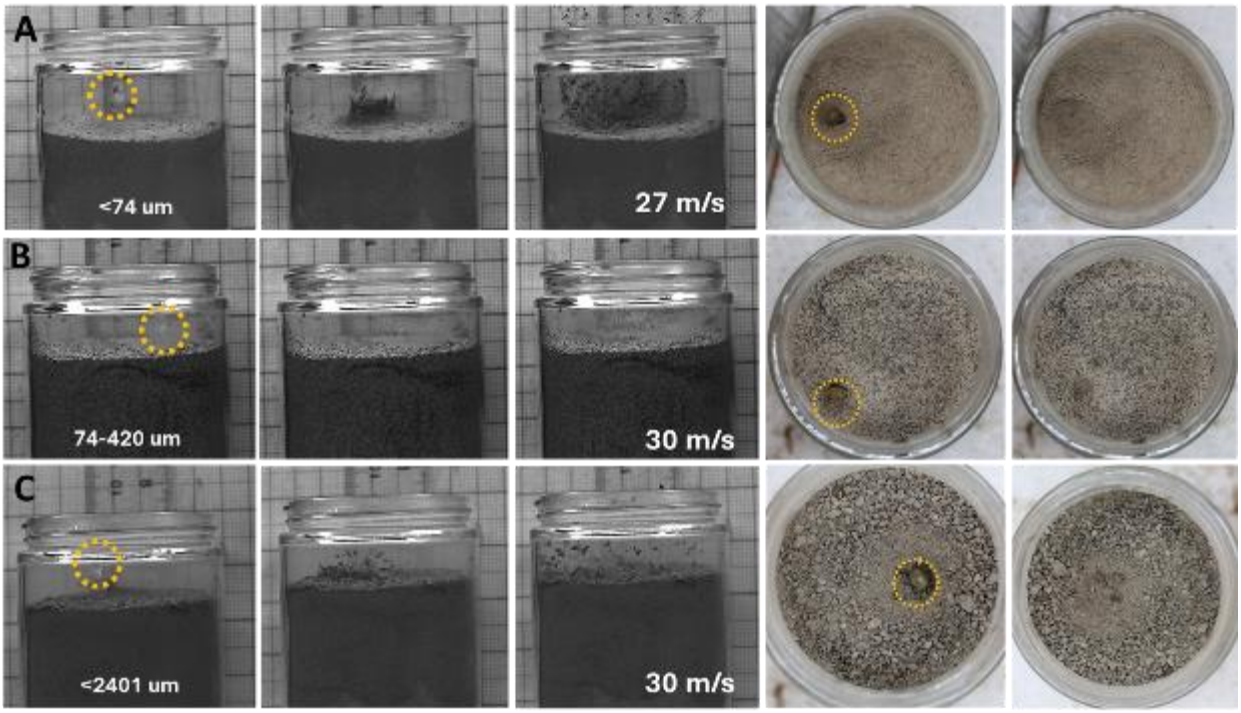

Figure 42. *Side and top view after impact of microcapsule on the powder bed filled with particle size* ***(A)*** *<74 µm,* ***(B)*** *74-425 µm, and* ***(C)*** *<2401 µm; the launch speed ranges from 27-30 m/s.*

Microcapsule delivery studies have shown that altering the velocity of the impact is a viable approach to modification the microcapsule's position on the target surface. It should be noted, however, that each microcapsule has a unique threshold value for penetrating the regolith bath, which is dependent on its particle size. We conducted collisions at higher velocities ranging from 27-30 m/s for all three particle sizes in order to determine the impact of particle size on microcapsule delivery. Based on the results presented in **Figure 42**, it can be seen that the collisions resulted in an embedded projectile (**Figure 42A**).

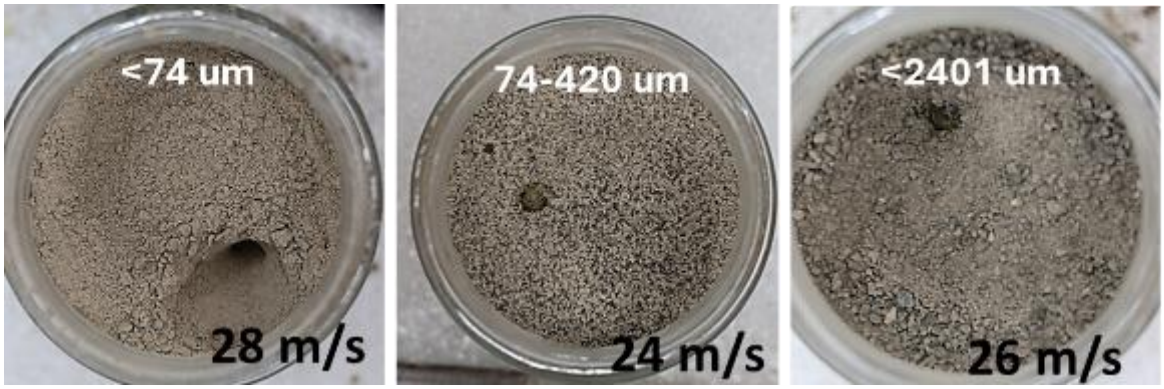

Figure 43. *Top view of penetrated microcapsule in the powder bed conatining particle size* ***(A)*** *<74 µm,* ***(B)*** *74-425 µm, and* ***(C)*** *<2401 µm; the launch speed ranges from 24-28 m/s.*

In spite of the fact that the projectile's motion after impact cannot be observed, the impact velocities can be determined by tracking the distance traveled by the capsules per frame. As can be seen in **Figure 43**, the digital images depict microcapsules being deployed entirely within the regolith at their given speeds, with smaller particles having the greatest penetration impact.

As a next step, we will perform X-ray CT on the deployed sample in order to determine the depth of penetration. The findings provide valuable insight into the impact of particle size and velocity on microcapsule delivery, and this information is crucial to optimizing microcapsule deployment for our application.

5.3.3 FUTURE WORK

Experiments were performed with a model system to mimic the delivery of precursors into the regolith. The impact speeds ranged from 2 m/s to a 30 m/s. Based on the results of this study, different launch velocities can produce different penetration depth effects, including rebound, leakage, or penetration caused by different particle sizes on the surfaces. In general, capsules penetrate deeper into regolith beds at higher impact velocities; smaller particle sizes are associated with further penetration depths. However, these findings need to be validated in low-gravity environments in order to establish broader generalizability and validate this approach for delivery of thermite and matrix transformation precursors reported in preceding sections.

As the research progresses, the model systems will be replaced with more realistic matrix transformation and thermite precursor capsules. As a result, these capsules will be tested for penetration depth and consolidation effects upon initiating the reaction fronts. The experiments and simulations outlined in section 5.2 represent a tightly integrated loop that will be leveraged to develop realistic models that inform the design of chemical precursor delivery systems for in-situ resource utilization and chemical transformations of regolith.

In conclusion, these experiments and simulations provide valuable insights into the impact of microcapsule delivery on the regolith and will be instrumental in the development of efficient and effective delivery systems for future space exploration missions.

6. PROTOTYPE DEVELOPMENT & ONGOING WORK

A large-scale prototype is currently being developed and validated as part of ongoing efforts. **Figure 44** illustrates a large-scale thermite reaction that was conducted at the RELLIS campus of the Texas A&M University system. For these experiments, extensive Environmental Health and Safety and fire department approvals have been obtained in order to ensure their safety. We believe that the results of these large-scale experiments are vital to the successful realization of the goal of stabilizing phase-separated metal sheets and skins of both advanced high-strength steel and Ti-Al-V/Fe alloys. To test the structural integrity of the regolith directly, a series of similar experiments are being undertaken in order to develop scale models of the consolidation reactions in regolith.

Additionally, we intend to transfer the small-scale reaction involving the regolith and its constituent parts to a heating

Figure 44. *Largescale thermite reactions performed at Texas A&M's RELLIS campus.*

furnace (preliminary findings and apparatus shown in **Fig. 45**), where microscopic imaging can precisely optimize solidus or combustion temperatures. The sequences of distinctive volume and shape changes as the temperature rises are recorded

by this common tool for process optimization in the ceramic sector. The is crucial to determine the initial ignition temperature for the various regolith components, and its accuracy will be compared to that of our ab-initio calculation.

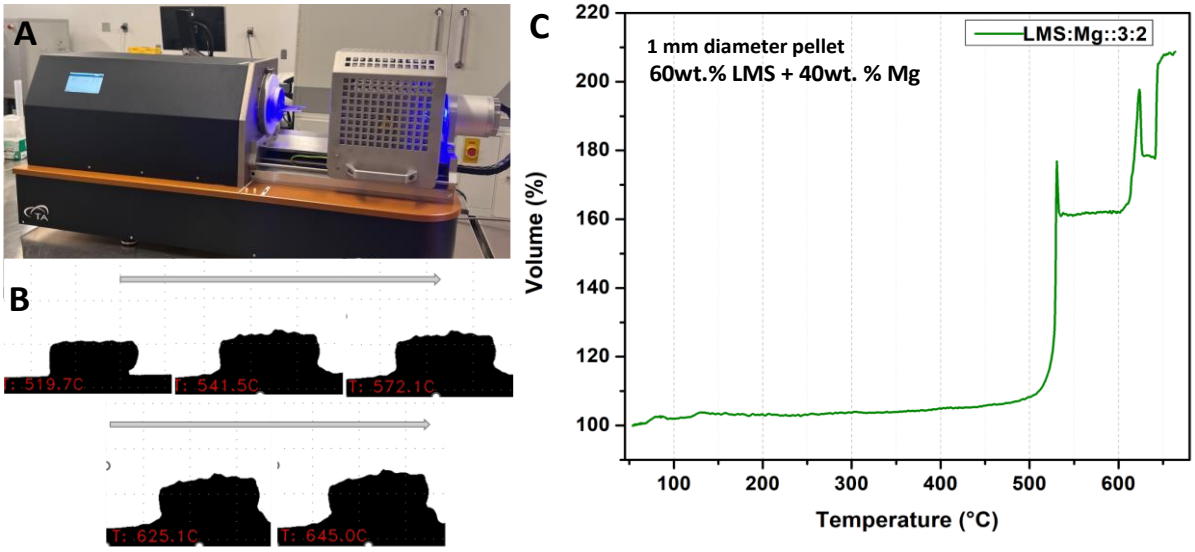

Figure 45: ***(A)*** *Shows a high-temperature furnace equipped with an Ar line for testing thermite reactions.* ***(B)*** *shows the microscopic image of a 1 mm pellet containing 60 wt.% LMS and 40 wt.% Mg at increasing temperatures, illustrating the solidus and combustion temperatures.* ***(C)*** *shows the expansion of volume versus temperature, with the temperature corresponding to the highest volume indicating the temperature at which the pellet combusts to form thermite.*

In phase II, our goal will be (1) the completion of extensive multiscale simulations bridging from atomistic to grain and continuum levels of thermite and regolith consolidation reactions and (2) enable large-scale testing of regolith consolidation chemistry at Texas A&M's RELLIS campus. Phase II will focus on building comprehensive model and detailed demonstrator of our RAMS concept. We further intend to publish several articles and to further refine our innovations with the help of peer review.

7. Products and Outreach

Publications

(1) Cool, N. I.; Perez-Beltran, S.; Cheng, J.; Rivera-Gonzalez, N.; Bronner, D.; Anita; Wang, E.; Zakira, U.; Farahbakhsh, M.; Liu, K.-W.; Hsu, J.-L.; Birgisson, B.; Banerjee, S., Matrix transformation of lunar regolith and its use as a feedstock for additive manufacturing. *iScience* **2023**, *26* (4), 106382.

(2) Anita; Bullard, J. W.; Banerjee, S., Chemical transformations of extraterrestrial soils. *Trends in Chemistry* **2022**, *4* (4), 260-263.

(3) S. Perez Beltran, Anita, B. Birgisson, S. Banerjee, Thermite Reactions as a Means of Metal Recovery and Regolith Consolidation, 2021, *in preparation*.

PRESENTATIONS

(1) Sarbajit Banerjee, JPL&TAMU Materials Collaboration Workshop, 6/8/2021

(2) Sarbajit Banerjee, 1st Annual NASA Excavation and Construction Technology Program Review, 08/31/2021-09/01/2021

(3) Sarbajit Banerjee, NIAC Symposium, 09/16/2021.

(4) Sarbajit Banerjee, Regolith Adaptive Modification System to Support Early Extraterrestrial Planetary Landings and Operations, Lunar Concrete Symposium. 14 December, 2022, Texas State University (online live presentation via Zoom).

COMIC STRIP

We are currently working on a comic strip for elementary and middle school students with Prof. Snezana Stanimirovic from the University of Wisconsin. An initial script has been prepared following two 10-year-olds, Stella and Riley, and their travels through space and to Mars. We expect to publish and disseminate the comic strip in Summer of 2024.

8. REFERENCES

(1) Anita; Bullard, J. W.; Banerjee, S. Chemical Transformations of Extraterrestrial Soils. *Trends Chem.* **2022**, *4* (4), 260–263. https://doi.org/10.1016/J.TRECHM.2022.01.006.

(2) Greenhagen, B. T.; Lucey, P. G.; Wyatt, M. B.; Glotch, T. D.; Allen, C. C.; Arnold, J. A.; Bandfield, J. L.; Bowles, N. E.; Hanna, K. L. D.; Hayne, P. O.; Song, E.; Thomas, I. R.; Paige, D. A. Global Silicate Mineralogy of the Moon from the Diviner Lunar Radiometer. *Science (80-.).* **2010**, *329* (5998), 1507–1509. https://doi.org/10.1126/SCIENCE.1192196/SUPPL_FILE/GREENHAGEN-SOM.PDF.

(3) Engelschiøn, V. S.; Eriksson, S. R.; Cowley, A.; Fateri, M.; Meurisse, A.; Kueppers, U.; Sperl, M. EAC-1A: A Novel Large-Volume Lunar Regolith Simulant. *Sci. Reports 2020 101* **2020**, *10* (1), 1–9. https://doi.org/10.1038/s41598-020-62312-4.

(4) Blake, D. F.; Morris, R. V.; Kocurek, G.; Morrison, S. M.; Downs, R. T.; Bish, D.; Ming, D. W.; Edgett, K. S.; Rubin, D.; Goetz, W.; Madsen, M. B.; Sullivan, R.; Gellert, R.; Campbell, I.; Treiman, A. H.; McLennan, S. M.; Yen, A. S.; Grotzinger, J.; Vaniman, D. T.; Chipera, S. J.; Achilles, C. N.; Rampe, E. B.; Sumner, D.; Meslin, P. Y.; Maurice, S.; Forni, O.; Gasnault, O.; Fisk, M.; Schmidt, M.; Mahaffy, P.; Leshin, L. A.; Glavin, D.; Steele, A.; Freissinet, C.; Navarro-González, R.; Yingst, R. A.; Kah, L. C.; Bridges, N.; Lewis, K. W.; Bristow, T. F.; Farmer, J. D.; Crisp, J. A.; Stolper, E. M.; Des Marais, D. J.; Sarrazin, P. Curiosity at Gale Crater, Mars: Characterization and Analysis of the Rocknest Sand Shadow. *Science (80-.).* **2013**, *341* (6153). https://doi.org/10.1126/SCIENCE.1239505/SUPPL_FILE/BLAKE.SM.PDF.

(5) Bandfield, J. L.; Poston, M. J.; Klima, R. L.; Edwards, C. S. Widespread Distribution of OH/H2O on the Lunar Surface Inferred from Spectral Data. *Nat. Geosci. 2018 113* **2018**, *11* (3), 173–177. https://doi.org/10.1038/s41561-018-0065-0.

(6) Cho, J.; Sheng, A.; Suwandaratne, N.; Wangoh, L.; Andrews, J. L.; Zhang, P.; Piper, L. F. J.; Watson, D. F.; Banerjee, S. The Middle Road Less Taken: Electronic-Structure-Inspired Design of Hybrid Photocatalytic Platforms for Solar Fuel Generation. *Acc. Chem. Res.* **2019**, *52* (3), 645–655. https://doi.org/10.1021/ACS.ACCOUNTS.8B00378.

(7) The production of oxygen and metal from lunar regolith | Elsevier Enhanced Reader https://reader.elsevier.com/reader/sd/pii/S0032063312001821?token=1A80953F9A156A3EE76231128614FB45E200AFE6304F6D3C85335E10433773DA1F33781BBAC6E4A28F74E6B03F11C975&originRegion=us-east-1&originCreation=20210807174700 (accessed Aug 7, 2021).

(8) Rachel Davidson; Ankit Verma; David Santos; Feng Hao; D. Fincher, C.; Dexin Zhao; Vahid Attari; Parker Schofield; Buskirk, J. V.; Antonio Fraticelli-Cartagena; G. Alivio, T. E.; Raymundo Arroyave; Kelvin Xie; Matt Pharr; P. Mukherjee, P.; Sarbajit Banerjee. Mapping Mechanisms and Growth Regimes of Magnesium Electrodeposition at High Current Densities. *Mater. Horizons* **2020**, *7* (3), 843–854. https://doi.org/10.1039/C9MH01367A.

(9) Martell, S. A.; Lai, Y.; Traver, E.; MacInnis, J.; Richards, D. D.; MacQuarrie, S.; Dasog, M. High Surface Area Mesoporous Silicon Nanoparticles Prepared via Two-Step Magnesiothermic Reduction for Stoichiometric CO2 to CH3OH Conversion. *ACS Appl. Nano Mater.* **2019**, *2* (9), 5713–5719.

https://doi.org/10.1021/ACSANM.9B01207/SUPPL_FILE/AN9B01207_SI_001.PDF.

(10) Lasaga, A. C.; Luttge, A. Variation of Crystal Dissolution Rate Based on a Dissolution Stepwave Model. *Science (80-.).* **2001**, *291* (5512), 2400–2404. https://doi.org/10.1126/SCIENCE.1058173.

(11) Cailleteau, C.; Angeli, F.; Devreux, F.; Gin, S.; Jestin, J.; Jollivet, P.; Spalla, O. Insight into Silicate-Glass Corrosion Mechanisms. *Nat. Mater. 2008 712* **2008**, *7* (12), 978–983. https://doi.org/10.1038/nmat2301.

(12) Bajpayee, A.; Farahbakhsh, M.; Zakira, U.; Pandey, A.; Ennab, L. A.; Rybkowski, Z.; Dixit, M. K.; Schwab, P. A.; Kalantar, N.; Birgisson, B.; Banerjee, S. In Situ Resource Utilization and Reconfiguration of Soils Into Construction Materials for the Additive Manufacturing of Buildings. *Front. Mater.* **2020**, *0*, 52. https://doi.org/10.3389/FMATS.2020.00052.

(13) GR, W.; J, C.; M, L.; S, B. Building on Sub-Arctic Soil: Geopolymerization of Muskeg to a Densified Load-Bearing Composite. *Sci. Rep.* **2017**, *7* (1). https://doi.org/10.1038/S41598-017-15115-Z.

(14) Styskalik, A.; Kordoghli, I.; Poleunis, C.; Delcorte, A.; Moravec, Z.; Simonikova, L.; Kanicky, V.; Aprile, C.; Fusaro, L.; Debecker, D. P. Hybrid Mesoporous Aluminosilicate Catalysts Obtained by Non-Hydrolytic Sol–Gel for Ethanol Dehydration. *J. Mater. Chem. A* **2020**, *8* (44), 23526–23542. https://doi.org/10.1039/D0TA07016E.

(15) Grugel, R. N.; Toutanji, H.; Grugel, R. N.; Toutanji, H. Sulfur "Concrete" for Lunar Applications Sublimation Concerns. *AdSpR* **2008**, *41* (1), 103–112. https://doi.org/10.1016/J.ASR.2007.08.018.

(16) Anita; Zaheer, W.; Jakhar, K.; Antao, D. S.; Gupta, S.; Banerjee, S. Powder Bed Coating of Bitumen with Asphaltenes to Obtain Solid Prills for Midstream Transportation. *Fuel* **2021**, *302*, 121093. https://doi.org/10.1016/J.FUEL.2021.121093.

(17) Hayes, A. C.; Osio-Norgaard, J.; Miller, S.; Vance, M. E.; Whiting, G. L. Influence of Powder Type on Aerosol Emissions in Powder-Binder Jetting with Emphasis on Lunar Regolith for In Situ Space Applications. *ACS ES&T Eng.* **2021**, *1* (2), 183–191. https://doi.org/10.1021/acsestengg.0c00045.

(18) Delgado, A.; Shafirovich, E. Towards Better Combustion of Lunar Regolith with Magnesium. *Combust. Flame* **2013**, *160* (9), 1876–1882. https://doi.org/10.1016/J.COMBUSTFLAME.2013.03.021.

(19) Khale, D.; Chaudhary, R. Mechanism of Geopolymerization and Factors Influencing Its Development: A Review. *J. Mater. Sci.* **2007**, *42* (3), 729–746. https://doi.org/10.1007/S10853-006-0401-4/FIGURES/10.

(20) Komnitsas, K.; Zaharaki, D. Geopolymerisation: A Review and Prospects for the Minerals Industry. *Miner. Eng.* **2007**, *20* (14), 1261–1277. https://doi.org/10.1016/J.MINENG.2007.07.011.

(21) Dimas, D.; Giannopoulou, I.; Panias, D. Polymerization in Sodium Silicate Solutions: A Fundamental Process in Geopolymerization Technology. *J. Mater. Sci.* **2009**, *44* (14), 3719–3730. https://doi.org/10.1007/S10853-009-3497-5/FIGURES/15.

(22) Dancer, C. E. J. Flash Sintering of Ceramic Materials. *Mater. Res. Express* **2016**, *3* (10), 102001. https://doi.org/10.1088/2053-1591/3/10/102001.

(23) Guo, J.; Guo, H.; Baker, A. L.; Lanagan, M. T.; Kupp, E. R.; Messing, G. L.; Randall, C. A. Cold Sintering: A Paradigm Shift for Processing and Integration of Ceramics. *Angew. Chemie Int. Ed.* **2016**, *55* (38), 11457–11461. https://doi.org/10.1002/ANIE.201605443.

(24) Castro, R. H. R.; Gouvêa, D. Sintering and Nanostability: The Thermodynamic Perspective. *J. Am. Ceram. Soc.*

2016, *99* (4), 1105–1121. https://doi.org/10.1111/JACE.14176.

(25) Wakai, F.; Brakke, K. A. Mechanics of Sintering for Coupled Grain Boundary and Surface Diffusion. *Acta Mater.* **2011**, *59* (14), 5379–5387. https://doi.org/10.1016/J.ACTAMAT.2011.05.006.

(26) Khoshnevis, B.; Thangavelu, M.; Yuan, X.; Zhang, J. Advances in Contour Crafting Technology for Extraterrestrial Settlement Infrastructure Buildup. *AIAA Sp. 2013 Conf. Expo.* **2013**. https://doi.org/10.2514/6.2013-5438.

(27) Bhatia, A.; Sehgal, A. K. Additive Manufacturing Materials, Methods and Applications: A Review. *Mater. Today Proc.* **2021**. https://doi.org/10.1016/J.MATPR.2021.04.379.

(28) Wang, Z.; Zhang, Y.; Bernard, A. A Constructive Solid Geometry-Based Generative Design Method for Additive Manufacturing. *Addit. Manuf.* **2021**, *41*, 101952. https://doi.org/10.1016/J.ADDMA.2021.101952.

(29) Tian, C.; Li, T.; Bustillos, J.; Bhattacharya, S.; Turnham, T.; Yeo, J.; Moridi, A. Data-Driven Approaches Toward Smarter Additive Manufacturing. *Adv. Intell. Syst.* **2021**, *3* (12), 2100014. https://doi.org/10.1002/AISY.202100014.

(30) Ellery, A. Sustainable In-Situ Resource Utilization on the Moon. *Planet. Space Sci.* **2020**, *184*, 104870. https://doi.org/10.1016/J.PSS.2020.104870.

(31) Khoshnevis, B.; Bukkapatnam, S.; Kwon, H.; Saito, J. Experimental Investigation of Contour Crafting Using Ceramics Materials. *Rapid Prototyp. J.* **2001**, *7* (1), 32–41. https://doi.org/10.1108/13552540110365144/FULL/XML.

(32) Zhuravlev, L. T. Concentration of Hydroxyl Groups on the Surface of Amorphous Silicas. *Langmuir* **1987**, *3* (3), 316–318. https://doi.org/10.1021/LA00075A004.

(33) Melani, G.; Nagata, Y.; Wirth, J.; Saalfrank, P. Vibrational Spectroscopy of Hydroxylated α-Al2O3(0001) Surfaces with and without Water: An Ab Initio Molecular Dynamics Study. *J. Chem. Phys.* **2018**, *149* (1), 014707. https://doi.org/10.1063/1.5023347.

(34) Kai, M. F.; Dai, J. G. Understanding Geopolymer Binder-Aggregate Interfacial Characteristics at Molecular Level. *Cem. Concr. Res.* **2021**, *149*, 106582. https://doi.org/10.1016/J.CEMCONRES.2021.106582.

(35) Yang, L.; Ma, Z.; Stukowski, A. Visualization and Analysis of Atomistic Simulation Data with OVITO–the Open Visualization Tool. *Model. Simul. Mater. Sci. Eng.* **2009**, *18* (1), 015012. https://doi.org/10.1088/0965-0393/18/1/015012.

(36) Liu, Y.; Yu, P.; Wu, Y.; Yang, H.; Xie, M.; Huai, L.; Goddard, W. A.; Cheng, T. The DFT-ReaxFF Hybrid Reactive Dynamics Method with Application to the Reductive Decomposition Reaction of the TFSI and DOL Electrolyte at a Lithium-Metal Anode Surface. *J. Phys. Chem. Lett.* **2021**, *12* (4), 1300–1306. https://doi.org/10.1021/ACS.JPCLETT.0C03720/SUPPL_FILE/JZ0C03720_SI_003.TXT.

(37) Camacho-Forero, L. E.; Smith, T. W.; Balbuena, P. B. Effects of High and Low Salt Concentration in Electrolytes at Lithium-Metal Anode Surfaces. *J. Phys. Chem. C* **2017**, *121* (1), 182–194. https://doi.org/10.1021/ACS.JPCC.6B10774/ASSET/IMAGES/LARGE/JP-2016-107748_0010.JPEG.

(38) Kresse, G.; Furthmüller, J. Efficiency of Ab-Initio Total Energy Calculations for Metals and Semiconductors Using a Plane-Wave Basis Set. *Comput. Mater. Sci.* **1996**, *6* (1), 15–50. https://doi.org/10.1016/0927-0256(96)00008-0.

(39) Kresse, G. Ab Initio Molecular Dynamics for Liquid Metals. *J. Non. Cryst. Solids* **1995**, *192–193*, 222–229. https://doi.org/10.1016/0022-3093(95)00355-X.

(40) Kresse, G.; Furthmüller, J. Efficient Iterative Schemes for *Ab Initio* Total-Energy Calculations Using a Plane-Wave Basis Set. *Phys. Rev. B* **1996**, *54* (16), 11169. https://doi.org/10.1103/PhysRevB.54.11169.

(41) Kresse, G.; Joubert, D. From Ultrasoft Pseudopotentials to the Projector Augmented-Wave Method. *Phys. Rev. B* **1999**, *59* (3), 1758. https://doi.org/10.1103/PhysRevB.59.1758.

(42) Perdew, J. P.; Burke, K.; Ernzerhof, M. Generalized Gradient Approximation Made Simple. *Phys. Rev. Lett.* **1996**, *77* (18), 3865. https://doi.org/10.1103/PhysRevLett.77.3865.

(43) Kamphaus, E. P.; Balbuena, P. B. First-Principles Investigation of Lithium Polysulfide Structure and Behavior in Solution. *J. Phys. Chem. C* **2017**, *121* (39), 21105–21117. https://doi.org/10.1021/ACS.JPCC.7B04822/ASSET/IMAGES/LARGE/JP-2017-048227_0009.JPEG.

(44) Plimpton, S. Fast Parallel Algorithms for Short-Range Molecular Dynamics. *J. Comput. Phys.* **1995**, *117* (1), 1–19. https://doi.org/10.1006/JCPH.1995.1039.

(45) Joshi, K. L.; Psofogiannakis, G.; Van Duin, A. C. T.; Raman, S. Reactive Molecular Simulations of Protonation of Water Clusters and Depletion of Acidity in H-ZSM-5 Zeolite. *Phys. Chem. Chem. Phys.* **2014**, *16* (34), 18433–18441. https://doi.org/10.1039/C4CP02612H.

(46) Hong, S.; Van Duin, A. C. T. Molecular Dynamics Simulations of the Oxidation of Aluminum Nanoparticles Using the ReaxFF Reactive Force Field. *J. Phys. Chem. C* **2015**, *119* (31), 17876–17886. https://doi.org/10.1021/ACS.JPCC.5B04650/SUPPL_FILE/JP5B04650_SI_001.PDF.

(47) Wen, Y.; Liu, X.; Chen, X.; Jia, Q.; Yu, R.; Ma, T. Effect of Heat Treatment Conditions on the Growth of MgAl2O4 Nanoparticles Obtained by Sol-Gel Method. *Ceram. Int.* **2017**, *43* (17), 15246–15253. https://doi.org/10.1016/J.CERAMINT.2017.08.061.

(48) Aupoil, J.; Champenois, J. B.; d'Espinose de Lacaillerie, J. B.; Poulesquen, A. Interplay between Silicate and Hydroxide Ions during Geopolymerization. *Cem. Concr. Res.* **2019**, *115*, 426–432. https://doi.org/10.1016/J.CEMCONRES.2018.09.012.

(49) Panagiotopoulou, C.; Kontori, E.; Perraki, T.; Kakali, G. Dissolution of Aluminosilicate Minerals and By-Products in Alkaline Media. *J. Mater. Sci.* **2007**, *42* (9), 2967–2973. https://doi.org/10.1007/S10853-006-0531-8.

(50) Cao, S.; Piao, L.; Chen, X. Emerging Photocatalysts for Hydrogen Evolution. *Trends Chem.* **2020**, *2* (1), 57–70. https://doi.org/10.1016/J.TRECHM.2019.06.009.

(51) Anita; Bullard, J. W.; Banerjee, S. *Chemical Transformations of Extraterrestrial Soils*.

(52) Hafner, J. Ab-Initio Simulations of Materials Using VASP: Density-Functional Theory and Beyond. *J. Comput. Chem.* **2008**, *29* (13), 2044–2078. https://doi.org/10.1002/JCC.21057.

(53) Monkhorst, H. J.; Pack, J. D. Special Points for Brillouin-Zone Integrations. *Phys. Rev. B* **1976**, *13* (12), 5188. https://doi.org/10.1103/PhysRevB.13.5188.

(54) Chen, Z.; Li, Z.; Li, J.; Liu, C.; Lao, C.; Fu, Y.; Liu, C.; Li, Y.; Wang, P.; He, Y. 3D Printing of Ceramics: A Review. *J. Eur. Ceram. Soc.* **2019**, *39* (4), 661–687. https://doi.org/10.1016/J.JEURCERAMSOC.2018.11.013.

(55) Isachenkov, M.; Chugunov, S.; Akhatov, I.; Shishkovsky, I. Regolith-Based Additive Manufacturing for

Sustainable Development of Lunar Infrastructure – An Overview. *Acta Astronaut.* **2021**, *180*, 650–678. https://doi.org/10.1016/J.ACTAASTRO.2021.01.005.

(56) Tailby, J.; MacKenzie, K. J. D. Structure and Mechanical Properties of Aluminosilicate Geopolymer Composites with Portland Cement and Its Constituent Minerals. *Cem. Concr. Res.* **2010**, *40* (5), 787–794. https://doi.org/10.1016/J.CEMCONRES.2009.12.003.

(57) ZHOU, S.; ZHU, X.; LU, C.; LI, F. Synthesis and Characterization of Geopolymer from Lunar Regolith Simulant Based on Natural Volcanic Scoria. *Chinese J. Aeronaut.* **2022**, *35* (1), 144–159. https://doi.org/10.1016/J.CJA.2020.06.014.

(58) Mills, J. N.; Katzarova, M.; Wagner, N. J. Comparison of Lunar and Martian Regolith Simulant-Based Geopolymer Cements Formed by Alkali-Activation for in-Situ Resource Utilization. *Adv. Sp. Res.* **2022**, *69* (1), 761–777. https://doi.org/10.1016/J.ASR.2021.10.045.

(59) Davis, G.; Montes, C.; Eklund, S. Preparation of Lunar Regolith Based Geopolymer Cement under Heat and Vacuum. *Adv. Sp. Res.* **2017**, *59* (7), 1872–1885. https://doi.org/10.1016/J.ASR.2017.01.024.

(60) Alexiadis, A.; Alberini, F.; Meyer, M. E. Geopolymers from Lunar and Martian Soil Simulants. *Adv. Sp. Res.* **2017**, *59* (1), 490–495. https://doi.org/10.1016/J.ASR.2016.10.003.

(61) Luna-Galiano, Y.; Fernández-Pereira, C.; Izquierdo, M. Contributions to the Study of Porosity in Fly Ash-Based Geopolymers. Relationship between Degree of Reaction, Porosity and Compressive Strength. *Mater. Constr.* **2016**, *66* (324). https://doi.org/10.3989/MC.2016.10215.

(62) Lee, S.; van Riessen, A. A Review on Geopolymer Technology for Lunar Base Construction. *Mater. 2022, Vol. 15, Page 4516* **2022**, *15* (13), 4516. https://doi.org/10.3390/MA15134516.

(63) Brisset, J.; Colwell, J.; Dove, A.; Abukhalil, S.; Cox, C.; Mohammed, N. Regolith Behavior under Asteroid-Level Gravity Conditions: Low-Velocity Impact Experiments. *Prog. Earth Planet. Sci.* **2018**, *5* (1). https://doi.org/10.1186/s40645-018-0222-5.